A PARAMETRIC ANALYSIS OF GUST-INDUCED AIRFOIL SURFACE-PRESSURE PHASE BEHAVIOR

By

HARIKISHIN PRAKASH BAKHTIANI

Bachelor of Science

Oklahoma State University

Stillwater, Oklahoma

2002

Submitted to the Faculty of the
Graduate College of the
Oklahoma State University
in partial fulfillment of
the requirements for
the Degree of
MASTER OF SCIENCE
July, 2004

A PARAMETRIC ANALYSIS OF GUST-INDUCED

AIRFOIL SURFACE-PRESSURE

PHASE BEHAVIOR

Thesis Approved:

_____

Thesis Advisor

_____

_____

_____

Dean of the Graduate College

ACKNOWLEGMENTS

A work of this magnitude was made possible only by the assistance of many individuals. First and foremost, I would like to thank my graduate advisor and committee chair Dr. Eric A. Falk. Thank you, sir, for your continuous support, guidance and hard work. You are truly a great friend and mentor. Words cannot express my appreciation of your encouragement, inspiration and patience. Gratitude and appreciation are also extended to my other committee members, Dr. Andrew S. Arena and Dr. Afshin J.Ghajar.

To my friends and colleagues at the Turbolab, it's been both an honor and privilege to have met and worked with you all. Aaron thanks for all your help. Robert thanks for answering all my questions and guiding me when direction was needed.

Finally, a special 'thank you' to my parents, Prakash and Jaya Bakhtiani for their continuous love, support and words of encouragement. The successes I have achieved did not come without certain sacrifices, which they endured in some form. Finally to my brother, Nicky, who never fails to amaze me.

TABLE OF CONTENTS

LIST OF TABLES

LIST OF FIGURES

NOMENCLATURE

Symbols

$\Delta C_p{}'$	=	unsteady differential-pressure coefficient
$\Delta p'$	=	differential unsteady pressure
$\hat{n}$	=	normal vector to lifting-surface chord
ω	=	disturbance angular frequency
ϕ	=	surface-pressure phase distribution
ρ_∞	=	freestream mean density
$\vec{\psi}_m$	=	m-th mode shape vector
a	=	forcing-disturbance transverse velocity
c	=	lifting-surface chord
f_m	=	m-th mode generalized force
$H_i^{(2)}$	=	i-th order Hankel function, 2nd kind
k	=	reduced frequency
S	=	Sears function
U_∞	=	freestream mean velocity
x/c	=	non-dimensional distance along chord
$\bar{u}_i$	=	mean velocity component
u_i'	=	unsteady velocity component

G_k = turbulent kinetic energy due to mean velocity gradients

G_b = turbulent kinetic energy due to buoyancy

ε = dissipation rate

$\vec{v}$ = velocity vector ($=u\hat{i}+v\hat{j}$) in 2D

$\vec{A}$ = surface are vector

Γ_ϕ = diffusion coefficient for ϕ

S_ϕ = source of ϕ per unit volume

N_{faces} = number of faces enclosing cell

$\rho_f \upsilon_f \vec{A}_f$ = mass flux through the face

$(\nabla\phi)_n$ = magnitude of $\nabla\phi$ normal to face f

$P_{t,i}$ = total pressure inlet

P_t = total pressure

P' = unsteady pressure

P = instantaneous pressure

$\overline{P}$ = time-averaged pressure

TE = trailing edge

LE = leading edge

Acronyms

CFD = computational fluid dynamics

AOA = angle of attack

RANS = Reynolds-averaged Navier-Stokes equations

1 CHAPTER 1

INTRODUCTION

1.1 OVERVIEW OF AIRFOIL GUST INTERACTIONS

Lifting-surface response to unsteady aerodynamic forcing is of particular interest in aircraft propulsion applications, primarily due to time-resolved aerodynamic interactions in turbomachinery. In these applications, lifting surfaces (i.e., airfoils) often operate in both randomly turbulent and periodically oscillating fluid environments, including temporally and spatially non-uniform propagating disturbances. Relative unsteady motion between a lifting surface and the fluid results in complex fluid-structure interactions and may produce aerodynamic/structural response. In order to optimize lifting-surface designs, a detailed understanding of inherent fluid-structure interactions is required, where these interactions can be described, in part, by lifting-surface pressure response. Unsteady surface-pressure phase distributions compromise one aspect of lifting-surface fluid-structure interactions, as phase directly affects time-resolved unsteady force/moment behavior, particularly in terms of forcing structural modes.

1.2 COMPRESSOR DESIGN INTENT AND OPERATING ENVIRONMENT

For the purpose of emphasizing the continued need for investigating unsteady fluid-structure interactions, consider an axial-flow compressor. Axial-flow compressors are typically composed of a number of rotating blades for the purpose of turning and

adding work to the passing airflow. This turning process accomplishes a desired total enthalpy rise through the device. A single row of rotating blades is often referred as a blade row. A blade row can lead or follow a separate single row of stationary vanes often referred to as a vane row. Vane rows direct rotor inlet/outlet airflow corresponding to the compressor design. In modern compressors, achieving the design rise requires several blade/vane rows, each providing a portion of the enthalpy difference. Each pair of blade/vane rows represents a stage in the compressor [Falk, 2000].

With the overall goal of engine design being often to decrease engine size and weight, compressor size and weight must also be decreased. A lower number of stages and reduced axial spacing between stages helps to accomplish this goal. However, operating at lower number of stages requires a corresponding increase in stage aerodynamic loading to achieve the desired compressor enthalpy rise. In addition, reduced stage-to-stage spacing leads to greater aerodynamic interactions between vane/blade rows. Such interactions come in the form of disturbances caused by the relative motion between the rotor and stator rows.

1.3 NORMAL COMPRESSOR OPERATION LEADING TO AIRFOIL-GUST INTERACTIONS

The rotational motions between rotor/stator rows, or stages, in a turbine-engine compressor generate a designed enthalpy rise across the component. In the process, however, each stage induces propagating aerodynamic disturbances that act as periodic excitations, or forcing functions, for neighboring blade/vane rows. These propagating disturbances are generally grouped as:

- Convective downstream-propagating viscous wakes: produced by the frictional interactions between the fluid and lifting surface.
- Convective downstream-propagating vortical wakes: produced by vortex shedding in response to bound circulation fluctuations on the lifting surface.
- Acoustically propagating potential disturbances: elicited by variations in the velocity potential, or pressure fields, associated with the blades of a given row [Hall, 1991]. Induced potential disturbances may be temporary in nature, decaying exponentially in the near field, or propagate without attenuation into the far field, depending on blade-tip Mach numbers.

Interactions between a lifting surface and propagating disturbance field induces time-dependent angle-of-attack changes on the body, causing spatially and temporally dependent surface-pressure distributions. Integration of these surface-pressure distributions forms unsteady forces and moments on the body. Moments and forces generate temporally and spatially dependent mechanical stresses, or alternating stresses. If the induced alternating stresses are strong enough, structural fatigue may plague the lifting-surface with the possibility of catastrophic failure.

Fatigue is a process of cumulative structural damage caused by repeated load fluctuations, or stresses [Barsom, 1987]. Fatigue occurs in regions deforming plastically under applied loads; thus, under purely elastic stress conditions, localized areas of raised stress must be present to induce fatigue, where these raised stresses exceed the material yield stress. Prolonged exposure to fatigue-inducing unsteady loads may cause initiation and subsequent propagation of a crack, or cracks, in plastically deformed structural regions. Eventually, if crack propagation continues, catastrophic fracture and failure of

the lifting surface may occur. Typically the number of load fluctuations necessary to initiate a crack within working lifting-surfaces(such as a compressor blade/vane row) is quite large; thus, the cumulative structural damage process is often referred to as high cycle fatigue, or HCF.

Aerodynamically induced load fluctuations in a jet engine compressor composed of high-strength structural components are designed to yield only elastic stress fluctuations. However, the occurrence of random material defects, foreign object damage (FOD), or blade rubbing can provide the proper conditions for crack initiation and propagation. Nonetheless, the number of load fluctuations typically required to form a crack within a jet engine blade/vane component is quite large, leading to HCF.

1.4 IMPORTANCE OF HCF TO ENGINE COMMUNITY

High-cycle fatigue is of utmost importance in current jet engine design, were small structural failures can greatly affect entire engine operations to the extent of engine failure. Due to its importance, a considerable number of experimental and computational investigations have been conducted with the overall goal of predicting lifting-surface HCF failures in jet engines. Nonetheless, jet engine HCF failures continue to occur and are largely unanticipated. Recent advances in engine technology may only complicate this problem, as current trends toward higher blade loadings, increased operating temperatures, smaller stage-to-stage spacing, unconventional geometries, and advanced materials reach beyond traditional design domains, complicating HCF-resistant technology [Fleeter, 1992]. In practice, HCF-related engine failure has been identified as a major contributor to engine-safety mishaps in U. S. military fighter aircraft [Thompson, 1998], where as many as 50% of all engine failures have been attributed to HCF. As

such, HCF failure presents a major readiness and monetary concern for both the U.S. Air Force and U.S. Navy [Fecke, 1998].

In an attempt to overcome reoccurring HCF problems in military engines, the U.S. Department of Defense established the National Turbine Engine High Cycle Fatigue Program in 1994. The goal of this ongoing program is to develop, implement, and validate damage tolerant design methodologies to avoid HCF-related engine failures. This goal is to be accomplished by increasing the level of understanding regarding HCF physics, as well as through the development of better HCF predictive capabilities. The specific goal of improving predictions of engine component response to unsteady aerodynamic forcing belongs to the Science and Technology branch of the HCF program.

1.5 IMPORTANCE OF PHASE DISTRIBUTIONS IN PREDICTING AIRFOIL MODAL FORCING

In order to avoid structural vibrations and HCF-related failures, it is important to accurately predict time-resolved generalized forces for each lifting-surface structural mode. Unsteady surface-pressure phase distributions represent one component of such predictions. Chordwise-varying phase distributions influence time-resolved surface-pressure amplitude distributions along the chord. Chordwise varying phase may also affect surface-pressure node locations, where the node locations change positions with different phase distributions. Mispredictions of chordwise-varying phase may result in under predicted modal forces, generating greater-than-expected mechanical stresses at multiple spatial and temporal frequencies, and therefore HCF. In all, unsteady surface-pressure phase distributions play a very important role in lifting-surface unsteady forcing and thus predictions of modal forcing. A brief example illustrating the importance of

considering unsteady surface-pressure phase distributions in lifting-surface forcing is provided in Chapter 2.

1.6 NEED FOR CONTINUED SURFACE-PRESSURE PHASE ANALYSIS

Given the potential for catastrophic structural failure caused by lifting-surface fatigue-life degradation, accurate fluid-structure interaction predictions have been aggressively sought for aerodynamic unsteady forcing problems. In fact, extensive amounts of information are available regarding the influence of forced response on turbomachine lifting surfaces (due to the propensity of high-cycle fatigue failures in modern high-performance gas turbine engines). Representative investigations have predicted, or measured, unsteady surface-pressure distributions on various lifting bodies, and characterized these distributions in terms of amplitude, frequency, and phase. These investigations typically focus on surface-pressure amplitude and frequency, with little attention to the influence of surface-pressure phase. This is not to say that phase has been completely ignored. In fact, the contrary is true. Researchers have reported surface-pressure phase data over lifting surfaces under a variety of forcing conditions, as will be discussed in Chapter #2.

Despite the inclusion of phase results in many research investigations, however the dependence of lifting-surface response to variations in chordwise surface-pressure phase distribution remains relatively unexamined. Moreover, no known investigation has developed general "rules of thumb" to act as guidelines in predicting phase distributions for the most common forcing configurations. Lastly, no consistent explanation exists for observed surface-pressure phase variations between different forcing configurations. The

role of surface-pressure phase in the production of structural vibrations and HCF failures therefore remains largely unresolved.

1.7 SCOPE OF CURRENT INVESTIGATION

The objective of the current research is to conduct a series of numerical simulations to examine the influence of various aerodynamic-forcing and lifting-surface configurations on chordwise surface-pressure phase distributions. In particular, the influence of lifting-surface thickness, camber and angle of attack is discussed. The influences of different solidity values as well as the fundamental physics underlying chordwise surface-pressure phase distributions are also explored. Results will assist the interpretation of experimentally and computationally generated chordwise surface-pressure phase data, as well as provide fundamental results to assist future lifting-surface design efforts in resisting aeroelastic modal forcing. Finally, a comparison between the computed phase results and experimental cascade data reported by Fabian et al. and Falk et al. is presented, providing an explanation of the observed experimental phase trends.

2 CHAPTER 2

PREVIOUS WORK

This chapter reviews previous work in the area of unsteady lifting-surface aerodynamic forcing. The purpose of this review is to place the current research in proper perspective, establishing its motivation, importance and its potential contribution to the aerodynamic forced-response community.

2.1 LITERARY REVIEW

Many researchers have reported surface-pressure phase distributions over lifting surfaces under a variety of forcing conditions. Numerous experimental investigations have been performed on isolated airfoils, cascades and jet engine blade/vane rows in an attempt to understand the detailed fluid-structure interactions related to lifting-surface forced response.

2.1.1 Single-Airfoil Investigations

One of the early works in the field of lifting-surface forced response was conducted by Sears [1938, 1941], who examined unsteady aerodynamic forcing of rigid infinite-span flat plates by convecting chordwise sinusoidal gusts in an incompressible inviscid flow. Sears derived a relationship for the chordwise, unsteady, non-dimensional, differential-pressure amplitude distribution on such lifting surfaces as

$$\Delta C_p' = 2\pi\sqrt{\frac{1-x/c}{1+x/c}}S(k)e^{i\omega t} \tag{2.1}$$

where

$$S(k) = \frac{2}{\pi k[H_0^{(2)} - iH_1^{(2)}]} \tag{2.2}$$

Unsteady surface-pressure time series predicted by Eq. (2.1) are found to be synchronous along the chord, indicating no chordwise time delay between pressure-amplitude peaks/troughs. Thus, Eq. 2.1 predicts surface-pressure chordwise phase to be independent of gust propagation speed. The results of Sears suggest instantaneous surface-pressure response along the entire lifting-surface chord to the convective sinusoidal gusts. By extension, Sears predicts corresponding surface-pressure phase distributions versus chord would show zero phase slope; i.e., require the entire surface to respond instantaneously to all forcing disturbances.

Although not noted by Sears, his results suggest a chordwise-varying phase distribution should correlate with finite surface-pressure propagation speeds over a lifting surface. Thus, the slope of a surface-pressure phase distribution along the chord relates to forcing-disturbance propagation speed. Faster disturbance propagation corresponds to less phase change, or lower slope, with chord and vice-versa.

2.1.2 Turbomachine and Cascade Investigations

Turbomachine unsteady forcing phenomena were also experimentally investigated to verify existing analytical results, as well as identify new flow physics. For example, Fleeter et. al. conducted an experimental investigation to determine rotor-induced unsteady pressure distributions on downstream stator vanes [Fleeter et. al., 1978]. This was accomplished in the Detroit Diesel Allison (DDA) large-scale, low-

speed, single-stage research compressor. This investigation studied the effects of reduced frequency and incidence angle on stator-vane surface-pressure distribution. Measurements were collected with embedded pressure transducers mounted axially along both suction and pressure surfaces of the stator vanes [Fleeter et al., 1978].

Resultant unsteady surface-pressure amplitudes were shown to compare reasonably well with existing analytical results for all reduced frequency values at small incidence values. However, at large negative incidence angles, experimental data correlations with predictions were very poor. This was attributed to convected-wake phenomena not modeled in the analysis. Corresponding surface-pressure phase results were found to be ambiguous (i.e., no clear chordwise trend) leading to the conclusion that rotor wakes travel differently over airfoil suction and pressure surfaces, depending upon their harmonic frequency.

Fleeter et al. also observed similar wake-propagation behavior in a later study [Fleeter et al., 1980]. In this investigation, rotor-induced surface-pressure data acquired on cambered stator-vanes were compared to flat-plate, vortical gust code results to determine the effect of airfoil camber on airfoil unsteady lift. Unsteady surface-pressure amplitudes on cambered stator vanes exhibited amplification at the leading edge decaying in the chordwise direction. As such, amplitude data correlated very well with theoretical predictions, at both zero and negative incidence angles. However, phase data for the cambered stator-vanes again exhibited ambiguous characteristics, showing very poor correlation with the theoretical predictions. In particular, phase data were found to correlate with the theoretical predictions only in the leading edge region, varying linearly from the predicted results downstream. Here again, Fleeter et al. attributed this poor

phase behavior to unknown convected-wave phenomenon appearing along the cambered-airfoil vane row. The convected-wave phenomenon first appeared near the rear of the vane, moving forward as incidence angle decreased. This phenomenon also exhibited different behavior on the vane pressure and suction surfaces. Unfortunately, the observed convected-wave phenomenon was not modeled or investigated fully, in the presented analysis.

Lifting-surface chordwise relative-phase information was experimentally examined by Fabian et al in a linear transonic cascade [Fabian et. al., 1996]. The cascade consisted of six production-hardware stator vanes collected from the fan stage in a F109 turbofan engine. Stator vanes were placed in a 4 in. × 4 in. cross-section cascade wind tunnel, creating five two-dimensional passages; flow turning through the passages induced vane mean aerodynamic loading. Vane unsteady forcing was accomplished via a row of five circular cylinders placed 0.8 vane chords upstream or downstream of the vane row; allowing forward or rearward aerodynamic forcing, respectively. In the rearward-forcing configuration, upstream-propagating potential disturbances, created by shed bound circulation on the downstream cylinders, forced the vane row. Unsteady, phase-locked, surface-pressure measurements were collected on the vanes at various freestream Mach numbers not exceeding 0.59.

Surface-pressure results indicated rearward forcing to elicit nearly linear phase behavior with chord, as illustrated in Figure 2-1, for both first and second harmonic surface-pressure frequencies. Note the slope of the phase data is positive with respect to chord, indicating an upstream-propagating forcing disturbance, as predicted by the superimposed line showing analytical model results. The linear nature of data also

suggest phase to be independent of aerodynamic loading, and have a constant propagation speed [Fabian et al., 1996]. Thus, forcing disturbance and surface-pressure propagation correlate in the rearward-forced cascade configuration.

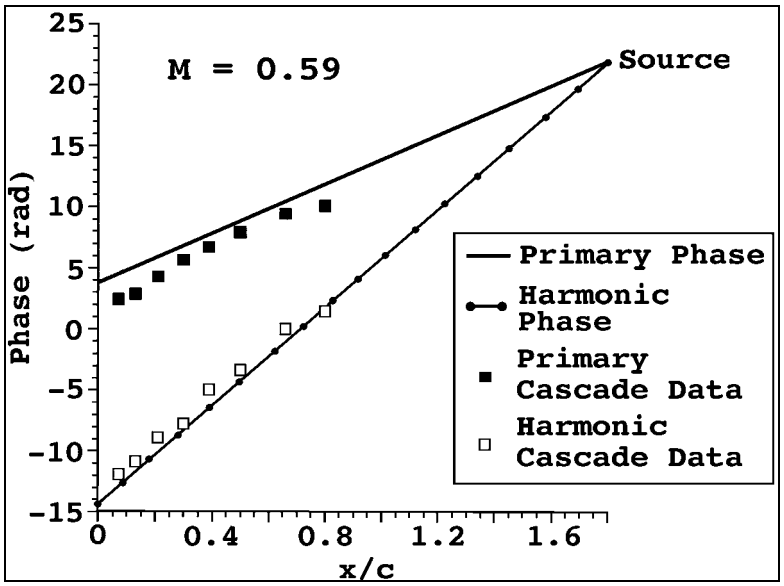

Figure 2-1 Relative Phase Variation with Chord: Rearward-Forced Cascade of Fabian et al. [1996].

In addition to rearward forcing, forward-forcing investigations conducted by Fabian et al. also examined chordwise phase distributions [Fabian et al., 2001]. By placing forcing cylinders upstream of the vane row, the cascade configuration allowed convective cylinder wakes to propagate across and force the cascade row. Phase-locked surface-pressure measurements, analogous to those collected during rearward forcing, produced chordwise phase distributions such as Figure 2-2. Note that unlike the rearward-forcing phase data, the forward-forcing data are not linear, have no clear slope or pattern, and do not agree with the analytical phase model results (solid lines). As such, Fabian et al. termed this data behavior as "ambiguous", attributing the chaotic nature of the data to cylinder-wake interaction with downstream-propagating potential disturbances also emanating from the forcing cylinders. The ambiguous phase results of Figure 2-2

raised the question as to whether such phase ambiguity might also be expected in a rotating machine, as opposed to the linear cascade setup.

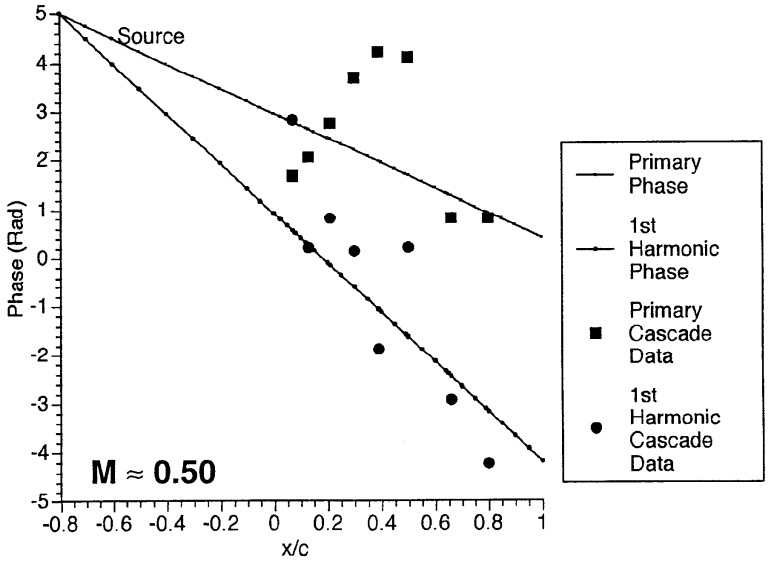

Figure 2-2 Relative Phase Variation with Chord: Forward-Forced Cascade of Fabian et al. [1996].

In order to answer the question raised by the cascade study [Fabian et al., 1996], phase-locked, unsteady, surface-pressure measurements were performed across swept stator vanes in a running F109 turbofan engine [Falk et al., 1997]. Unlike most turbofan engines, the F109 has only a single stage of axial compression. Therefore, no obstructions exist downstream of the stator vanes that might produce upstream-propagating disturbances. The only disturbances propagating across the stator vanes develop from upstream. This forcing configuration is analogous to the forward-forced cascade of Fabian et al. Results from the investigation by Falk again showed lifting-surface phase information to not display a definite propagation direction at either the convected or acoustic disturbance speed along the vane. In fact, the phase ambiguity measured in the F109 supported the previous arguments of Fabian et al. [1996] and provided presumptive evidence of a strong interaction between downstream-propagating potential and

convected disturbances. Of these disturbances, one was argued to be the vortical wakes created by the fan blades at the blade-passing frequency, propagating at the local convection velocity. The other disturbance was argued to be a potential disturbance also created at the blade-passing frequency, but propagating downstream at acoustic speeds.

Frey and Fleeter [Frey, 1998], performed experiments to investigate and quantify gust-generated unsteady aerodynamic response of stator blades. In their experiment, 2/revolution unsteady aerodynamic forcing functions were introduced to a first stage rotor-blade row, these forcing disturbances having significant vortical and potential components. Obtained results showed unsteady pressure amplitudes to reach a high value near the leading edge, decaying by 75% at mid-chord and then increasing slightly in the aft chord; such amplitude behavior was also observed by Fabian et al. Results again suggested a strong interaction between vortical and potential disturbances, comparing well with proprietary codes named LINFLO and LINSUB. Unfortunately, no explanation of chordwise phase distributions was given.

2.2 UNRESOLVED ISSUES

The aforementioned investigations provide essential improvements toward understanding lifting-surface surface-pressure distributions under a variety of forcing conditions; however, the unexplained behavior of reported phase data remains an open topic. Upon review, a consistent explanation for observed surface-pressure phase variations along examined lifting surfaces under various aerodynamic forcing configurations does not exist. As such, researchers and designers working in the forced-response area are largely uneducated about the role of surface-pressure phase distributions in the production of lifting-surface structural vibrations and HCF failures.

Therefore, what follows is a brief analytical example illustrating the possible influence of chordwise phase distributions on time-resolved surface-pressure response and modal forcing. It is intended that this example underscores, or even introduces, the importance of accurately considering phase distributions in lifting-surface response models, while also reinforcing the need for continued examination of lifting-surface phase distributions under various, even simplified, forcing conditions.

Consider an infinite-span flat-plate lifting surface having a chord extending from $-1.0 < x/c < 1.0$, where the surface is placed in an incompressible inviscid fluid. If the lifting-surface is subjected to a propagating sinusoidal disturbance, and it is assumed that the ingested disturbance is not distorted by interaction with the flat plate, the unsteady differential-pressure distribution along the lifting surface can be described in terms of a periodic function having some amplitude, frequency and phase. This function is given by

$$\Delta p'(x/c,t) = a(k)\rho_\infty U_\infty \Delta C_p'(x/c)\sin[\omega t + \phi(x/c)] \qquad \textbf{(2.3)}$$

where $\Delta C_p'$ is predicted by Sears in Eq. (2.1).

Using Eqs. (2.1) and (2.3), non-dimensional unsteady surface-pressure time series at various *x/c* locations are computed, as shown in Figures 2-3 and 2-4, for two separate phase distributions. In the non-varying phase case (i.e., $\phi(x/c) = 0$) of Figure 2-3, each *x/c* time-series is found to be in phase, reflecting instantaneous chordwise response to each propagating disturbance. This corresponds to the lifting-surface phase distribution of Sears. Conversely, for the chordwise-varying phase case (i.e., $\phi(x/c) \neq 0$) of Figure 2-4, each *x/c* location responds sequentially to the propagating disturbances. Note that the phase distributions of Figures 2-3 and 2-4 assume a constant phase change, or constant disturbance propagation speed, between each chordwise lifting-surface location.

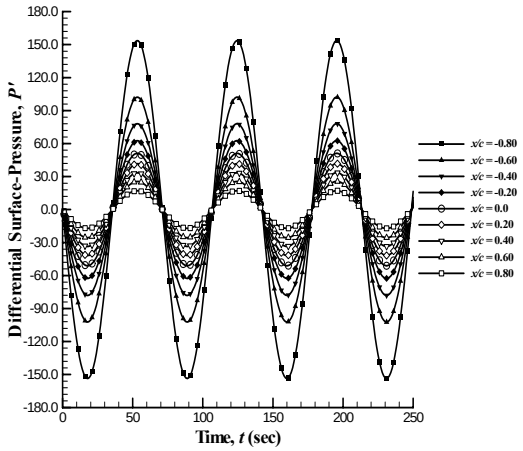

Figure 2-3 Unsteady Differential Surface-Pressure Time Series: ($\phi(x/c) = 0$).

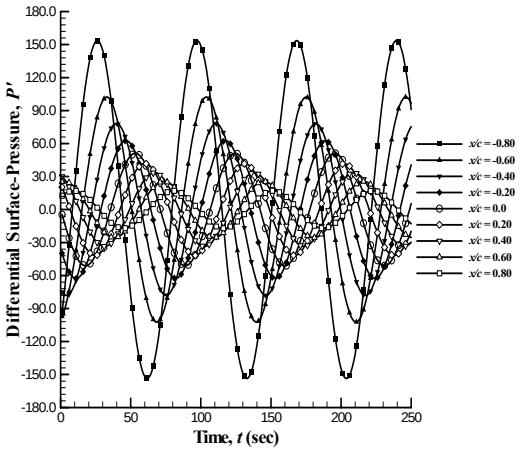

Figure 2-4 Unsteady Differential Surface-Pressure Time Series: ($\phi(x/c) \neq 0$).

Figures 2-5 and 2-6 exhibit corresponding surface-pressure distributions (computed from Figures 2-3 and 2-4) at selected times of t = 1, 45, 89, and 130 μs, for the two examined phase distributions. For the non-varying phase case of Figure 2-5, unsteady surface-pressure alternates continuously from positive to negative pressure due to the assumed sinusoidal nature of the forcing disturbance. At no time during the oscillation cycle, however, does the differential surface-pressure have both negative and positive chordwise components. In contrast, unsteady surface pressures corresponding to the chordwise-varying phase case, as shown in Figure 2-6, have multiple pressure-node locations, where these node locations change chordwise position with time. Furthermore, the chordwise-varying phase case alters the shape of the surface-pressure distribution, particularly along the forward half of the lifting surface.

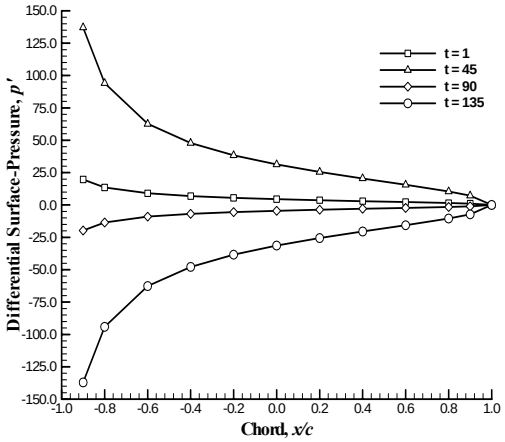

Figure 2-5 Unsteady Differential Surface-Pressure Variation with Chord: ($\phi(x/c) = 0$).

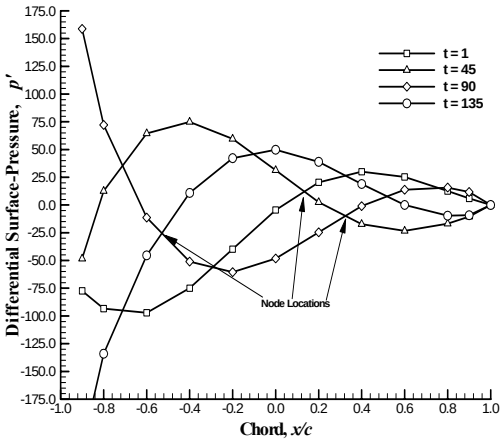

Figure 2-6 Unsteady Differential Surface-Pressure Variation with Chord:($\phi(x/c) \neq 0$).

Chordwise integration of the surface-pressures in Figures 2-5 and 2-6 provides a maximum unsteady force, or lift, of 140 and 80.0, for the $\phi(x/c) = 0$ and ($\phi(x/c) \neq 0$) cases, respectively. Given these lift differences, it may be inferred that chordwise-varying phase may be desirable in terms of reducing unsteady aerodynamic loading. However, the integration process ignores modal forcing of the lifting surface. The unsteady generalized force on a particular structural mode, *m*, can be computed through the integral of the dot-product between the examined mode shape and surface-pressure distribution over the lifting-surface chord. Thus, for the current example, the generalized force on a particular structural mode can be written as

$$f_m(t) = \int_{-1}^{+1} [\Delta p'(x/c,t)\hat{n}].[\vec{\psi}_m(x/c)]d(x/c) \qquad \textbf{(2.4)}$$

A simply supported, infinite-span, two-dimensional lifting surface has an infinite number of mode shapes grouped into two families. Rigid-body mode shapes correspond to plunging and pitching oscillations of the lifting surface, while flexible-body mode

shapes correspond to elastic structural deflections. Several flexible-body mode shapes are illustrated in Figure 2-7, for the first three modes, along with the first rigid-body mode.

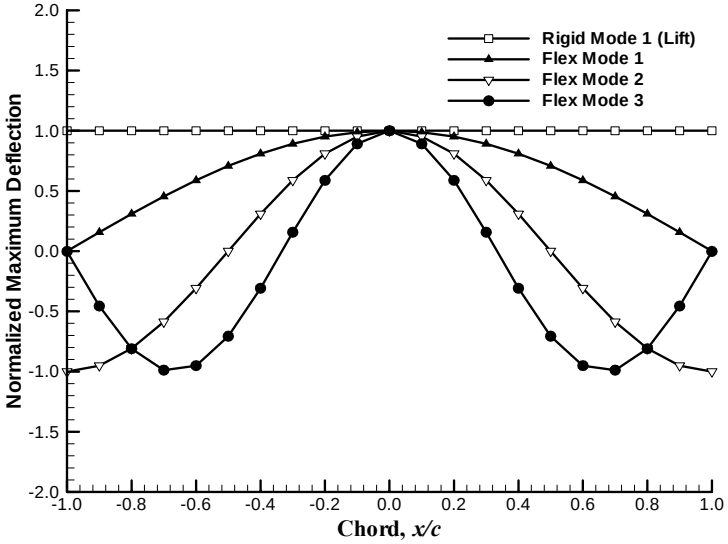

Figure 2-7 Rigid-Body and Flexible-Body Mode Shapes for a Simply Supported, Infinite-Span, Two-Dimensional Lifting Surface.

Accurate predictions of time-resolved generalized forces on each structural mode are important to avoid structural vibrations and HCF failure. To emphasize this fact, the surface-pressure distributions of Figures 2-5 and 2-6 are input into Eq. (2.4) along with the mode shapes of Figure 2-7, producing a generalized force on each examined structural mode. The maximum generalized forces obtained through this exercise are presented in Figure 2-8 and plotted versus mode number for the two separate chordwise phase distributions. Note that "mode 0" in Figure 2-8 corresponds to the first rigid-body structural mode, or lift-mode, while the higher modes correspond to the first, second and third flexible-body modes, respectively. Examining Figure 2-8, the non-varying phase distribution shows a canonical decay in force with increasing mode number. In contrast, the chordwise-varying phase distribution exhibits decreased force in the lower-order

modes and significantly amplified force in higher-order modes. Therefore, modal force is found to be a function of chordwise phase distribution.

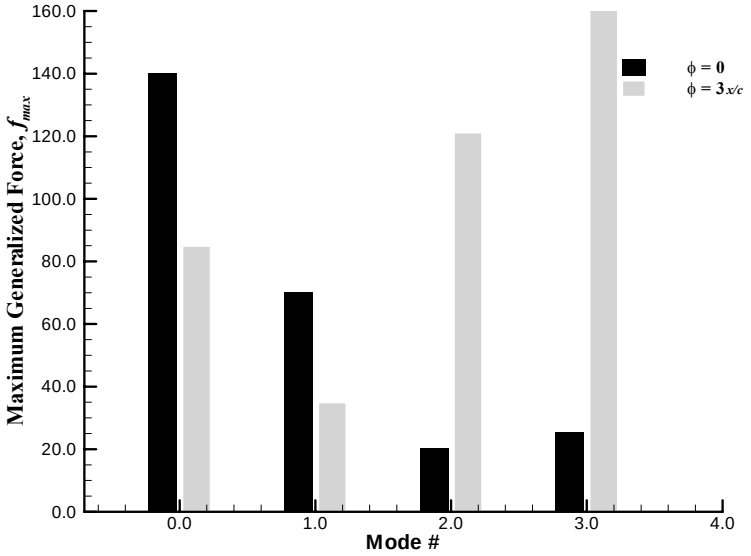

Figure 2-8 Maximum Generalized forces on Structural Modes for Various Phase Distributions.

The above unsteady-forcing example emphasizes several facts. First, chordwise-varying phase may alter time-resolved surface-pressure amplitude distributions along a lifting-surface chord. Second, chordwise-varying phase distributions also produce surface-pressure node locations, where these node locations may change position with time. Third, generalized modal forces are altered by chordwise phase distribution. In particular, higher-order modal forces may be amplified by chordwise-varying phase distributions, generating greater mechanical stresses at spatial and temporal frequencies not predicted for the non-varying phase case. Such possible variations in lifting-surface modal forcing may, if inaccurately predicted, lead to decreased fatigue life for the lifting structure.

In all, unsteady surface-pressure phase distributions are clearly important to the unsteady forcing problem. This is particularly evident when one considers that some

current unsteady-forcing predictive tools employ the results of Sears as a basis of their predictions. Fortunately, an increasing number of forced-response predictive tools are not based on the results of Sears, opting rather for direct numerical simulation of the governing fluid dynamic equations. Validation of these computational tools has proven to be laborious and heavily dependent on the availability of properly posed benchmark data. As such, few comparisons between computed an experimentally determined surface-pressure phase distributions have been made. This is not to say that benchmark phase data are not available, but rather that the significance of the data is not well understood or properly examined. In fact, what is intriguing about the previously reported phase data in this chapter is not their lack of inclusion in the open literature, but the almost complete disregard as to their importance and correlation with computed/measured trends. Much of the available computational/experimental phase data do not correspond to the constant disturbance-speed assumptions made in the above example; in fact, certain data sets show almost no discernable trend with chord. Therefore, while the above example emphasizes the importance of considering chordwise-varying phase for a constant propagation speed, the validity of assuming a constant disturbance propagation speed is unclear. Moreover, the effects of phase deviations from the assumed constant-speed disturbance phase on lifting-surface response are unknown.

2.3 CURRENT RESEARCH OBJECTIVE

Given the continued need for examining the influence of lifting-surface chordwise phase distribution on surface-pressure response, the current research presents a fundamental study of surface-pressure phase. In particular, two-dimensional, time-accurate, RANS simulations are performed to examine the fundamental physics leading

to surface-pressure phase. Attempts are made to reveal the essential dependencies of that phase on forcing configuration. Simulations are performed for a variety of lifting surface geometries and forcing conditions utilizing the commercially available CFD algorithm, Fluent (v. 6.0).

3 CHAPTER 3

COMPUTATIONAL METHODOLOGY AND SETUP

This chapter discusses the computational methodology and setup employed in the present research. A description of the airfoil and stator-vane cascade geometries, as well as associated boundary conditions, is given. In-depth discussions regarding FLUENT and its companion mesh generation software, GAMBIT, are also provided along with a development of the UDF (user-defined function) generating the airfoil forcing function.

3.1 AIRFOIL GEOMETRY AND BOUNDARY CONDITIONS

Surface-pressure phase data on forward-forced lifting surfaces are examined using the commercially available CFD algorithm, FLUENT (v. 6.0). Simulations were performed with four symmetric NACA airfoil profiles of 10, 12, 15 and 20% thickness (relative to chord), two cambered airfoils of 2 and 6% camber (relative to chord), two mean-flow attack angles of 5 and 10 degrees and two forcing-disturbance frequencies of 150 Hz and 300 Hz. In all simulations, periodic boundary conditions were enforced on the upper and lower computational boundaries located about an otherwise isolated lifting surface, as illustrated in Figure 3-1. These periodic boundaries simulate the influence of neighboring surfaces, or a series of airfoils in cascade; an airfoil cascade configuration was selected for comparison with previous experimental configurations. A cascade solidity of 4.0, representing weak surface-to-surface pitchwise aerodynamic coupling as

compared to modern cascaded blade rows, was selected for the majority of simulations; however, other solidities equaling 2.0 and 6.0 were also briefly investigated. Pressure-inlet and pressure-outlet boundary conditions were set for the computational inlet and outlet boundaries, respectively (see Figure 3-1).

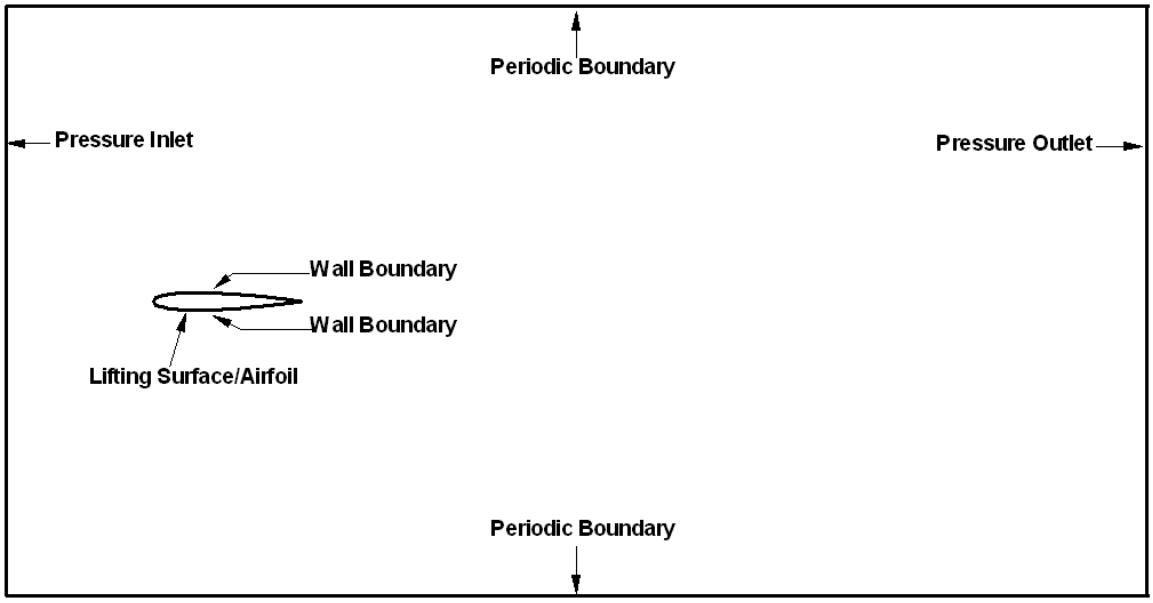

Figure 3-1 Airfoil-Cascade Computational Boundaries.

3.2 STATOR-VANE GEOMETRY AND BOUNDARY CONDITIONS

In addition to the simplified NACA airfoil-cascade configuration, a more complicated cascade configuration was also examined. This configuration employed aerodynamically loaded vanes that mimicked the two-dimensional geometry of the stator-vane row in the fan compression stage of a F109 turbofan engine (at 87.8% span). The high cascade solidity and double circular-arc profile of the stator-vane row required definition of additional geometric variables beyond the simplified NACA airfoil cascade. A complete discussion of the cascade geometry and nomenclature is provided in Appendix A. In the present investigation, a vane-centered computational mesh was

selected to model the stator-vane cascade geometry, with the simulated vane centered in the computational domain, as shown in Figure 3-2. Periodic boundary conditions were enforced at mesh boundaries above and below the vane, simulating the influence of other vanes in cascade. The periodic boundaries were set at mid-pitch between vanes, using the vane camber-line arc to define the boundary geometry. The stator-vane inlet flow angle was set to be 21.9^{o}, while the exit flow was set to be -20.6^{o}, based on previous experimental data [Fabian, 1995]. The stator vanes possess a maximum camber and thickness of 12% and 8% relative to chord, respectively. Vane profile coordinates are listed in Appendix B, reproduced from [Fabian, 1995]. Table 3.1 provides characteristics of the modeled stator-vane cascade geometry. Like the NACA-airfoil cascade, pressure-inlet and pressure-outlet boundary conditions were set for the stator-vane computational inlet and outlet boundaries, respectively.

Table 3.1 Modeled Stator-Vane Cascade Geometry.

Parameter	***Value***
Vane Spacing, S	0.84 m
Solidity, σ	1.524
Inlet Flow Angle, α_1	21.9^{o}
Exit Flow Angle, α_2	-20.6^{o}

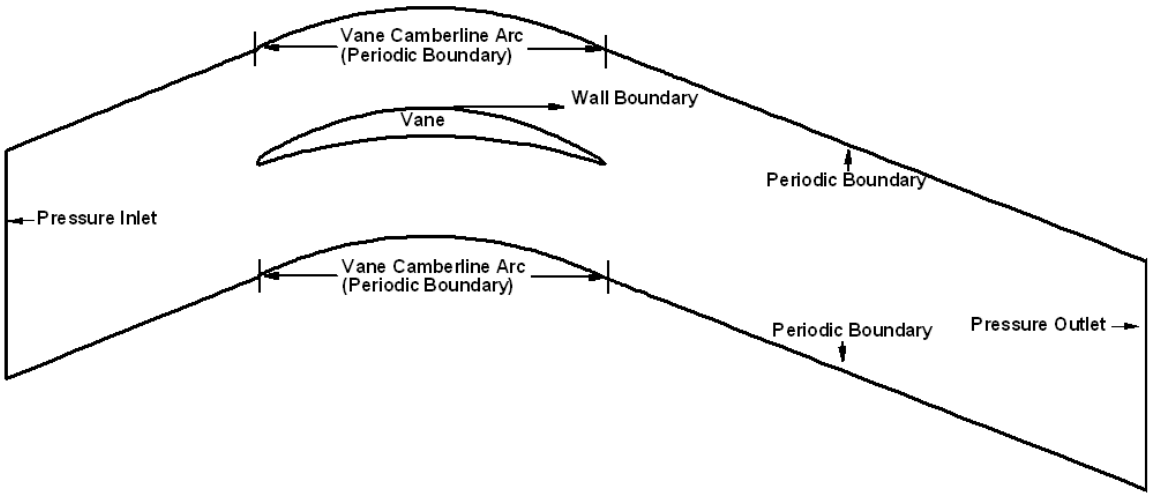

Figure 3-2 Stator-Vane Cascade Computational Boundaries.

3.3 GENERAL FLUENT SOLVER DESCRIPTION

FLUENT is a state-of-the-art commercially available flow-solver with capability for modeling unsteady, compressible, viscous flows via numerical solution of the governing fluid dynamic equations. Numerical simulation of the governing fluid dynamic equations in FLUENT is accomplished via a control-volume based (finite-volume) discretization technique. This technique integrates governing integral equations established within discrete elements (i.e. finite volumes, or cells) of the mesh, resulting in a system of algebraic equations for dependent variables such as velocity and pressure. The discretized algebraic system is then linearized and solved numerically to yield updated variable values at each iteration/time step, using (in the present investigation) implicit linearization schemes. Solution interpolation between adjacent element-face regions is accomplished via one of several user-defined methods, including first-order upwind, second-order upwind and power-law interpolation. First-order or second-order accurate spatial/temporal discretization is available in FLUENT, where second-order accuracy is default for coupled solutions. To aid convergenence in highly non-linear

problems, FLUENT allows user-defined controls over under-relaxation and courant (CFL) numbers.

Numerical solutions are achieved through one of three user-selected solvers, including: segregated, coupled-implicit, or coupled-explicit solvers. The segregated solver linearizes the governing equations implicitly with respect to the dependent variables, solving the resulting set of equations sequentially. Linearized momentum equations are solved individually for fluid velocity, followed by corrective step in which velocity is adjusted based on user-selected velocity-pressure correlations to satisfy continuity. Conversely, coupled solvers simultaneously solve the set of governing equation defining the dependent variables, where the equation set can be linearized either explicitly or implicitly. For implicit linearization, Gauss-Seidel solvers are employed in conjunction with an algebraic multi-grid (AMG) method to solve the system(s) of equations. Conversely, with explicit linearization, dependent-variable solutions are updated at each time step using a multi-step Runge-Kutta solver, with the additional option of employing a full approximation storage (FAS) multi-grid scheme to accelerate convergence. FLUENT allows users to specify several boundary condition types. Supported inlet and outlet boundary conditions include: pressure-inlet, velocity-inlet, mass-flow-inlet, inlet-vent, intake-fan, pressure-outlet, pressure-far-field, outflow, outlet-vent, and exhaust-fan-boundaries. Similarly, wall, repeating, and pole boundary types include: wall, symmetry, periodic and axis boundaries.

For the present research, two-dimensional numerical simulations of the Reynolds-averaged Navier-Stokes equations were accomplished in FLUENT via a finite-volume technique. A coupled solution methodology (Section 3.3.1) was selected, in which the

fully coupled systems of equations defining the dependent variables in each cell were discretized, linearized, and solved simultaneously at each iteration/time step. Linearized equation systems were solved using a Gauss-Seidel solver in conjunction with an algebraic multi-grid (AMG) method. Second-order accurate spatial and temporal discretization was employed for all simulations, with implicit linearization. Simulations were fully viscous, utilizing a standard k-ε turbulence model (see Section 3.3.3).

3.3.1 Coupled Solution Method

The coupled solver used for the current simulations solves the governing equations of continuity, momentum, and (where appropriate) energy and species transport simultaneously (i.e., coupled together). Governing equations for additional scalars (i.e., turbulence, etc.) are solved sequentially using a segregated approach. Since the set of governing equations is non-linear (and therefore coupled), several sub-iterations of the solution procedure are performed at each time step before a converged solution is obtained at that time step. Each sub-iteration consists of the steps illustrated in Figure 3-3 and outlined below:

1. Fluid properties are updated, based on the current solution. (If the calculation has just started, fluid properties are updated based on an initial solution.)
2. Continuity, momentum, and (where appropriate) energy and species equations are solved simultaneously.
3. Where appropriate, equations for scalars such as turbulence and radiation are solved using the previously updated values of the other variables.
4. A check for convergence of the equation set is made.

These steps are continued until the convergence criteria are met at each time step. [FLUENT, 2001]

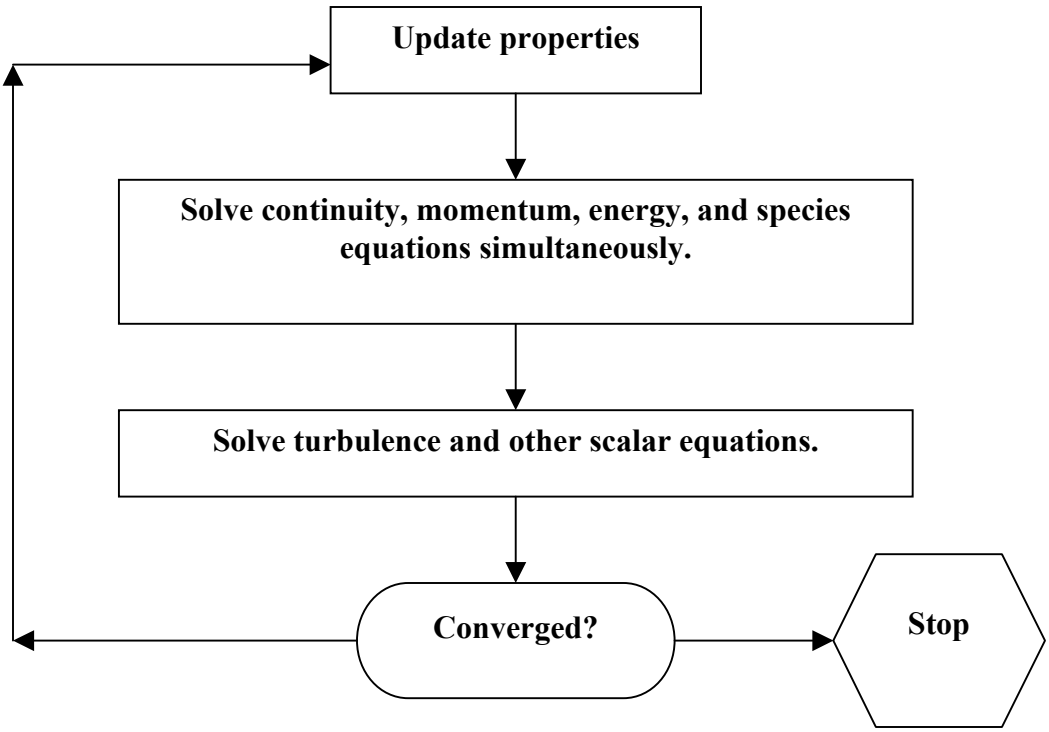

Figure 3-3 Overview of the Coupled Solution Method [Fluent, 2001].

3.3.2 Reynolds-Averaged Navier-Stokes (RANS) Equations

The Reynolds-averaged Navier-Stokes (RANS) equations were selected to represent transport equations for ensemble-averaged, or mean, flow quantities, with all turbulence scales modeled. The approach of permitting a solution for just the mean-flow variables greatly reduces the computational effort. If the mean flow is steady, the governing equations will not contain time derivatives and a steady-state solution can be obtained economically. A computational advantage is also provided in required time-accurate simulations, as time step may be determined by global unsteadiness in the mean flow rather than turbulent unsteadiness. The RANS approach models turbulent flow

quantities, through such well-known models as the Spalart-Allmaras, *k-ω, k-ε*, and RSM models [FLUENT, 2001].

3.3.2.1 Reynolds (Ensemble) Averaging

In Reynolds averaging (i.e., ensemble averaging solution variables in the instantaneous (exact) Navier-Stokes equations are decomposed into mean (ensemble-averaged or time-averaged) and fluctuating components (about the mean). For velocity components, this decomposition equals

$$u_i = \overline{u}_i + u_i' \tag{3.1}$$

Likewise, for pressure and other scalar quantities:

$$\phi = \overline{\phi} + \phi' \tag{3.2}$$

where ϕ denotes a scalar such as pressure energy or species concentration.

Substituting these forms of the flow variables into the instantaneous continuity and momentum equations, and taking a time (or ensemble) average (and dropping the overbar on the mean velocity, $\overline{u}$), yields the ensemble-averaged continuity and momentum equations. These equations can be written in Cartesian tensor form as:

$$\frac{\partial \rho}{\partial t} + \frac{\partial}{\partial x_i}(\rho u_i) = 0 \tag{3.3}$$

$$\frac{\partial}{\partial t}(\rho u_i) + \frac{\partial}{\partial x_j}(\rho u_i u_j) = \frac{\partial p}{\partial x_i} + \frac{\partial}{\partial x_j}\left[\mu\left(\frac{\partial u_i}{\partial x_j} + \frac{\partial u_j}{\partial x_i} - \frac{2}{3}\delta_{ij}\frac{\partial u_1}{\partial x_1}\right)\right] + \frac{\partial}{\partial x_j}(-\rho u_i' u_j') \tag{3.4}$$

Equations (3.3) and (3.4) are also known collectively as the RANS equations.

3.3.3 k – ε Turbulence Model

In the present application, a standard *k-ε* turbulence model was used to simulate the effects of turbulence. The standard *k-ε* model is a semi-empirical model based on model transport equations for turbulence kinetic energy, *k*, and it dissipation rate. The model transport equation for *k* was derived from an exact equation, while the model transport equation for ε was obtained using physical reasoning. Equations for *k* and ε are given as follows

$$\frac{\partial}{\partial t}(\rho k)+\frac{\partial}{\partial x_i}(\rho k u_i)=\frac{\partial}{\partial x_j}\left[(\mu+\frac{\mu_t}{\sigma_k})\frac{\partial k}{\partial x_j}\right]+G_k+G_b-\rho\varepsilon-Y_M+S_k \qquad \textbf{(3.5)}$$

and

$$\frac{\partial}{\partial t}(\rho \varepsilon)+\frac{\partial}{\partial x_i}(\rho \varepsilon u_i)=\frac{\partial}{\partial x_j}\left[(\mu+\frac{\mu_t}{\sigma_\varepsilon})\frac{\partial \varepsilon}{\partial x_j}\right]+C_{1\varepsilon}\frac{\varepsilon}{k}+(G_k+C_{3\varepsilon}G_b)-C_{2\varepsilon}\rho\frac{\varepsilon^2}{k}+S_\varepsilon \qquad \textbf{(3.6)}$$

where,

$C_{1\varepsilon}, C_{2\varepsilon}, C_{3\varepsilon}, \sigma_k$ and σ_ε are model constants nominally having the following values:

$$C_{1\varepsilon} = 1.44$$

$$C_{2\varepsilon} = 1.92$$

$$C_{3\varepsilon} = 0.09$$

$$\sigma_k = 1.0$$

$$\sigma_\varepsilon = 1.3$$

The above values are default in FLUENT, and are employed in the current investigation.

3.3.4 Finite-Volume Discretization Methodology

FLUENT uses a control-volume-based technique to convert governing fluid dynamic equations to algebraic equations that can be solved numerically. This control-volume technique consists of integrating the governing equations about each control volume (or cell) in the computational mesh, yielding discrete equations that conserve each quantity on a control-volume basis. Discretization of the governing equations can be illustrated most easily by considering the steady-state conservation equation for transport of a scalar quantity, ϕ. This is demonstrated by the following equation written in integral form for an arbitrary control volume, *V,* as follows:

$$\oint \rho\phi\vec{v}d\vec{A} = \oint \Gamma_\phi \nabla_\phi d\vec{A} + \int_V S_\phi dV \tag{3.7}$$

The above equation is applied to each control volume, or cell, in the computational domain. Thus, discretization of Eq. (3.7) for a given control volume yields:

$$\sum_f^{N_{faces}} \rho_f \vec{v}_f \phi_f \vec{A}_f = \sum_f^{N_{faces}} \Gamma_\phi (\nabla\phi)_n \vec{A}_f + S_\phi V \tag{3.8}$$

All governing equations solved by FLUENT take the same general form as Eq. (3.8) and therefore readily apply to unstructured meshes composed of tetrahedra, as in the current investigation. FLUENT stores discrete values of the scalar ϕ at the cell centers. However, face values, of ϕ_f, are required for convection terms in Eq. 3.8 and therefore must be interpolated from adjacent cell-center values. This is accomplished using an upwind scheme.

3.3.5 Second-Order Upwind Scheme

For the present investigation, a second-order upwind scheme was selected. When second-order solution accuracy is desired in FLUENT, flow quantities at cell faces are computed using a multi-dimensional linear reconstruction approach. In this approach, higher-order accuracy is achieved at cell faces through a Taylor series expansion of the cell-centered solution about the cell centroid. Thus when second-order upwinding is selected, a face value ϕ_f is computed using the following expression:

$$\phi_f = \phi + \nabla\phi \Delta\vec{s} \tag{3.9}$$

where ϕ and $\nabla\phi$ are the cell-centered value and its gradient, and $\Delta\vec{s}$ is the displacement vector from the cell centroid to the face centroid. This formulation requires the determination of the gradient $\nabla\phi$ in each cell, where this gradient is computed using the divergence theorem,

$$\nabla\phi = \frac{1}{V}\sum_{f}^{N_{faces}} \tilde{\phi}_f \vec{A} \tag{3.10}$$

In Eq. (3.9) face values $\tilde{\phi}_f$ are computed by averaging ϕ between cells adjacent to the face in question. Finally, the gradient $\nabla\phi$ is value-limited so that no new maxima or minima are introduced in the examined cell region.

3.3.6 Second-Order Time Discretization

For transient simulations, the governing equations must be discretized in both space and time. Spatial discretization for time-dependent equations is identical to the steady-state case; however, temporal discretization involves integration of every term in

the governing differential equations over one time step, Δt. The integration of transient terms is straightforward, as described below.

A generic expression for the time evolution of a variable ϕ is given by:

$$\frac{d\phi}{dt} = F(\phi) \tag{3.11}$$

where the function F incorporates both spatial and temporal discretization. If the time derivative is discretized to first-order approximation, an expression for the discretized derivative may be written as

$$\frac{\phi^{n+1} - \phi^n}{\Delta t} = F(\phi) \tag{3.12}$$

While a second-order accurate temporal discretization is given by

$$\frac{3\phi^{n+1} - 4\phi^n + \phi^{n-1}}{2\Delta t} = F(\phi) \tag{3.13}$$

Once the time derivative has been discretized, a choice remains for evaluating $F(\phi)$. The method employed here to evaluate $F(\phi)$ at a future time level, such as

$$\frac{\phi^{n+1} - \phi^n}{\Delta t} = F(\phi^{n+1}) \tag{3.14}$$

This is referred to as "implicit" integration as ϕ^{n+1} in a given cell depends on both sides of Eq. (3.14), giving

$$\phi^{n+1} = \phi^n + \Delta t F(\phi^{n+1}) \tag{3.15}$$

The implicit relation of Eq. (3.15) can be solved iteratively by initializing ϕ^{n+1} to ϕ^t and iterating the equation

$$\phi^t = \frac{4}{3}\phi^n - \frac{1}{3}\phi^{n-1} + \frac{2}{3}\Delta t F(\phi^t) \tag{3.16}$$

for second-order formulation, until ϕ^t stops changing (i.e., converges). At that point, ϕ^{n+1} is set equal to ϕ^t. The advantage of a fully implicit scheme is its unconditional stability with respect to time-step size.

3.3.7 Linearization Methodology

In the coupled-solution method the discrete, non-linear governing equations are linearized to produce a system of equations for the dependent variables in every computational cell. The resultant linear system is then solved to yield an updated flow-field solution. The manner in which the governing equations are linearized may take an implicit or explicit form with respect to the dependent variable (or set of variables) of interest. For the present analysis a coupled-solution methodology with implicit linearization was used. This results in a system of linear equations with *N* equations for each cell in the domain, where *N* is the number of coupled equations in the set. Because there are *N* equations per cell, this is sometimes called a block system of equations. A point-implicit (i.e., block Gauss-Seidel) linear equation solver is used in conjunction with an algebraic multigrid (AMG) method to solve the resultant block system of equations for all *N* dependent variables in each cell. For example, linearization of the coupled continuity, *x*-, *y*-, *z*-momentum, and energy equation set will produce a system of equations in which *p, u, v, w*, and *T* are unknowns. Simultaneous solution of this equation system (using the block AMG solver) yields at once updated pressure, velocity, and temperature fields.

3.3.8 Periodic Boundary Conditions

Periodic boundary conditions are advantageous when the physical geometry of interest and the expected flow solution has a spatially periodic nature. The assumption of spatial flow periodicity implies the velocity components repeat themselves in space as follows:

$$u(\vec{r}) = u(\vec{r} + \vec{L}) = u(\vec{r} + 2\vec{L}) = ...$$

$$v(\vec{r}) = v(\vec{r} + \vec{L}) = v(\vec{r} + 2\vec{L}) = ... \quad \textbf{(3.17)}$$

where $\vec{r}$ is the position vector and $\vec{L}$ is the periodic length vector of the domain considered. For viscous flows, the spatially distributed pressure field may not be periodic in the sense of the above Eq. (3.18). Instead, pressure drop between modules maybe periodic in space, giving

$$\Delta p = p(\vec{r}) - p(\vec{r} + \vec{L}) = p(\vec{r} + \vec{L}) - p(\vec{r} + 2\vec{L}) = ... \quad \textbf{(3.18)}$$

If the coupled solver is selected in FLUENT, Δp maybe specified as a constant value at any periodic boundary.

3.3.9 Standard FLUENT Inlet/Outlet/Wall Boundary Conditions

3.3.9.1 Pressure-Inlet Boundary Conditions

Pressure-inlet boundary conditions define fluid pressure at flow inlets, along with all other scalar properties of the flow. They are suitable for both incompressible and compressible flow calculations [Fluent, 2001]. Pressure-inlet boundary conditions are typically specified in FLUENT when inlet pressure is known but flow rate and/or velocity is not known. When flow enters through a pressure-inlet boundary, FLUENT enforces the input boundary pressure as the fluid total-pressure at the inlet plane, p_0. In

steady-state incompressible flow, the inlet total-pressure and static pressure p_s are related at the inlet velocity via Bernoulli's equation:

$$p_0 = p_s + \frac{1}{2}\rho v^2 \tag{3.19}$$

In compressible flow, the total-pressure and static pressure are related by

$$p_0 = p_s(1 + \frac{\gamma - 1}{2} M^2)^{\frac{\gamma}{\gamma - 1}} \tag{3.20}$$

3.3.9.2 Pressure-Outlet Boundary Condition:

As specified earlier, a pressure-outlet boundary condition was selected at the computational outlet plane for all simulations. Pressure-outlet boundary conditions in FLUENT require the specification of a static (gauge) pressure at the outlet boundary. For a subsonic flow, FLUENT enforces the input boundary pressure as the fluid static pressure at the outlet plane, and extrapolates all other flow conditions to the outlet from the interior of the domain.

3.3.10 Operating Pressure

In the present investigation, the operating pressure condition in FLUENT was set to 0 Pa, allowing all pressure calculations to be treated as gauge pressures. Setting the computational operating pressure equal to 0 Pa is significant as it reduces round-off error problems. In low-Mach number flows, overall pressure changes are typically small compared to the atmospheric static pressure, and therefore can be significantly affected by numerical round-off error. Moreover, FLUENT always uses gauge pressure for all its calculations, as such setting the operating pressure equal to zero makes gauge and absolute pressures equivalent.

3.4 UDF DESCRIPTION

Aerodynamic forcing of the examined lifting surfaces was achieved by modeling waveform characteristics similar to a passing wake, as might be found in a rotor-stator compression stage. In doing so, a user-defined function (UDF) was written in FLUENT. A UDF can be dynamically loaded into the FLUENT solver to enhance standard features of the available code. Such functions are written in the C programming language, allowing standard C library functions to be used, as well as predefined macros (provided by Fluent Inc.).

A UDF can be implemented as an interpreted or compiled function. An interpreted UDF is read in and interpreted at run time. Alternatively, a compiled UDF is grouped into shared libraries when it is compiled and linked with the standard FLUENT executable. An interpreted UDF is simple to use but imparts coding and speed limitations. A compiled UDF executes faster and has no coding limitations, but requires more effort to develop and implement. The current investigation employs a compiled UDF.

3.4.1 Development Logic/Procedure

The developed inlet UDF established an inlet total-pressure profile, simulating the movement of a rotor-blade wake passing across the computational inlet. The following steps were employed to code and implement the UDF in FLUENT for the present investigation.

1. Define the wake model.
2. Create a C source code file
3. Start FLUENT and setup the case file.

4. Compile the C source code
5. Activate the UDF in FLUENT.

The first step to generate and implement the inlet UDF was to develop an analytical model of a typical rotor-blade wake; this wake representing the aerodynamic forcing function for the examined lifting surfaces. Experimental low-speed compressor investigations by Reynolds et. al (1979) showed that rotor-blade wake profiles approximately follow a Gaussian profile. As such, a simple aerodynamic forcing-function model was developed using a Gauss function. This model is characterized by the wake centerline defect, W_{dc}, and the semi-wake width, δ (see Figure 3-4). An equation for total-pressure deficit produced by a rotor-blade wake function was defined as

$$P_{ti} = W_{dc} e^{[-\delta(\frac{y}{c}-t)^2]} \qquad 3.21$$

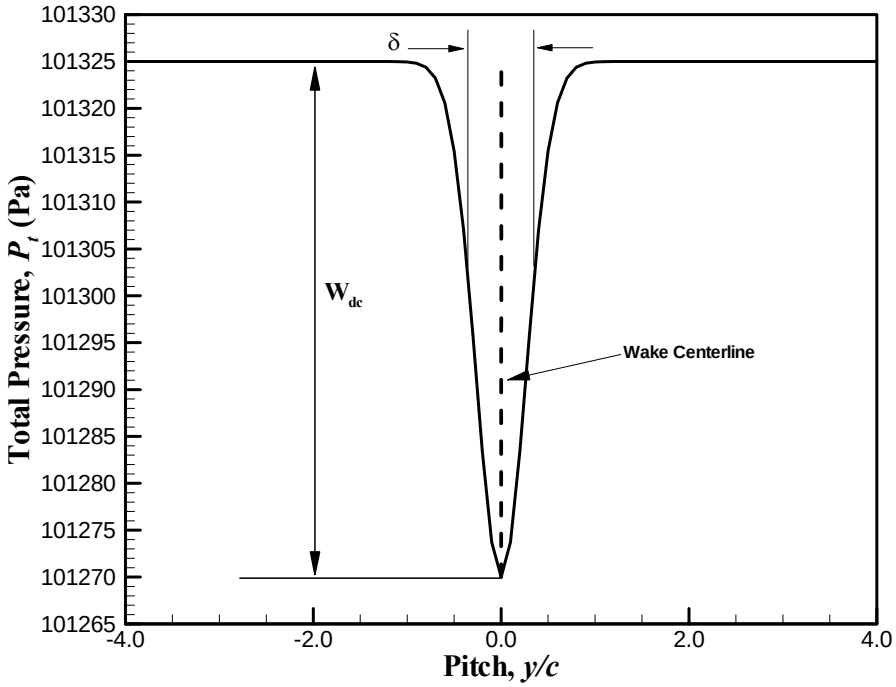

Figure 3-4 Rotor Wake Characteristics.

Values for the wake centerline defect, W_{dc}, and the semi-wake width, δ, were optimized to obtain the waveform shown in Figure 3-4.

Having developed the aerodynamic forcing-function model, a C source code was written. This source code incorporated standard C library functions as well as predefined macros (provided by FLUENT). These include the DEFINE_PROFILE macro, the F_CENTROID macro, begin_f_loop macro and F_PROFILE macro. The UDF (source code) written was compiled in FLUENT as an interpreted UDF and applied to the pressure-inlet boundary. A complete description of the developed UDF with a detailed discussion of each macro is provided in Appendix C.

3.5 COMPUTATIONAL GRID DESCRIPTION

The FLUENT software package contains an available pre-processor for geometry modeling and mesh generation known as GAMBIT. As such, the computational grids for the present investigation were created with GAMBIT grid generation software [FLUENT, 2001].

3.5.1 Gambit Grid Generation Software

Mesh generation for FLUENT simulations may be provided through its companion software, GAMBIT; however, select third-party software is also supported. GAMBIT is a graphically oriented software package mimicking many computer aided drawing (CAD) programs. GAMBIT allows users to graphically reproduce complex physical geometries of interest, and mesh these geometries using several user-selected mesh-generation algorithms. GAMBIT geometries are created by manipulating components such as edges, faces, and volumes that represent the physical system being

considered. Vertex coordinates for these components can be directly generated in GAMBIT or imported from existing data files. Created components can be rotated, translated, copied, split, united and subtracted from one another, to name a few operations, as is typical of most CAD software.

GAMBIT geometries can also be created in different coordinate systems, or multiple local coordinate systems, depending on the particular application. The software provides complete meshing flexibility in both two and three dimensions, featuring algorithms for structured quadrilateral and hexahedral meshes, unstructured triangular, tetrahedral, pyramid and wedge meshes, and mixed structured-unstructured meshes. GAMBIT also supports boundary-layer subroutines to construct structured meshes in close proximity to geometric walls, providing increased grid resolution in viscous boundary layers. So-called "boundary-layer meshes" can be coupled with unstructured meshes in the adjacent potential flow, forming a hybrid mesh. Mesh density and distribution are easily controlled via direct input of nodal positions, or through appropriate sizing functions that concentrate mesh points around user-defined regions. User input during mesh construction allows high-density elements to be concentrated in areas of high-flow gradients.

3.5.2 Grid Methodology

3.5.2.1 Airfoil-Cascade Mesh

The methodology followed to create meshes for the parametric NACA airfoil-cascade analysis was as follows. Airfoil geometry (obtained from XFOIL) was read into GAMBIT as vertex data, and interpolation was performed between vertex data to create the basic airfoil shape. Once airfoil shape was defined, inlet and outlet boundary planes

were created. The inlet boundary was located one airfoil chord forward of the airfoil leading edge, while the outlet boundary was placed 16 chords downstream of the airfoil trailing edge. In order to reduce computational expense, only one airfoil was considered with periodic boundary conditions simulating the influence of neighboring cascaded airfoils. A two-dimensional hybrid mesh, consisting of a structured H-grid immediately surrounding the airfoil, and an unstructured triangular mesh representing the potential region outside of the airfoil boundary layer, was created. The resulting grid system, for the NACA 0012 airfoil profile, is represented in Figure 3-5. A detailed description of the boundary-layer mesh and its characteristics is provided in Section 3.5.2.1.1. Grid sizes employed for the airfoil-cascade meshes are provided in Section 3.5.2.1.2.

3.5.2.1.1 Grid Density and Grid Distribution

Grid node distributions employed for the airfoil-cascade parametric analysis are outlined in Table 3.2. The total number of mesh elements for the airfoil-cascade mesh equaled 26446, where 24246 were triangular mesh elements and 2200 were quadrahedral mesh elements. The Tri-Pave meshing scheme provided by GAMBIT was used to create the triangular mesh elements.

Table 3.2 Grid Distribution (Airfoil-Cascade Mesh).

Surface	***# of Nodes***
Inlet	100
Outlet	25
Periodic Boundary	150
Airfoil Suction Side	55
Airfoil Pressure Side	55

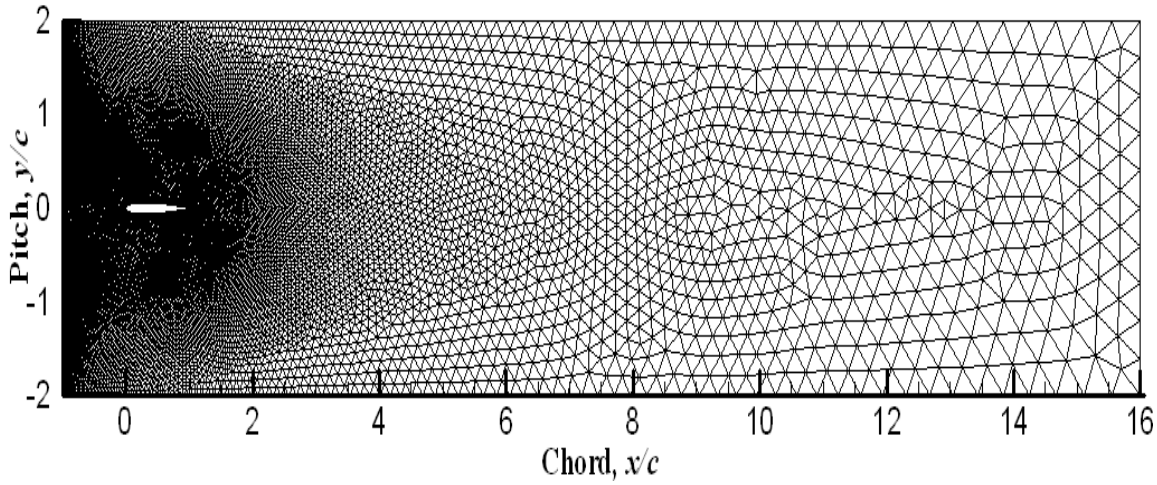

Figure 3-5 Airfoil-Cascade Mesh (NACA 0012 airfoil)

3.5.2.1.2 Boundary Layer (Viscous-Flow Region) Grid

As mentioned in Section 3.5.2.1, in the immediate region surrounding the airfoil a structured boundary-layer grid was generated. Boundary-layer grids in FLUENT define mesh node spacing in regions immediately adjacent to an edge and/or face. These grids control mesh density and location in a specific region of interest, here the upper (suction) and lower (pressure) surfaces of the airfoil.

In the case of the NACA airfoil-cascade simulations, the first boundary-layer nodes were positioned 0.12% (relative to chord) from the airfoil surface with a growth rate of 1.1, with the total number of boundary-layer mesh levels equaling 20. Table 3.3 outlines the boundary-layer mesh characteristics employed for the NACA airfoil-cascade simulations. Figure 3-6 depicts the structured boundary-layer mesh surrounding the NACA 0012 airfoil.

Table 3.3 Boundary-Layer Mesh Characteristics (Airfoil-Cascade Mesh).

Parameter	***Value***
Algorithm	Uniform
First Row Height	0.12% (relative to chord)
Growth Factor	1.1
No. of Rows	20
Total Depth	0.06873
Internal Continuity	On
Wedge Corner Shape	On
Transition Pattern	1:1

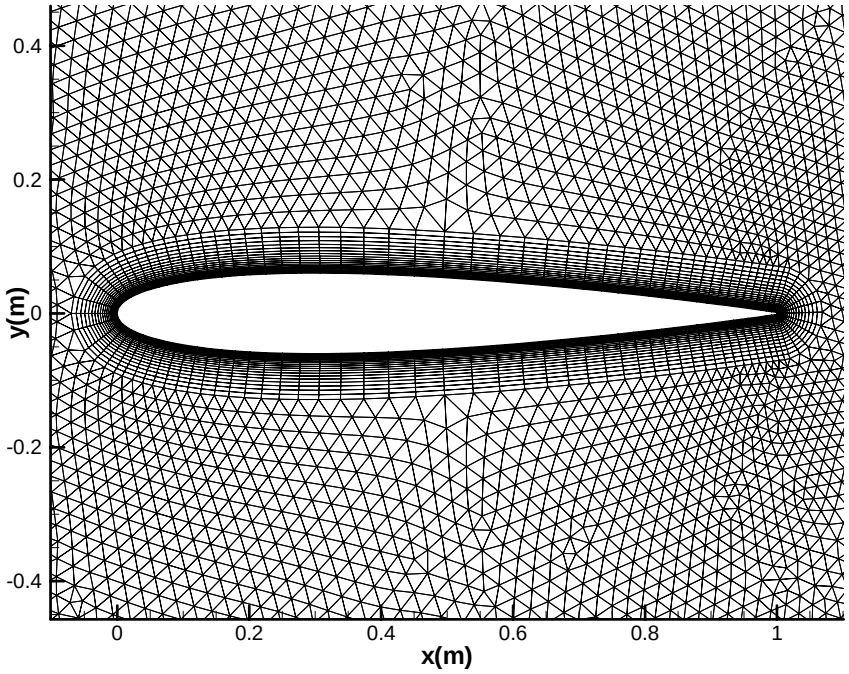

Figure 3-6 Structured Boundary-Layer Mesh Surrounding NACA 0012 Airfoil Geometry.

3.5.2.2 Stator-Vane Cascade Mesh

The steps followed to create the stator-vane cascade mesh are similar to those followed for the airfoil-cascade mesh. First, stator-vane coordinates (reproduced from Fabian [1995]) were read into GAMBIT as vertex data and interpolation was performed between vertices to create the stator-vane shape. Second, inlet and outlet boundary planes were created. Similar to the airfoil-cascade mesh, the inlet boundary was located one stator-vane chord forward of the vane leading edge, while the outlet boundary was placed 16 chords downstream of the vane trailing edge. The inlet and outlet boundaries were set exactly perpendicular to the *x*-axis with an inlet flow angle of 21.9^{o} and an outlet flow angle of -20.6^{o}. In order to reduce computational expense, only one stator-vane was considered with periodic boundary conditions simulating the influence of neighboring cascaded stator-vanes. A structured H-grid mesh was created for the entire stator-vane computational domain.

3.5.2.2.1 Grid Density and Grid Distribution

Grid node distributions employed for the stator-vane cascade mesh are outlined in Table 3.4. A successive ratio of 0.96 was used for periodic boundary edge-node grading, while bi-exponent type grading, with a ratio of 0.75, was selected for the stator-vane upper and lower surfaces. The total number of mesh elements for the stator-vane cascade mesh equaled 28000, all of which were quadrahedral mesh elements. The Map meshing scheme provided by GAMBIT was used to create the quadrahedral mesh elements. Figures 3-7 and 3-8 display the stator-vane cascade geometry and the modeled stator-vane mesh, respectively.

Table 3.4 Stator-Vane Cascade Mesh Node Distribution.

Surface	*# of Nodes*
Inlet	80
Outlet	80
Periodic Boundary	200
Airfoil Suction Side	75
Airfoil Pressure Side	75

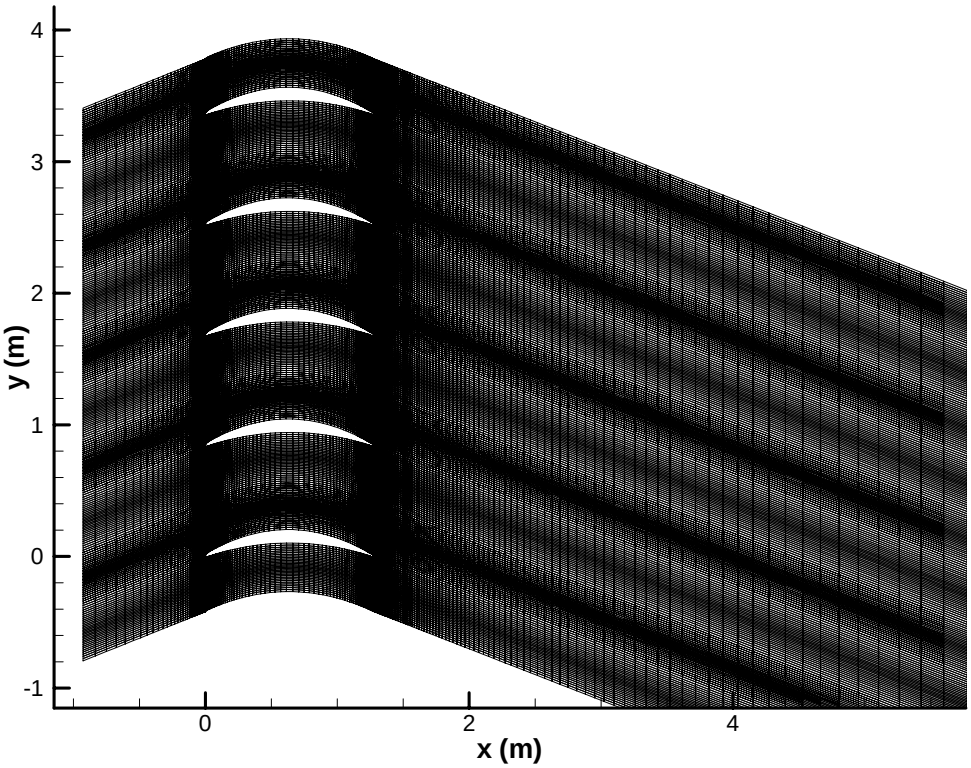

Figure 3-7 Stator-Vane Cascade.

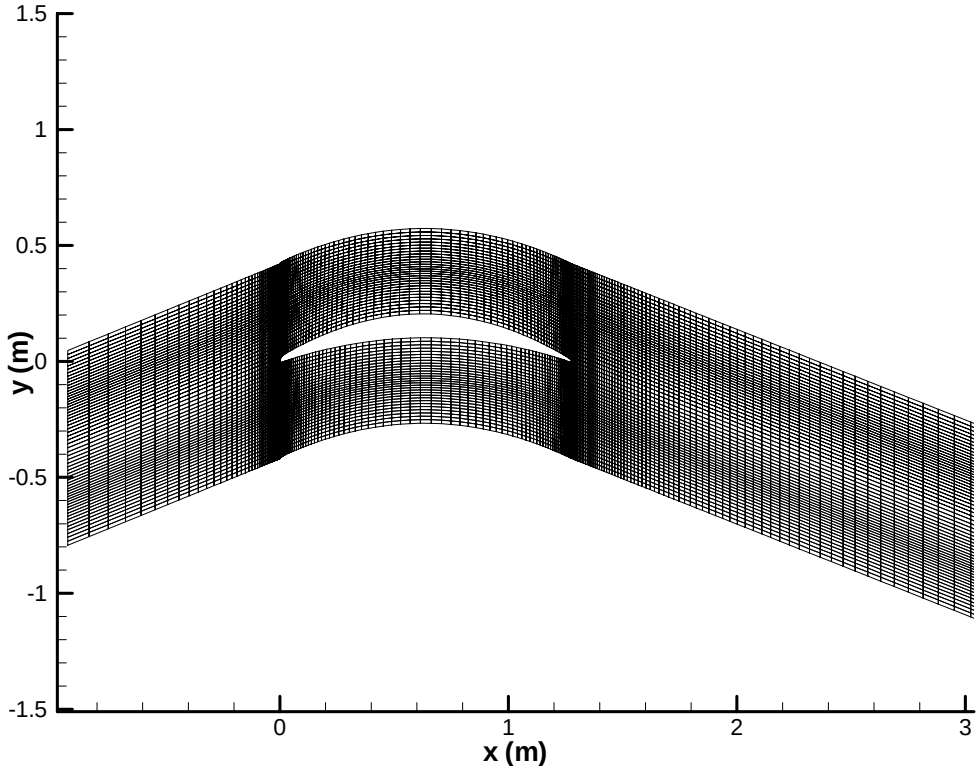

Figure 3-8 Modeled Stator-Vane Cascade Mesh.

3.6 Computational Setup

Table 3.5 summarizes the common inputs for all FLUENT simulations. All unsteady simulations for the airfoil parametric analysis were performed using 100 time steps per disturbance forcing period, corresponding to a time step of $5x10^{-3}$ s. Local convergence was achieved at each time step, with as many as 35 sub-iterations per time step. Global convergence for all unsteady simulations was based on lift periodicity; convergence was achieved when lift periodicity reached less than 0.1% variability between forcing periods. Figure 3-9 illustrates lift-convergence history for the NACA 0012 airfoil; this history is representative of all simulations conducted in the present research.

Table 3.5 FLUENT Configuration for Numerical Simulations.

Parameter	***Value***
Fluent Solver	Coupled-Implicit
Discretization Scheme	Second-Order (Momentum and Viscosity)
Material Properties	Standard Day Air as an Ideal-Gas
Operating Pressure	0 Pa
Viscosity Model	Standard k-ε Turbulence Model
Inlet Boundary Condition	Pressure Inlet
Outlet Boundary Condition	Pressure Outlet
Periodic Boundary Condition	Periodic

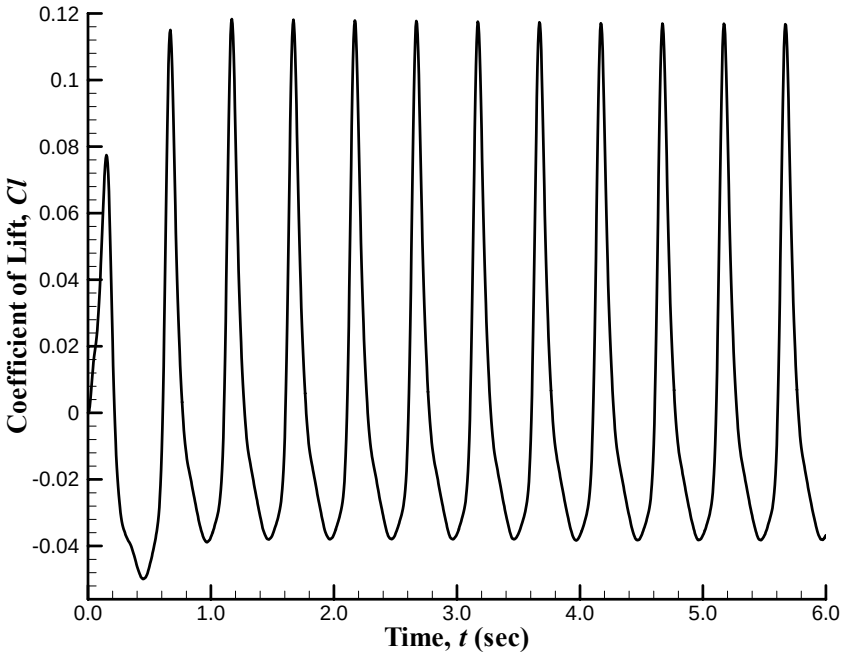

Figure 3-9 Lift Coefficient Time History Showing Convergence: NACA 0012 Profile.

3.6.1 Reference Values

During calculations, FLUENT employs non-dimensionalized variables. All variables are non-dimensionalized using the reference values listed in Table 3.6.

Table 3.6 FLUENT Reference Values

Parameter	***Value***
Reference Density	1.225 kg/m^3
Reference Length	1 m
Reference Pressure	101325 Pa
Reference Temperature	300 K
Reference Velocity	10.0001 m/s
Reference Viscosity	1.7894e-5 kg/m-s
Ratio of Specific Heats	1.40
Operating Pressure	0 Pa

3.6.2 Boundary Conditions

Pressure-inlet and pressure-outlet boundary conditions were employed for the computational inlet and outlet, respectively, with inlet pressure and temperature boundary conditions being set to standard-day atmospheric values for the steady-state simulation. However, for the unsteady simulations a UDF was employed at the pressure-inlet boundary, mimicking the convecting wake from a rotating rotor blade. Standard wall boundary conditions were used for airfoil/stator-vane suction and pressure surfaces. A detailed description of the UDF is presented in Section 3.4. Time-averaged freestream velocity was set to 10 m/s for all NACA airfoil-cascade simulations, while time-averaged freestream velocity for the stator-vane cascade simulations was set to 200 m/s. Table 3.7

summarizes the inlet and outlet boundary conditions employed for all FLUENT simulations performed in this research.

Table 3.7 FLUENT Boundary Conditions

Parameter	***Value***
Inlet Boundary Conditions	
Total Temperature	300 K
Direction Specification	Normal to Boundary
Turbulence Intensity (%)	1
Turbulence Viscosity Ratio	1
Outlet Boundary Conditions	
Backflow Total Temperature	300 K
Turbulence Intensity (%)	1
Turbulence Viscosity Ratio	1

3.7 Grid Independence

Gird independence was examined by obtaining NACA 0012 steady-state solutions for higher density (fine) mesh, as compared to the nominal mesh of Figure 3-5. The fine mesh contained 42018 elements, where 37618 were triangular mesh elements and 4400 were quadrahedral mesh elements. Pressure coefficient results from the NACA 0012 airfoil upper and lower surfaces were compared for each mesh.

Figure 3-10 shows steady-state pressure coefficient data along the NACA 0012 airfoil upper and lower surfaces for the nominal and fine meshes. As seen in the figure, the obtained pressure data compare favorably well, showing minimal discrepancies. As such, the nominal grid is deemed to be of sufficient density for the present investigation.

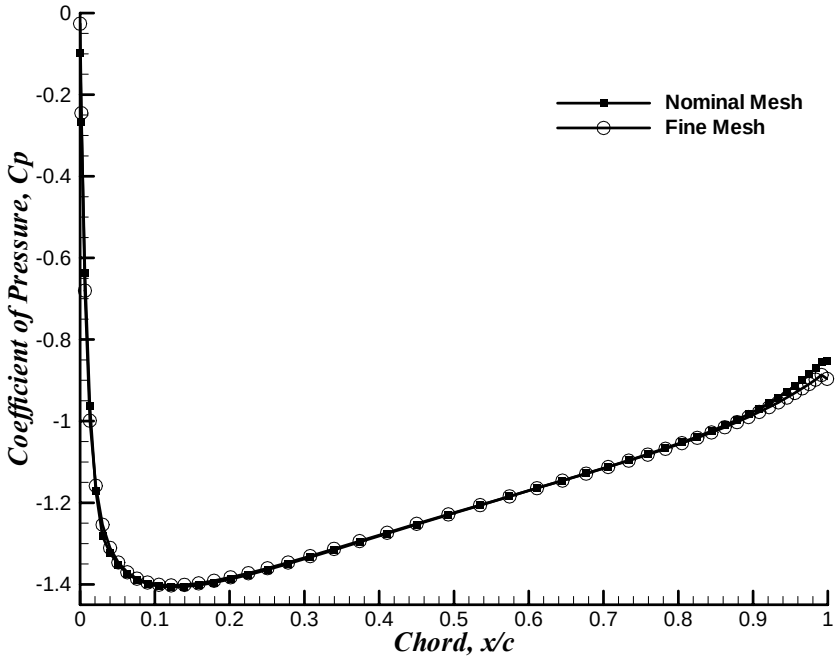

Figure 3-10 Steady-State Pressure Coefficient Data: NACA 0012.

Similar grid independence studies were performed for the stator-vane cascade analysis. In this case, the high density (fine) mesh contained 38000 quadrahedral elements as compared to the 28000 quadrahedral elements contained by the nominal mesh shown in Figure 3-8.

Figure 3-11 shows steady-state pressure coefficient data along the stator-vane upper and lower surfaces for the nominal and fine meshes. Here again, the pressure data obtained compare favorably showing negligible discrepancies. In particular, along the stator-vane upper surface small differences in pressure coefficient values are seen near the mid-chord region. However, near the leading and trailing edges the pressure data for the two meshes match perfectly well. Given the agreement of data and the additional CPU time required per computation by the fine mesh as compared to the nominal mesh, the nominal mesh is deemed to be of sufficient density for the present investigation.

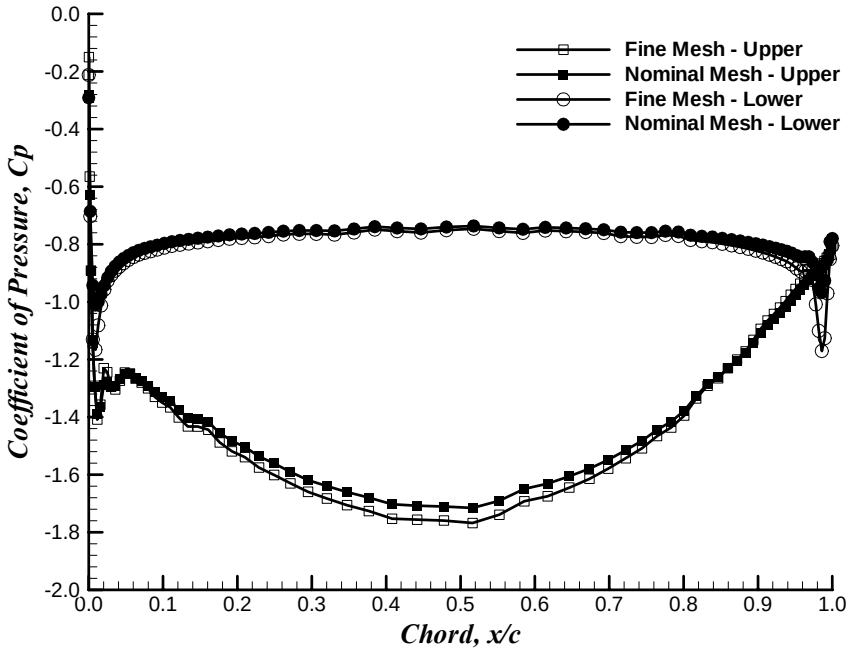

Figure 3-11 Pressure Coefficient Data: Stator-Vane.

4 Chapter 4

SOLUTION VALIDATION

This chapter describes the time-averaged static-pressure results for the baseline NACA 0012 airfoil case. The time-averaged flowfield represents an important aspect of the overall unsteady-forcing simulations for two reasons. First, unsteady results develop by subtracting time-averaged parameters from the instantaneous solution at each time step; thus, giving parameter perturbations about the time-averaged field. Second, the time-averaged flowfield facilitates examination to determine the accuracy and applicability of the FLUENT simulation results. Note that the time-averaged computational results described herein are primarily compared with experimental data from Abbott and Von Doenhoff [1959].

4.1 TIME-AVERAGED METHODOLOGY

Time-averaged parameter distributions for each simulation are computed by summing flow parameters (i.e., pressure, velocity, etc.) at each lifting surface grid location over 50 time steps (one aerodynamic forcing period), respectively. Resulting summations are then divided by 50, giving a time-averaged value for each solution parameter at each grid point.

4.2 BASELINE AIRFOIL TIME-AVERAGED STATIC-PRESSURE DISTRIBUTIONS

A time-averaged total-pressure contour plot for the NACA 0012 airfoil is presented in Figure 4-1, with attached numerical values indicating respective pressure contour levels.

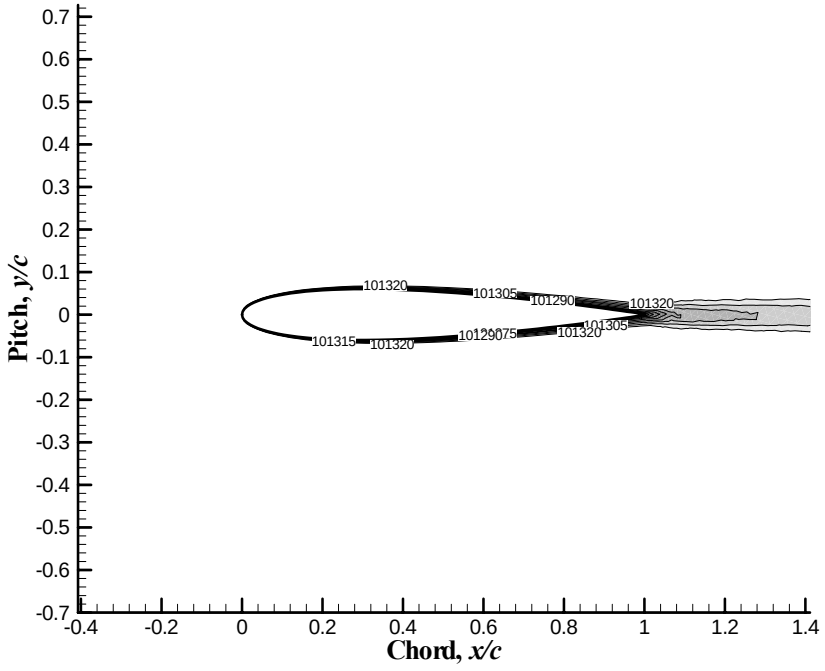

Figure 4-1 Time-Averaged Total-Pressure Contours (Pa): NACA 0012 Lifting Surface

As expected for this lifting-surface profile, the contours illustrate good qualitative characteristics of the simulated flowfield, showing a well-behaved symmetric total pressure distribution about the profile and in the lifting-surface wake. The flowfield on the airfoil surface shown in Figure 4-1 shows no indication of large-scale separation, exhibiting smooth attached flow. Thus, the time-averaged flow about the baseline lifting-surface is argued to be attached and producing a similar wake to that which would be expected.

Figure 4-2 exhibits the total-pressure wake profile of the NACA 0012 lifting surface. Pitchwise total pressure wake profiles at x/c = 0.005 and 0.01 downstream of the airfoil are exhibited. As discussed in Section 3.4 wake depth is defined as the maximum total pressure deficit, while wake width represents the maximum pitchwise effect of the total pressure deficit. Symmetric wake profiles are observed at both x/c locations downstream of the airfoil. Thus, confirming the inferences made earlier from Figure 4-1.

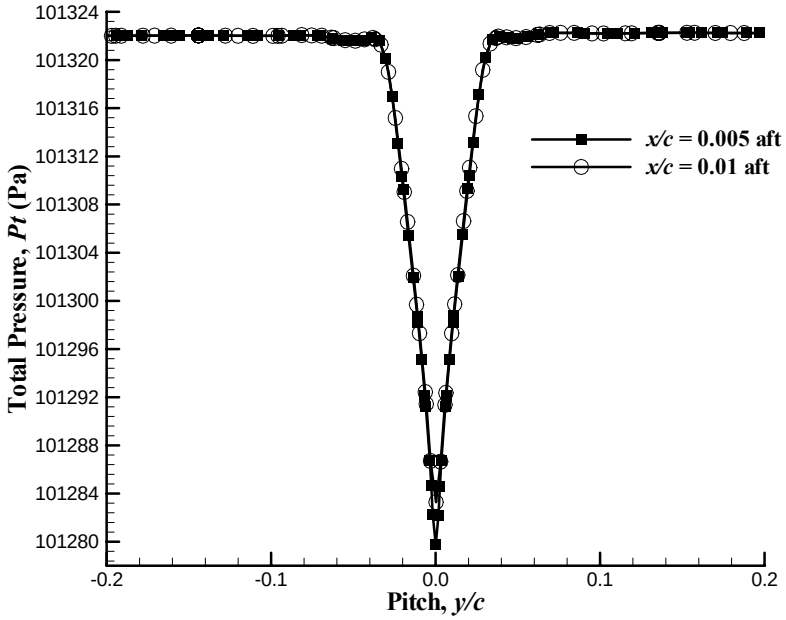

Figure 4-2 NACA 0012 Lifting Surface Wake Profile.

Figure 4-3 displays time-averaged static pressures computed along the NACA 0012 lifting surface chord. Pressure distributions along the suction and pressure surfaces are individually displayed. As expected, the symmetric NACA 0012 profile produces equivalent time-averaged static-pressure distributions on the suction (upper) and pressure (lower) surfaces. Thus, no time-averaged aerodynamic loading exists on the airfoil.

Static-pressure distributions predicted by FLUENT along the NACA 0012 profile are also compared with available experimental data [Abbott and Von Doenhoff, 1959], as

shown in Figure 4-3. The computational data compared favorably with the experimental data, except near the leading and trailing edge regions where slight discrepancies were found. In particular, the minimum pressure near the leading edge was underestimated, while a slightly lower pressure was predicted in the trailing-edge region. Given the reasonable agreement of the time-averaged data, the simulations presented herein correctly predict the time-averaged flowfield about the examined lifting surface.

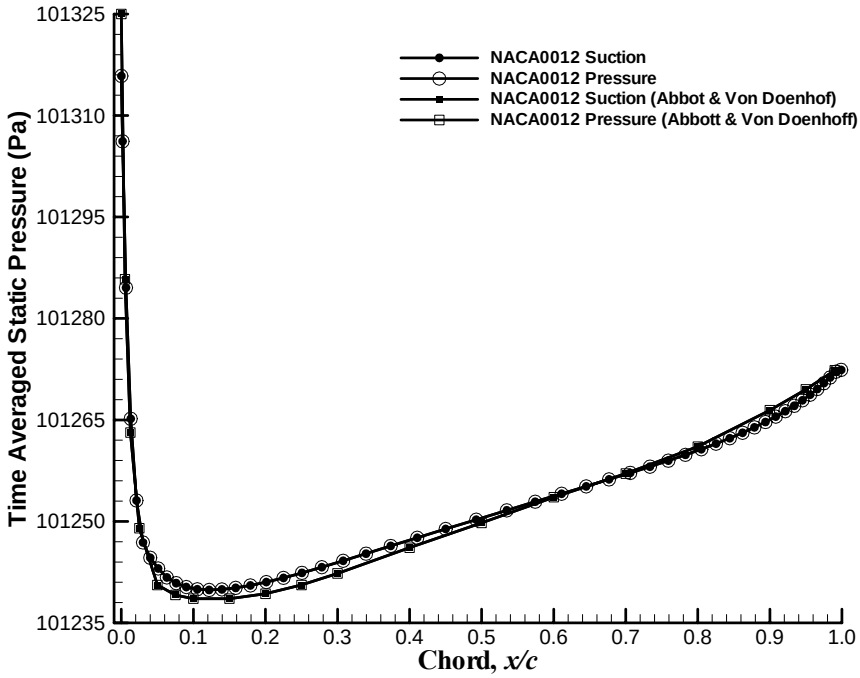

Figure 4-3 Time-Averaged Static Pressure : NACA 0012.

Figure 4-4 illustrates time-averaged static-pressure distributions computed for flow over the NACA 0012 airfoil at 0°, 5° and 10° angles of attack relative to the freestream. The non-equivalent surface-pressure distributions on the suction and pressure surfaces indicate aerodynamic loading caused by the non-zero angle of attack of the flow. The static pressure at the suction-surface leading edge decreases as angle of attack increases, while the static pressure at the pressure-surface leading edge increases. As

angle of attack increases, the difference in the pressure between the suction and pressure surfaces increases, producing higher aerodynamic loading.

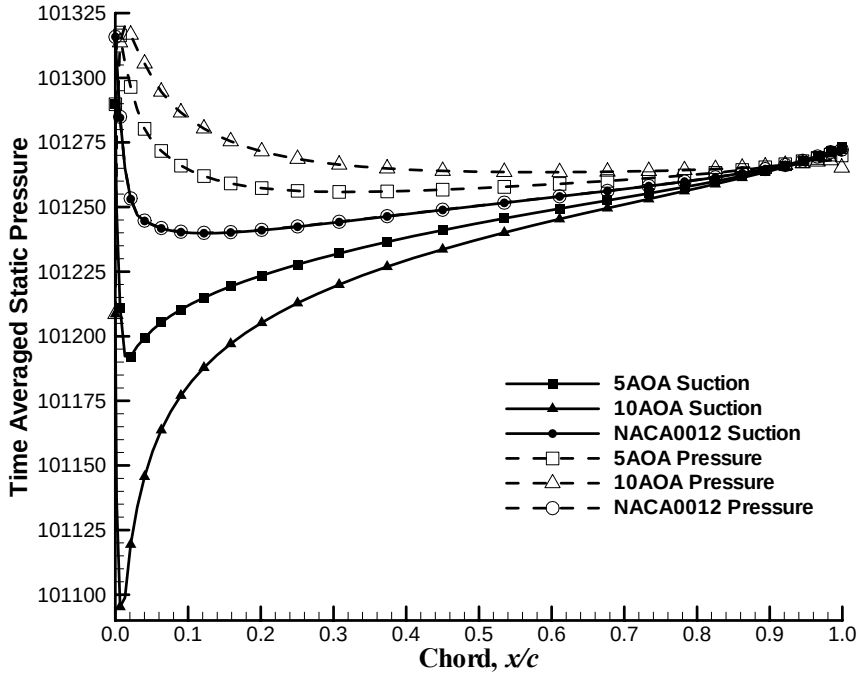

Figure 4-4 Time-Averaged Static Pressure : 0°, 5° and 10° Angle of Attack

Table 4.1 compares the computed lift coefficient values for the NACA 0012 airfoil at 0°, 5° and 10° angles of attack (relative to the freestream) with available experimental values from Abbott and Von Doenhoff [1959]. Note that the experimental values were measured at $Re = 6\text{x}10^6$, while Reynolds number for the current simulations was calculated to be $Re = 5.88\text{x}10^6$. As such, the discrepancy in the lift coefficient value is attributed to the lower *Re* used for the current investigation.

Table 4.1 Coefficient of Lift: 5° and 10° Angle of Attack.

Angle of Attack	*Computed Value*	*Experimental Value*
5°	0.54	0.59
10°	0.82	0.87

4.3 TIME-AVERAGED STATIC-PRESSURE DISTRIBUTIONS (THICKNESS INFLUENCE)

As described later in this thesis, the influence of lifting-surface thickness on time-accurate surface-pressure phase is examined via simulation of three NACA profiles of 10, 12, 15 and 20% thickness (based on chord). Figure 4-5 illustrates the corresponding time-averaged static-pressure distributions from these simulations, collected over one aerodynamic forcing period. The data in Figure 4-5 show good agreement between suction and pressure surfaces for each thickness, as anticipated for symmetric profiles. The equivalent surface-pressure distributions on both suction and pressure surfaces for each thickness case are indicative of no time-averaged aerodynamic loading. Each profile has distinct time-averaged pressure gradients along the chord, with higher thickness values resulting in more severe chordwise gradients.

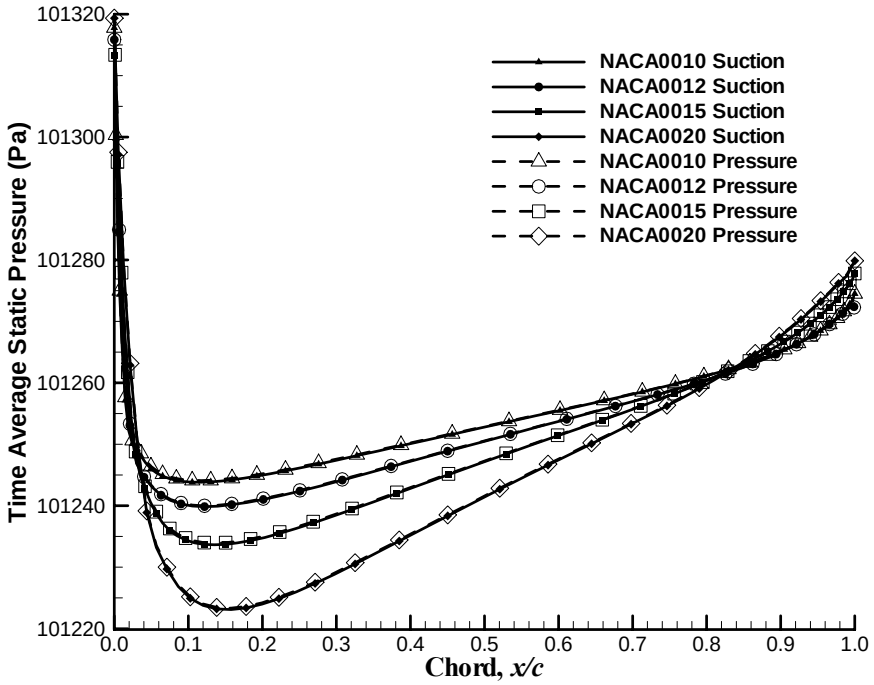

Figure 4-5 Time-Averaged Static-Pressure for Various Lifting-Surface Thicknesses.

The static-pressure distributions predicted by FLUENT for the 10 and 15% thickness profiles were compared with available experimental data from Abbott and Von Doenhoff [1959] as shown in Figure 4-6. Here again, as in the NACA 0012 case, the computational data compared favorably with the experimental data, except in the leading and trailing edge regions where slight discrepancies are observed. In particular, the minimum static-pressure near the leading edge is underestimated and a slightly lower static-pressure is predicted in the trailing edge region.

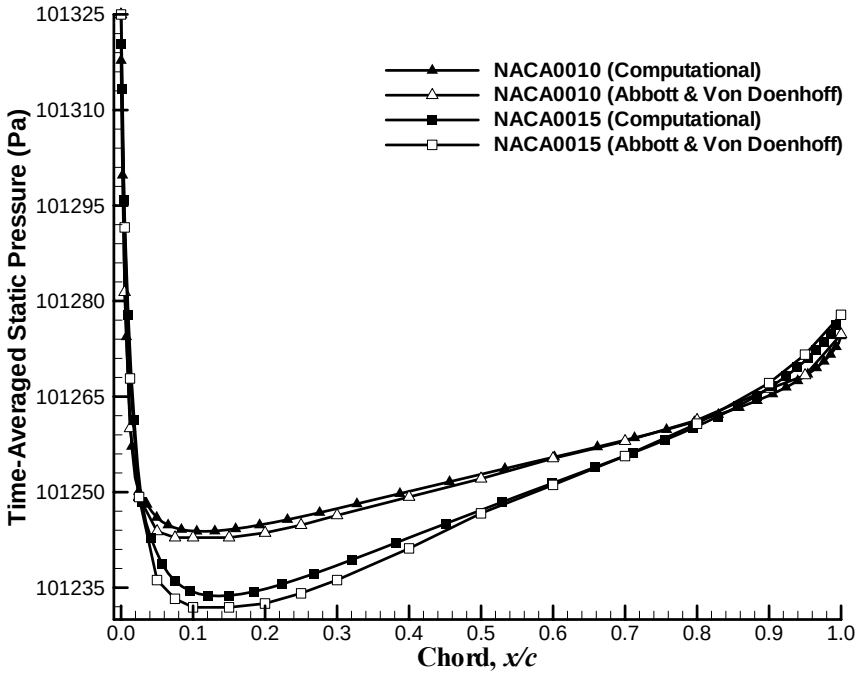

Figure 4-6 Time averaged Static Pressure Comparison with Experimental data.

4.4 TIME-AVERAGED STATIC-PRESSURE DISTRIBUTIONS (CAMBER INFLUENCE)

In addition to the lifting-surface cases, three cambered lifting-surface geometries were also considered, including 0, 2, and 6% camber (relative to chord). Figure 4-7 shows time-averaged static-pressure distributions along the suction and pressure surfaces

of each cambered profile. Note from Figure 4-7 that while each profile exhibits a unique chordwise surface-pressure gradient, as for various profile thicknesses, the cambered profiles also exhibit time-averaged aerodynamic loading. This is exhibited by the non-equivalent surface pressure distributions on the suction and pressure surfaces in Figure 4-7. Differential pressure across the lifting-surface increases as the percentage of camber relative to chord increases.

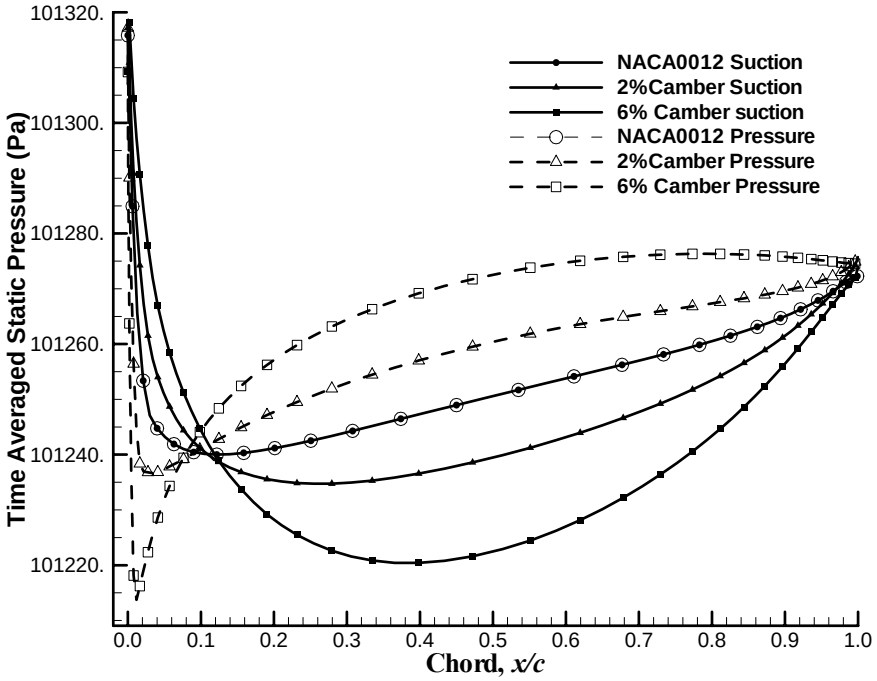

Figure 4-7 Time-Averaged Static-Pressure Distribution for Various Lifting-Surface Cambers

Table 4.2 compares the computed lift coefficient values for 2, and 6% cambered (relative to chord) airfoils with available experimental values from Abbott and Von Doenhoff [1959]. Here again, as was seen earlier for the AOA case, the computed lift coefficient values were slightly lower than the experimental values.

Table 4.2 Coefficient of Lift: Various Lifting-Surface Cambers.

Camber)	*Computed Value*	*Experimental Value*
2 %	0.21	0.25
6 %	0.74	0.78

4.5 COMPARISON OF TIME-ACCURATE BASELINE LIFT DEPENDENCY TO SEAR'S RESULTS

Figure 4-8 presents the first-harmonic (i.e., fundamental frequency) lift time series obtained from FLUENT for the baseline NACA 0012 airfoil, as well as known lift prediction for airfoils experiencing a sinusoidal transverse gust, as described by Sears [1938]. As can be seen in Figure 4-7, the computed lift compares perfectly well with the Sears predicted lift series. Note that, Sears unsteady aerodynamic forcing was modeled as a perfect sine-wave transverse gust as opposed to the rotor-wake model (transverse and chordwise varying velocity components) used for unsteady aerodynamic forcing in the present analysis. Given this agreement of the lift time series data, the unsteady results obtained from FLUENT are further validated.

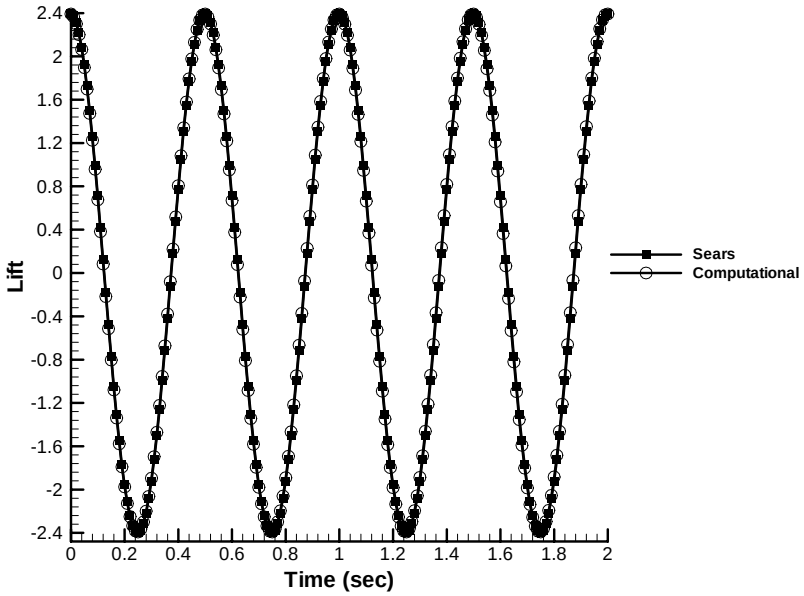

Figure 4-8 Lift-Time series Comparison with Sears results.

4.6 TIME-AVERAGED RESULTS SUMMARY

Time-averaged results obtained from FLUENT for the baseline NACA 0012 airfoil showed well-behaved characteristics. Total pressure contours around the airfoil exhibited smooth attached flow with no signs of large-scale separation and a symmetric wake profile. Pitchwise wake profiles developed downstream of the NACA 0012 lifting surface at $x/c = 0.005$ and $x/c = 0.01$ exhibited symmetry as well, further ascertaining this inference. Time-averaged static pressure distributions along the upper and lower surface of the NACA 0012 airfoil were perfectly symmetric, as expected for this profile. Thus, indicating no aerodynamic loading exists on the airfoil. Comparison of the time-averaged pressures with experimentally obtained values from Abbott and Von Doenhoff [1959] exhibited reasonable agreement with very slight discrepancies observed near the leading edge and trailing edge regions. Given this agreement of time-averaged data, the simulations presented correctly predict the time-averaged flowfield about the examined lifting surface.

Time-averaged pressure distributions obtained for various mean flow angles of attack (AOA), various thickness profiles and various camber profiles exhibited characteristics similar to that, which would be expected for the respective profiles. Non-equivalent time-averaged pressure distributions were exhibited at various mean flow angles of attack and by the various camber profiles, indicating aerodynamic loading on these profiles. Differential pressure (aerodynamic loading) was observed to increase as both AOA and percentage of camber relative to chord increased. Conversely, the various thickness profiles exhibited equivalent time-averaged pressure distributions along the upper and lower surfaces indicative of no time-averaged aerodynamic loading. Each thickness profile exhibits distinct time-averaged pressure gradients along the chord, with higher thickness values resulting in more severe chordwise gradients.

Computationally obtained time-averaged results for the parametric analyses were compared with those obtained experimentally by Abbott and Von Doenhoff [1959]. The computationally obtained time-averaged results compared favorably with the experimental data. Thereby, validating the steady state solution obtained from FLUENT for the current simulations. To validate the unsteady solution, first-harmonic lift time-series obtained from FLUENT for the NACA 0012 airfoil was compared with the Sears predicted lift series. The time-series matched perfectly well, even though Sears unsteady aerodynamic forcing was modeled as a perfect sine-wave transverse gust as opposed to the rotor-wake model (transverse and chordwise varying velocity components) used for unsteady aerodynamic forcing in the present analysis. Thus, the unsteady solution is validated.

5 Chapter 5

RESULTS FOR NACA 0012 BASELINE CONFIGURATION

This chapter describes the aerodynamic forcing function, as well as resulting airfoil forced response, for the baseline NACA 0012 airfoil simulations. Airfoil results are reported in terms of chordwise unsteady surface-pressure distributions, spectral content, and phase. Examination of the surface-pressure phase data reveals characteristics indicative of multiple disturbance interactions, similar to that discussed by Fabian and Jumper [1996]. An analytical model is developed to reproduce these observed interaction characteristics, and compared to simulation results.

5.1 DATA REDUCTION METHODOLOGY

Unsteady pressure results were obtained by removing the time-averaged pressure from the instantaneous pressure via

$$P' = P - \overline{P}$$

Unsteady pressure data were further reduced into elements of amplitude, frequency, and phase for first, second and third harmonics (i.e. one, two and three times the fundamental frequency) components. This was accomplished via Fast-Fourier Transform (FFT) techniques.

5.2 AIRFOIL FORCING-FUNCTION TIME DEPENDENCY

Figure 5-1 through Figure 5-4 exhibit total-pressure contours of the airfoil aerodynamic forcing function, or wake, moving downstream over the NACA 0012 airfoil. The plots illustrate total-pressure contours at four time instances during a single aerodynamic forcing period, T; illustrated times correlate to $t = 0$, $T/4$, $T/2$, and $3T/4$. The total-pressure disturbance is periodic and repeats with every forcing period. As the total-pressure disturbance translates, it directly impacts the airfoil leading edge. At the airfoil leading edge, the disturbance splits and propagates downstream along both airfoil lower and upper surfaces. This disturbance splitting process is most evident from $t = T/4$ to $t = T/2$. At impact on the airfoil upper surface, the disturbance accelerates (as compared to lower surface) before propagating downstream along the airfoil, decaying in strength during the process. On the airfoil lower surface, disturbance impact is much less prominent; disturbance chordwise propagation is delayed (i.e. it remains further upstream) relative to the upper-surface disturbance.

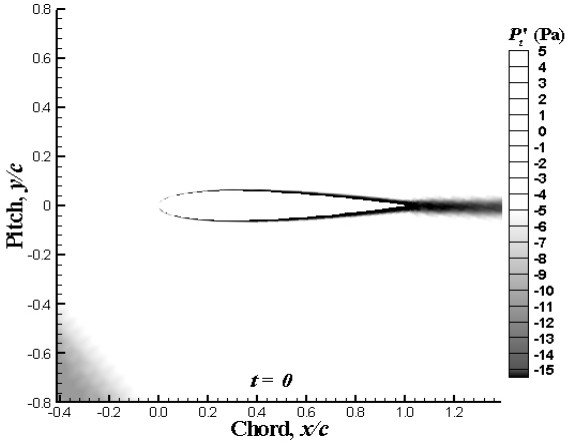

Figure 5-1 Forcing Function Total-Pressure Contours, $t = 0$.

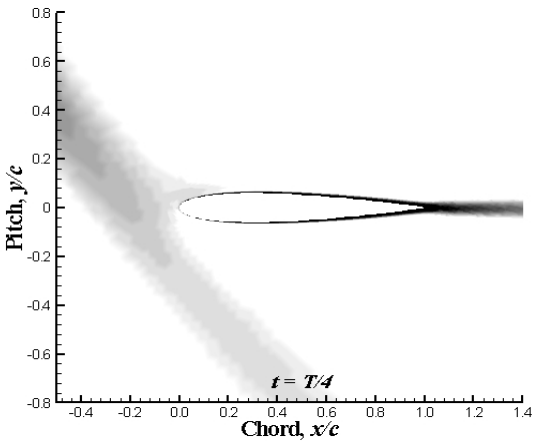

Figure 5-2 Forcing Function Total-Pressure Contours, $t = T/4$.

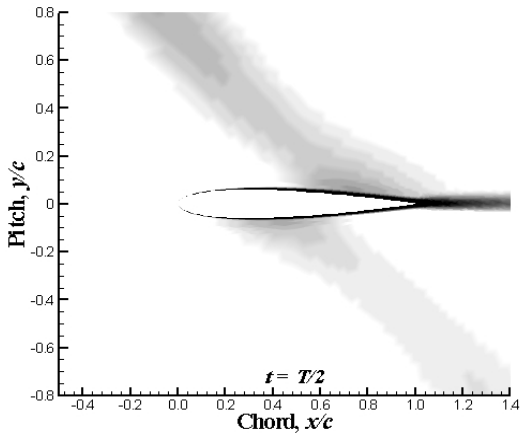

Figure 5-3 Forcing Function Total-Pressure Contours, t = T/2.

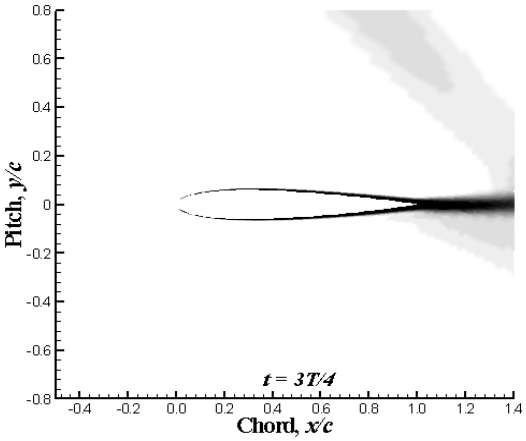

Figure 5-4 Forcing Function Total-Pressure Contours, t = 3T/4.

Figure 5-5 displays total-pressure time series relating the airfoil forcing-function at five equally spaced *x/c* locations (*x/c* = -0.2, -0.4, -0.6, -0.8, and –1.0) forward of the airfoil leading edge. Note that the time series have been arbitrarily shifted vertically by four units at each sequential *x/c* location, to provide better viewing. As expected, Figure 5-5 indicates periodic total-pressure variations corresponding to the aerodynamic-forcing frequency. Disturbance amplitude changes as the forcing wake travels downstream, indicating expected wake decay with convective distance. A monotonic phase shift is also observed between the time series, indicating constant-speed disturbance propagation downstream, or convection. Note that while the pressure fluctuations in Figure 5-5 are periodic, they are not purely sinusoidal, indicating the existence of forcing-function harmonic content.

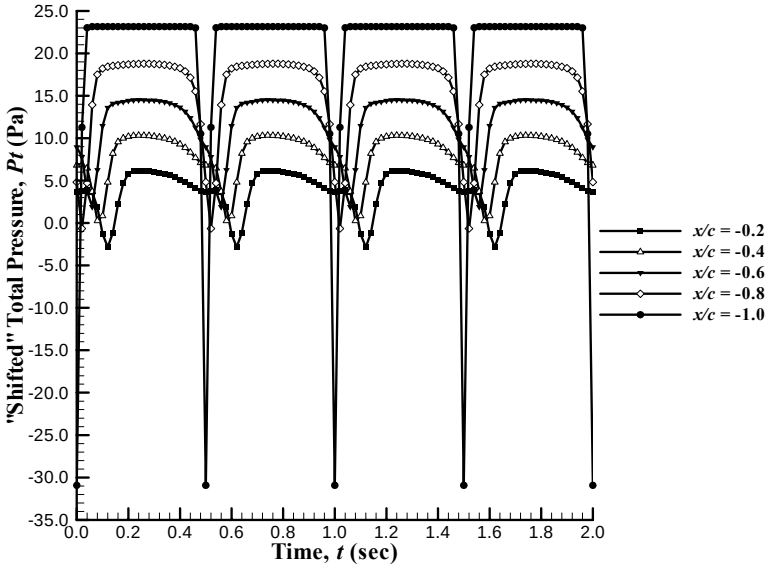

Figure 5-5 Total-Pressure Time Series Forward of Airfoil.

Figure 5-6 displays forcing-function static-pressure time series at five equally spaced *x/c* locations (20, 40, 60, 80 and 100%) forward of the airfoil leading edge. Similar amplitude trends (decreasing downstream) and periodicity are seen as in the total-pressure time series; however, no phase shift is observed between the series. Here again, the static pressure fluctuations are periodic but not purely sinusoidal, indicating the existence of harmonic content.

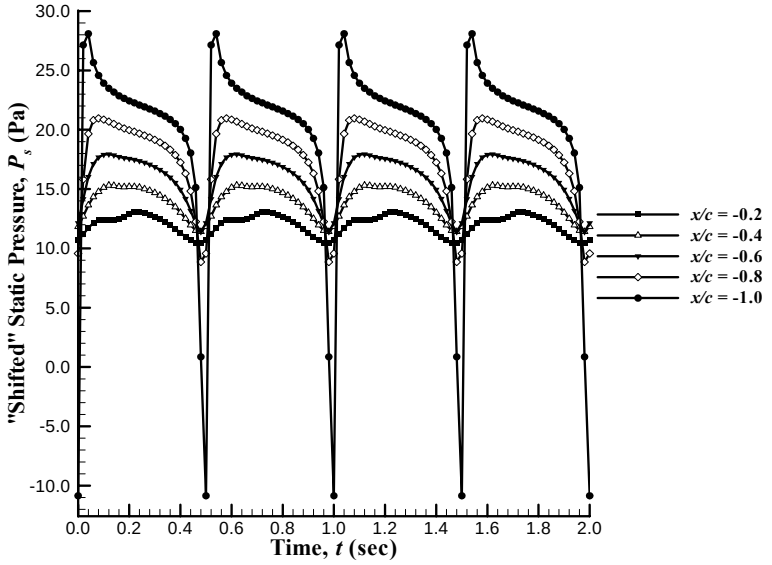

Figure 5-6 Static-Pressure Time series.

5.3 AIRFOIL FORCING-FUNCTION SPECTRAL CONTENT

Figure 5-7 and Figure 5-8 depict spectral content corresponding to the forcing-function total-pressure and static-pressure time series in Figure 5-5 and Figure 5-6, respectively. Note the *x*-axis in the spectral plots is reversed in order to indicate flow direction from the simulation inlet to airfoil leading edge. Significant harmonic frequencies reaching three times the primary aerodynamic-forcing frequency are observed in both figures. Both total and static pressures exhibit increased harmonic content near the inlet, with total-pressure showing greater amplitude. In each case, harmonic content decays as the wake travels downstream towards the airfoil leading edge. Such harmonic amplitude decay is expected, as wake mixing with convective distance inherently causes rapid spectral content loss.

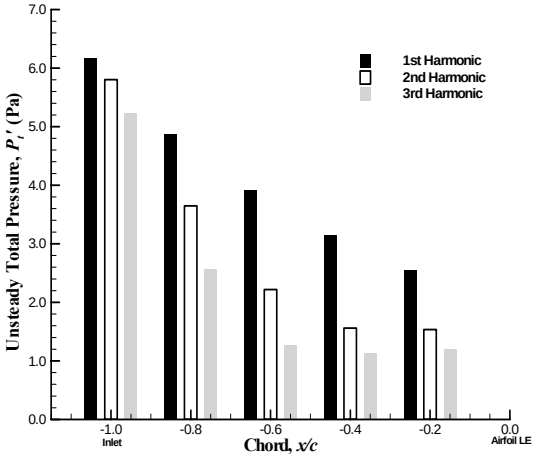

Figure 5-7 Forcing Function Total-Pressure Spectral Content.

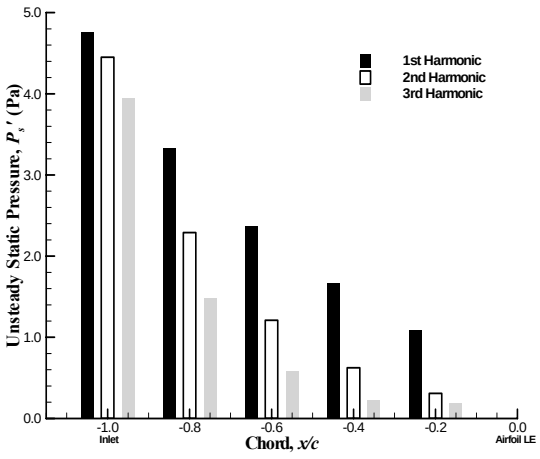

Figure 5-8 Forcing Function Static-Pressure Spectral Content.

5.4 AIRFOIL FORCING-FUNCTION PHASE DEPENDENCY

Figure 5-9 shows relative phase data for the first-harmonic static pressure at five equally spaced *x/c* locations (*x/c* = -0.2, -0.4, -0.6, -0.8, and –1.0) forward of the airfoil leading edge. Note the *x*-axis direction on the phase plot is reversed corresponding to

disturbance propagation direction. The first-harmonic phase data in Figure 5-9 shows consistent downstream disturbance propagation (i.e., convection) towards the airfoil leading edge, as indicated by the constant negative slope of the phase line. However, unsteady disturbance propagation changes dramatically as the airfoil leading edge is approached, as indicated by the positive phase slope beginning *x/c* = -0.2 forward of the leading edge. This change in phase slope correlates to rapid disturbance deformation near the leading edge, as can be observed in Figure 5-2.

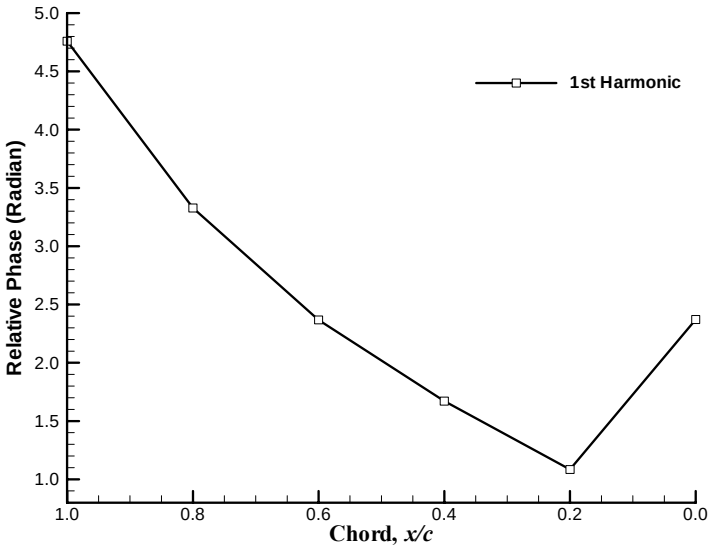

Figure 5-9 Airfoil Forcing Function 1st Harmonic Phase.

Relative-phase data at the second and third-harmonic frequencies are shown in Figure 5-10, for the forcing-function static-pressure data at five equally spaced *x/c* locations forward of the airfoil leading edge. It is observed that the second harmonic has a positively increasing phase slope; the increase in slope is very small until *x/c* = -0.4, after which it increases significantly. In comparison, the third harmonic phase slope is approximately zero, indicating very little propagation of the third-harmonic static pressure component. It is interesting to note the relative phase differences between the

static pressure first, second and third harmonics. Each harmonic component exhibits a different phase behavior, but collectively they combine to produce a waveform showing almost no propagation characteristics, as noted in Figure 5-6.

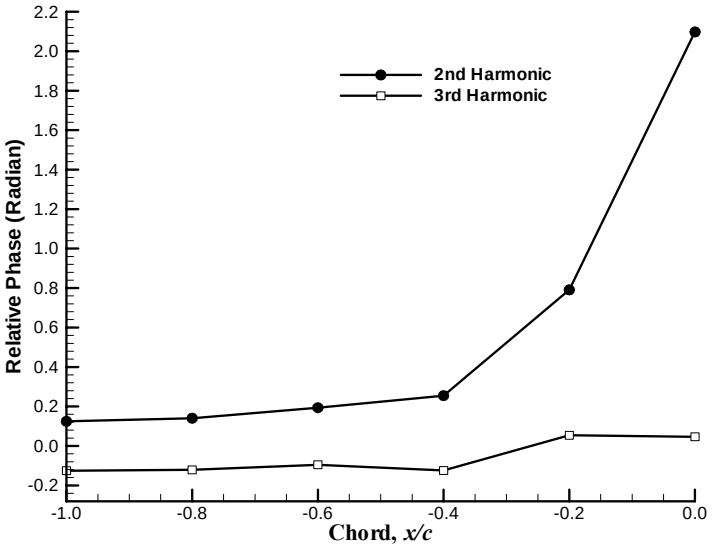

Figure 5-10 Airfoil Forcing Function Higher Harmonic Phase.

5.5 AIRFOIL SURFACE-PRESSURE TIME DEPENDENCY

Figure 5-11 through Figure 5-14 show contours of static pressure for the NACA 0012 airfoil at four time instances during a single aerodynamic forcing period, T; illustrated times correlate to $t = 0$, $T/4$, $T/2$, and $3T/4$.

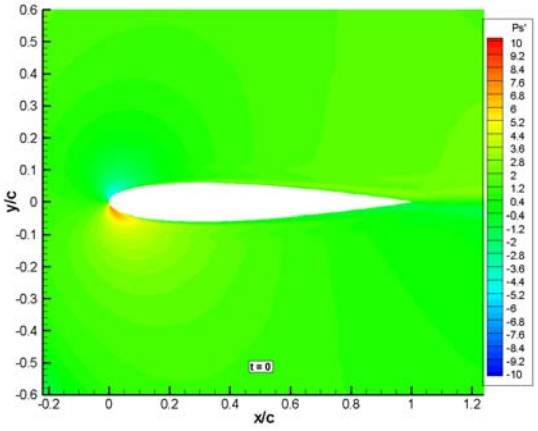

Figure 5-11 Airfoil Static-Pressure Contours, $t = 0$.

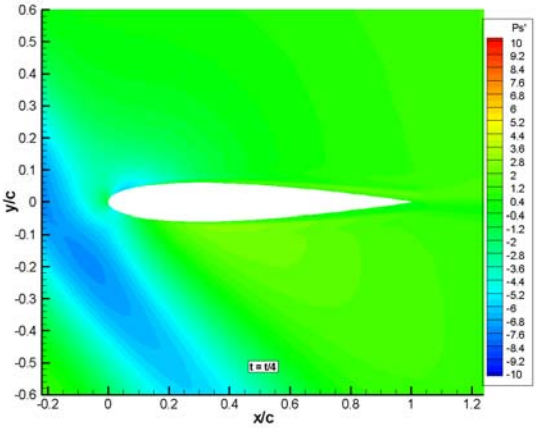

Figure 5-12 Airfoil Static-Pressure Contours, $t = T/4$.

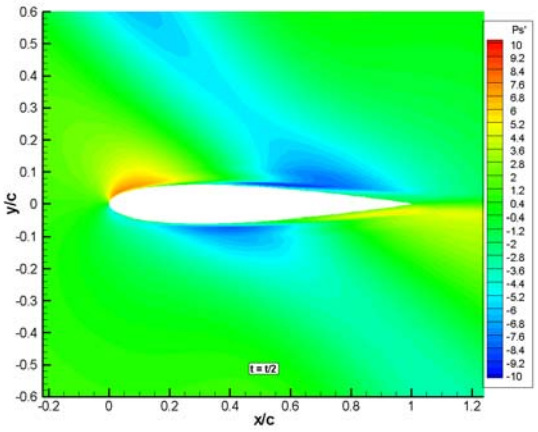

Figure 5-13 Airfoil Static-Pressure Contours, $t = T/2$.

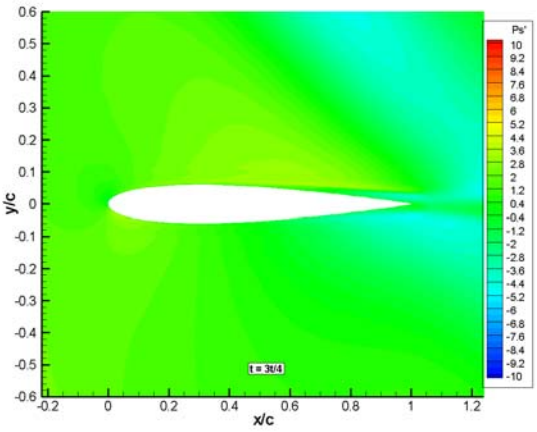

Figure 5-14 Airfoil Static-Pressure Contours, $t = 3T/4$.

As desired in construction of the forcing function, static-pressure disturbances repeat in time, mimicking the effect of a wake convecting from an upstream rotor in a turbomachine compressor. At the airfoil leading edge, the wake-induced pressure disturbances split and propagate downstream along both airfoil lower and upper surfaces. This disturbance splitting process is most evident from $t = T/4$ to $t = T/2$. At impact on the airfoil upper surface, the pressure waves also reflect back into the oncoming disturbance field. The impacted wave and its reflection travel together downstream along the airfoil, decaying in strength during the process. On the airfoil lower surface, pressure wave impact and reflection is much less prominent. Lower-surface chordwise disturbance propagation is delayed (i.e. further downstream) relative to the upper surface, as illustrated from $t = T/4$ to $t = T/2$.

Figure 5-15 shows airfoil surface-pressure time series at various chordwise locations along the airfoil upper surface. Note, the static-pressure series have been arbitrarily shifted vertically by two units at each sequential x/c location, to provide better viewing. As expected, these figures indicate periodic static-pressure variations corresponding to the aerodynamic-forcing frequency. While the pressure fluctuations are

periodic, they are not purely sinusoidal, indicating the existence of harmonic content. Higher amplitude unsteady pressure fluctuations exist near the airfoil leading edge, decaying rapidly downstream. Figure 5.15 also indicates almost no phase delay between time series at each *x/c* locations, a curious finding given the convective nature of the forcing function. This finding corresponds to the freestream static-pressure time series of Figure 5-6, and will be examined further in following sections.

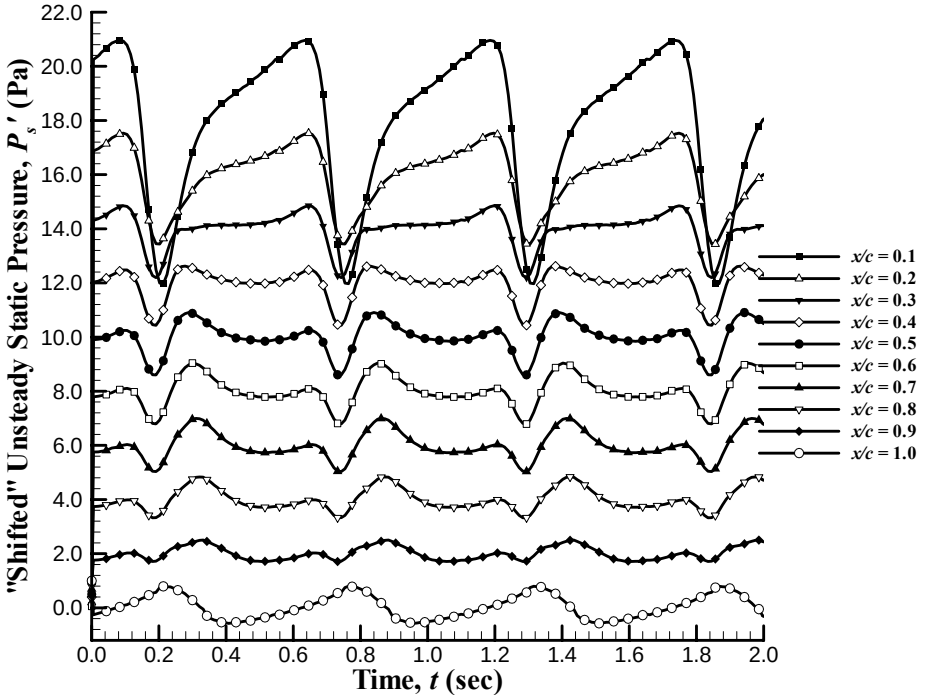

Figure 5-15 NACA 0012 Upper Surface Unsteady Static-Pressure Time series.

Figure 5-16 shows airfoil surface-pressure time series at various chordwise locations along the airfoil lower surface. Similar to the upper surface, the lower surface exhibits periodic time-series behavior corresponding to the aerodynamic-forcing frequency, unsteady leading-edge pressure amplification, and very little phase shift between chordwise locations. The lower-surface pressure fluctuations also display an almost reversed behavior as compared to the upper-surface, showing pressure increases at

the same instances as the upper surface experiences a pressure decrease. However, overall time-series amplitudes are greater for the lower surface as compared to the upper surface.

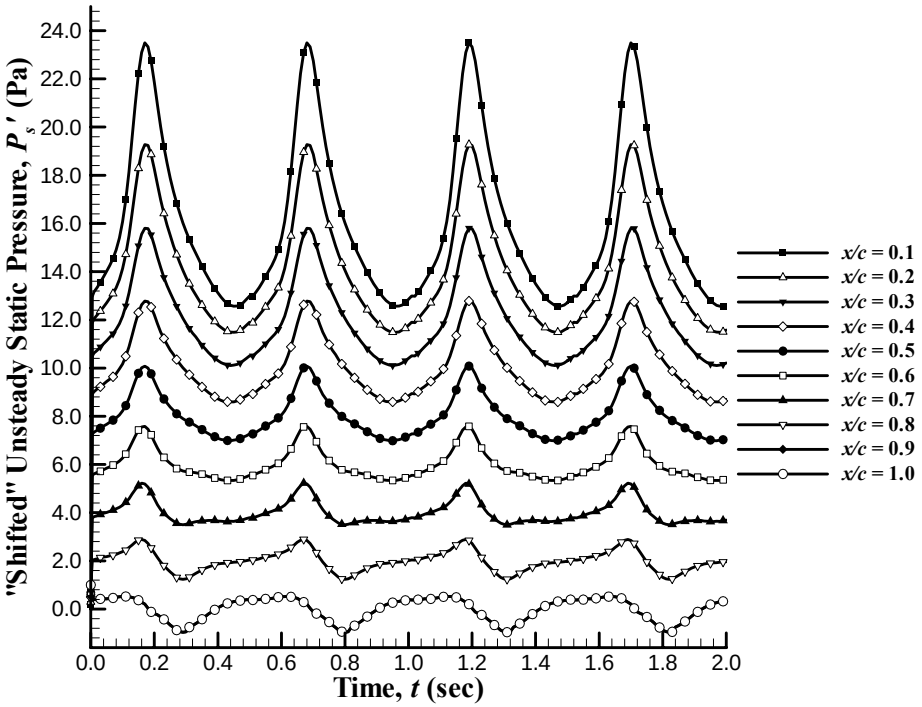

Figure 5-16 NACA 0012 Lower Surface Unsteady Static-Pressure Time series.

Differential surface-pressure time series data at various chordwise locations along the airfoil are provided in Appendix D. Differential surface pressure represents upper-surface minus lower-surface unsteady pressure, as presented in Eq. (5.1).

$$\Delta p' = p'_u - p'_l \qquad \textbf{5.1}$$

Here again, periodic time-series behavior corresponding to the aerodynamic-forcing frequency is obtained. The differential pressure is highest in amplitude at the leading edge, decays in strength downstream along the airfoil, and shows almost no phase shift between chordwise locations. Differential-pressure fluctuations are periodic in nature, but not purely sinusoidal, indicating the existence of harmonic content.

5.6 AIRFOIL SURFACE-PRESSURE SPECTRAL CONTENT

Figure 5-17 depicts spectral content related to the airfoil upper-surface pressure time series shown in Figure 5-15. Relevant surface-pressure harmonic frequencies reaching four times the aerodynamic-forcing frequency are observed. The airfoil upper surface exhibits increased higher-order pressure harmonics near the airfoil leading edge, generally decaying downstream along the upper surface. Specifically, the first-harmonic amplitude decays until x/c = 0.4, then increases toward the airfoil trailing edge. The second harmonic amplitude also shows a decaying trend downstream, but between x/c = 0.4 and x/c = 0.6 it exhibits higher amplitude than the first harmonic. The third and fourth harmonic amplitudes generally show a decaying trend with chordwise distance, almost vanishing near the airfoil trailing edge.

Note that harmonic content can be related to the "sine-like" behavior of a time series. For example, it would be expected that a wake time-series profile, such as in Figure 5-5, would exhibit significant harmonic content, while a pure sine wave would not. Thus, the relative change in harmonic content with chord position, as seen in Figure 5-17, can be directly attributed to disturbance deformation and interaction over the airfoil. Near the leading edge the disturbance is "wake-like" while at the trailing edge it is much more "sine-like". This statement is supported by Figure 5-15.

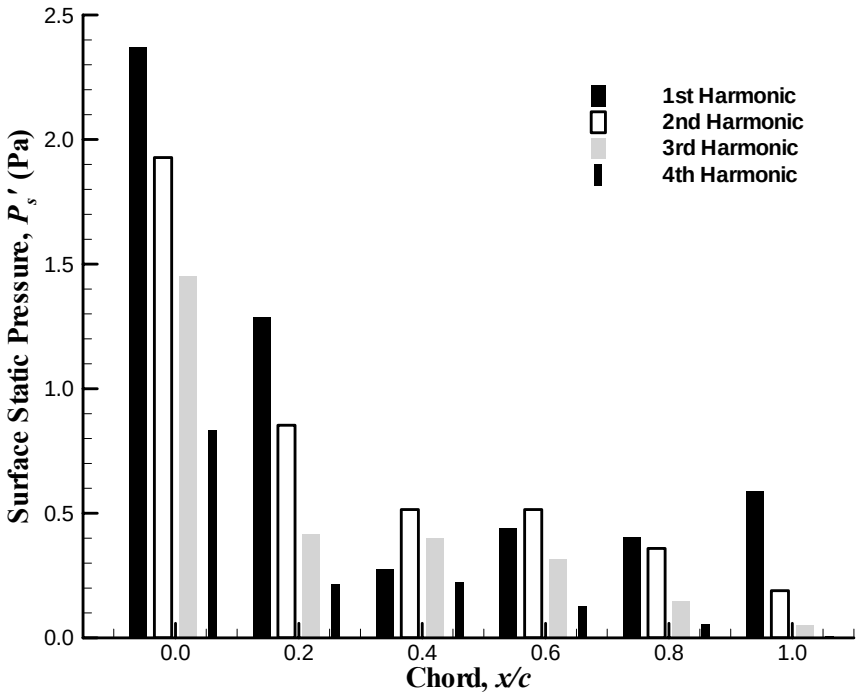

Figure 5-17 NACA 0012 Upper-Surface Static Pressure Spectral Content.

Spectral content related to the airfoil lower-surface pressure time series is depicted in Figure 5-18, corresponding to the time-series data of Figure 5-16. Similar to the airfoil upper surface, the lower surface shows relevant surface-pressure frequencies reaching four times the aerodynamic-forcing frequency, as well as increased higher-order pressure harmonics near the airfoil leading edge. The first-harmonic amplitude shows a similar trend to the upper surface, decaying downstream until x/c = 0.6 and then increasing. Unlike the upper surface, the second harmonic amplitude decays constantly downstream, always having lower amplitude than the first harmonic. Higher order harmonics decay downstream along the airfoil lower surface, approximately reaching a zero value near the trailing edge. Again, the change in harmonic content between the upper and lower surfaces indicates a difference in disturbance deformation and interaction over the airfoil lower surface. This statement is supported by Figure 5-16.

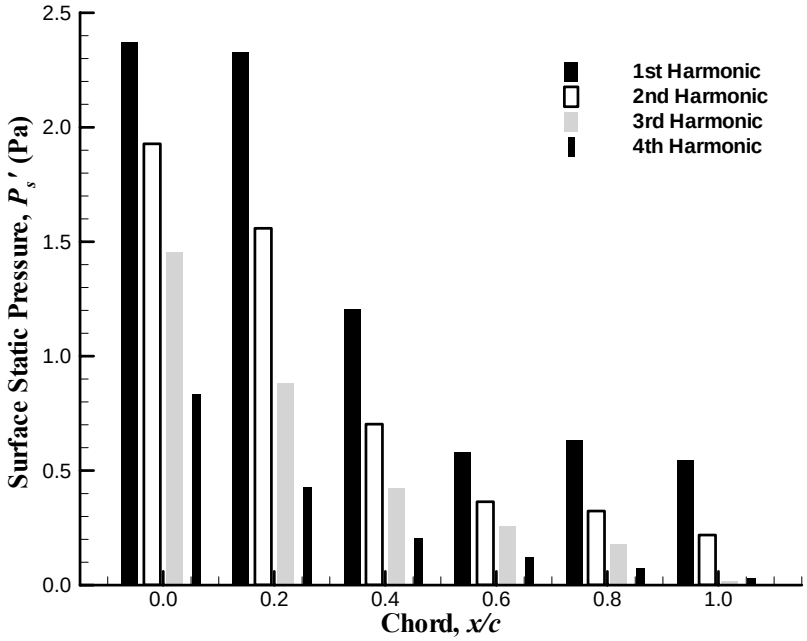

Figure 5-18 NACA 0012 Lower-Surface Static-Pressure Spectral Content.

5.7 AIRFOIL SURFACE-PRESSURE FIRST HARMONIC AMPLITUDE CHORDWISE DEPENDENCY

Figure 5-19 and Figure 5-20 display first-harmonic static-pressure time series at various chordwise locations along the airfoil upper and lower surfaces, respectively. Note, the static-pressure series have been arbitrarily shifted vertically by two units at each successive *x/c* location, to provide better viewing. As expected, these figures indicate periodic pressure variations corresponding to the aerodynamic forcing frequency. A phase shift is also observed between chord locations, (as indicated by the arrows) indicating disturbance propagation direction along the chord. On both upper and lower surfaces, large unsteady pressure fluctuations exist near the airfoil leading edge, decaying rapidly downstream. The overall time-series amplitudes are greater for the lower surface as compared to the upper surface.

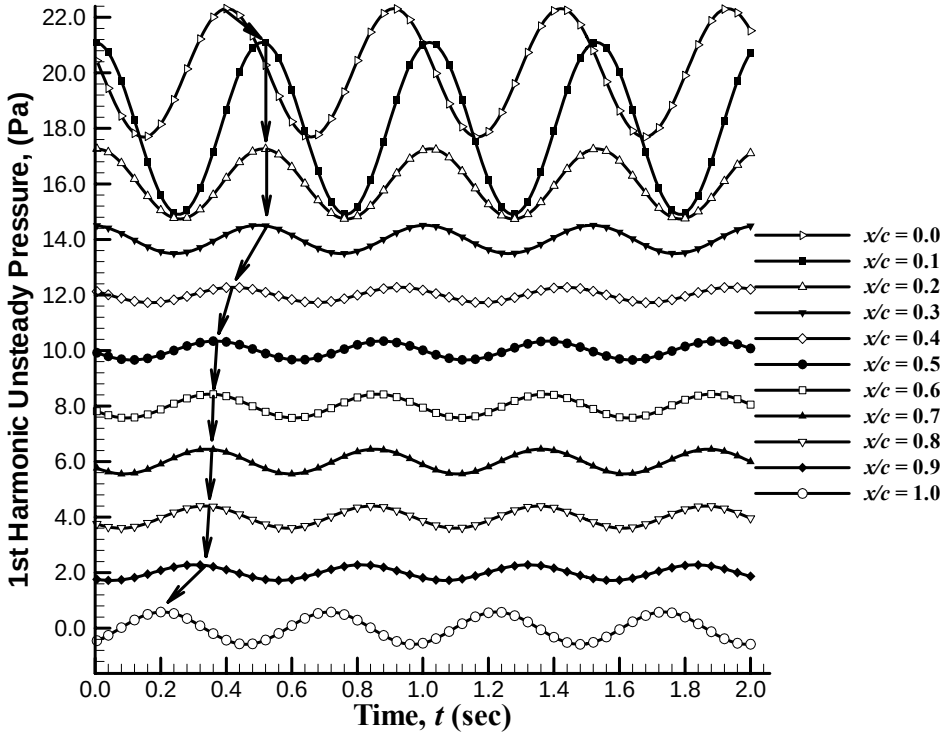

Figure 5-19 NACA 0012 Upper Surface 1st Harmonic Pressure Time series.

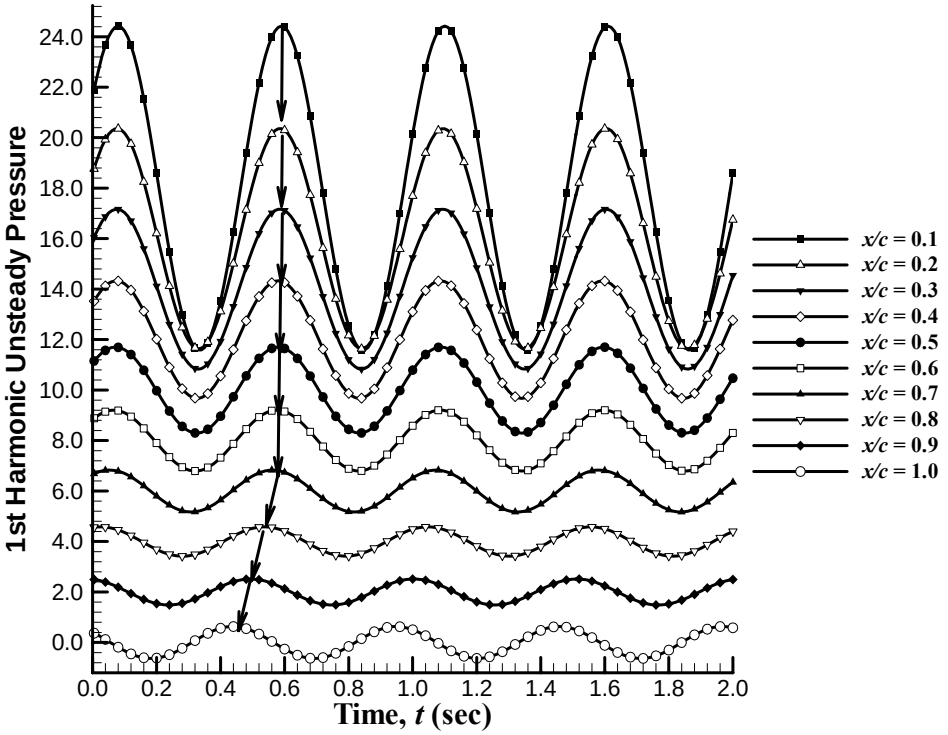

Figure 5-20 NACA 0012 Lower Surface 1st Harmonic Pressure Time series.

Figure 5-21 exhibits first-harmonic pressure amplitude dependence on chord; upper, lower and differential unsteady pressure amplitudes are shown. The airfoil lower surface exhibits higher-amplitude unsteady pressures as compared to the upper surface; thus, confirming inferences made earlier related to Figures 5-19 and 5-20. Upper, lower and differential unsteady pressure amplitudes follow similar chordwise trends; i.e., amplified at leading edge and decaying downstream along the chord.

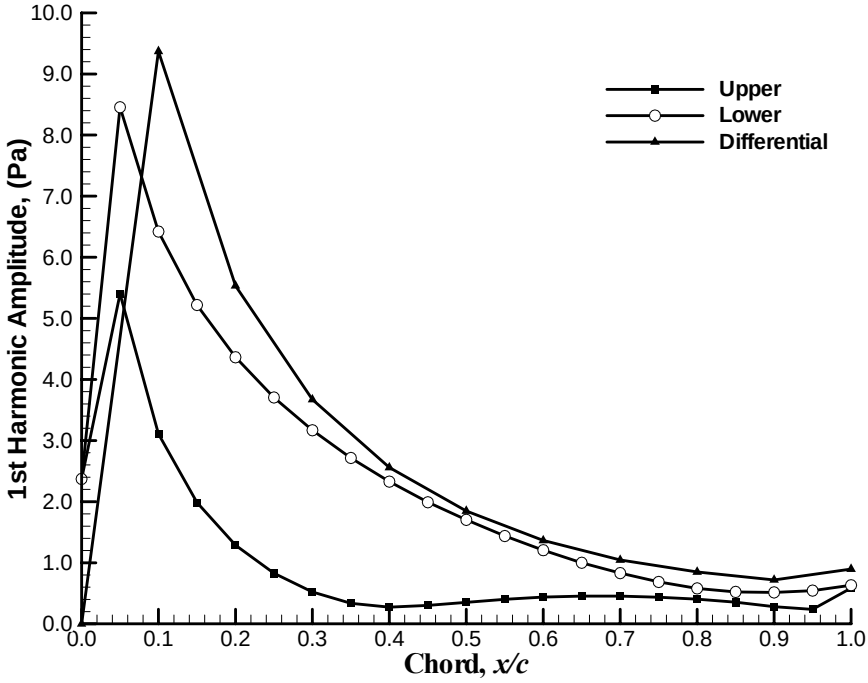

Figure 5-21 NACA 0012 1st Harmonic Pressure Amplitude.

5.8 AIRFOIL SURFACE-PRESSURE FIRST HARMONIC CHORDWISE PHASE DEPENDENCY

Figure 5-22 shows relative phase data for the first-harmonic unsteady surface pressures along the airfoil. The figure displays airfoil upper-surface, lower-surface and differential pressure phase along the airfoil chord.

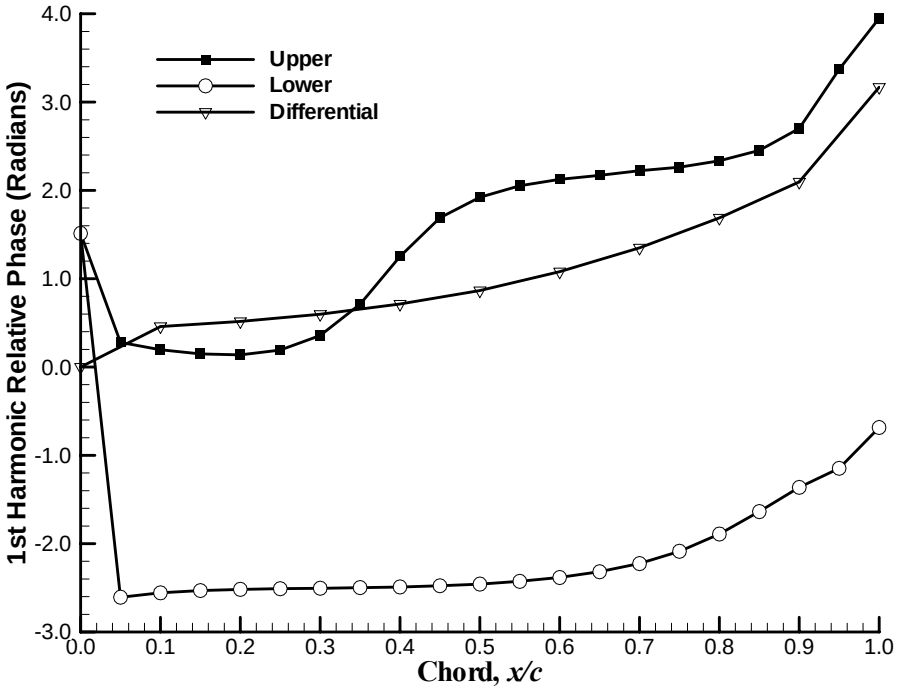

Figure 5-22 NACA 0012 1st Harmonic Phase.

Several important results can be immediately obtained from Figure 5-22. First, the upper-surface and lower-surface phase data exhibit different chordwise trends. Second, the upper-surface data show a significantly varying slope, particularly near the leading and trailing edges. Third, the lower-surface phase exhibits almost no slope near the mid-chord, increasing in slope towards the trailing edge. Finally, phase changes appear rapidly near the leading edges on both upper and lower surfaces.

Fabian and Jumper [1996] established phase-map analysis as a viable means of determining airfoil disturbance-propagation characteristics in an unsteady flow. Fabian and Jumper argued that a negative slope in a phase map, such as near the leading edge in Figure 5-22, indicates downstream-propagating surface-pressure waves, while a positive slope predicts upstream-propagating disturbances. Clearly, if these arguments are true, the data in Figure 5-22 exhibit non-physical disturbance-propagation characteristics.

Similar non-physical phase data were also discussed by Fabian and Jumper, from which they indicated “ambiguous” phase maps, like the one in Figure 5-22, most likely result from multiple pressure disturbances interacting over the airfoil chord.

5.9 AIRFOIL SURFACE-PRESSURE ANALYTICAL MODEL

The phase data of Figure 5-22 display ambiguous disturbance propagation, similar to that discussed by Fabian and Jumper [1996]. The phase data do not follow the convected speed along the airfoil, from which the downstream propagation of an airfoil forcing disturbance would exhibit a negative phase slope. In fact, based on the results of Fabian and Jumper, the upper-surface phase data of Figure 5-22 suggest an initially downstream-propagating disturbance from x/c = 0.0 to x/c = 0.1, with the disturbance gaining speed from x/c = 0.1 to x/c = 0.3, as evidenced by the flat phase slope. At x/c = 0.3, the disturbance presumably changes direction, propagating upstream from x/c = 0.55 to x/c = 0.8. Finally, the disturbance propagates upstream at a lower speed near the airfoil trailing edge. Conversely, the lower-surface phase map of Figure 5-22 suggests an initially downstream-propagating disturbance gaining speed from x/c = 0.1 to x/c = 0.65, finally propagating upstream near the airfoil trailing edge.

These inferences are reinforced by examining the fundamental (first-harmonic) frequency time series in Figure 5-19 and Figure 5-20, for the airfoil upper and lower surfaces, respectively. In Figures 5-19 and 5-20, the probable propagation direction of the waveforms from the leading edge to each successive x/c location has been indicated, where it has been assumed that the minimum time between each successive pressure peak provides the correct wave propagation direction. When compared to the upper-surface

and lower-surface phase maps of Figure 5-22, the wave propagation directions in Figure 5-19 and 5-20 are consistent, showing the same overall chordwise characteristics.

5.9.1 INTERACTION MODEL

Although the phase information in Figures 5-19, 5-20 and 5-22 correlate, the disturbance propagation directions implied by the data are clearly non-physical and incorrect. In the investigation of Fabian and Jumper, ambiguous phase maps similar to Figure 5-22 were argued to result from convectively-propagating vortical and acoustically-radiating potential disturbance interactions across their examined airfoil [1996]. These arguments were made based on airfoil surface-pressure response measurements, indicating airfoil aerodynamic forcing to be made up of two types of disturbances; these disturbances having the same primary forcing frequency, similar orders of magnitude, but different propagation speeds.

In the light of these previous arguments, it is conjectured here that the phase behavior in Figure 5-22 also results from interaction between two separate pressure disturbances in the computed field; both disturbances induced by the aerodynamic forcing function employed for airfoil unsteady forcing. In this case, these two disturbances are assumed to have the same primary forcing frequency, but different amplitudes and propagation characteristics.

Given these assumptions, a simple disturbance-interaction model is developed with the goal of eliciting the primary physical mechanisms leading to the ambiguous phase behavior of Figure 5-22. To this end, the model attempts to analytically reproduce the waveform characteristics observed in the upper-surface first-harmonic time series data of Figure 5-19. This model is comprised of two types of pressure disturbances: a

convectively propagating pressure wave, approximated by a wake-like function, and an acoustically propagating potential wave, approximated by a sine function. The convective pressure wave models the local influence of the passing wake over the airfoil, while the acoustic wave models the global potential-field response to airfoil lift, or circulation, changes in the unsteady flow. Note that this model is not developed with the intent to exactly reproduce the first-harmonic time-series data in Figure 5-19, but rather mimic the primary data characteristics.

The convectively propagating pressure wave was originally modeled after the rotor-wake, as discussed in Section 3.4.1. This model provides a smooth wake function with a pressure deficit decaying monotonically in the far-field. The equation for unsteady pressure produced by this wake-function is modeled as

$$P_v' = A_v e^{(-\delta y^2)} \qquad \textbf{5. 2}$$

Unfortunately, the wake model of Equation 5.2 does not easily account for wake convection, and may not properly account for wake decay across the airfoil. Therefore, wake time series were extracted from the periodic boundary of the computational domain, at x locations corresponding to x/c = 0.0 – 1.0. Wake extraction at this location correctly provides wake convection speeds and decay with x/c distance, although it does not account for wake deformation due to non-linear interactions with the airfoil. Figure 5-23 displays the extracted wake-induced pressure time series at various locations corresponding to airfoil chord. As expected, a decrease in amplitude is seen as the wake propagates downstream. A monotonic phase shift is also observed between locations corresponding to the airfoil chord, indicating constant-speed disturbance convection.

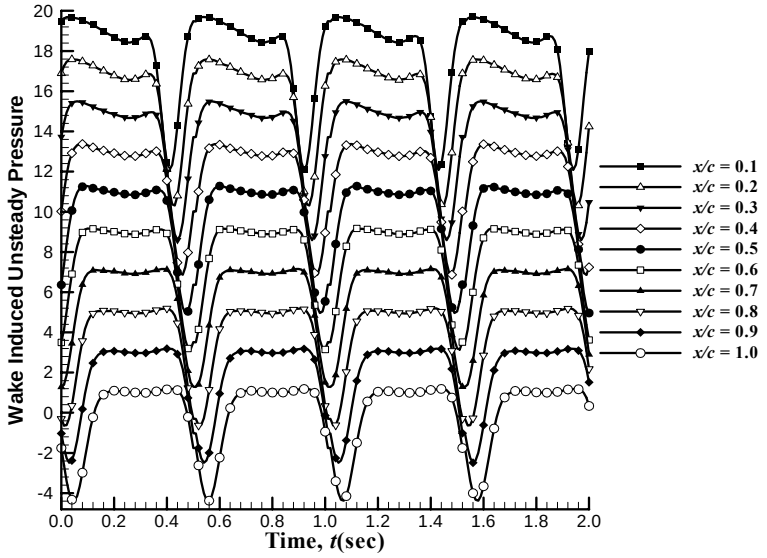

Figure 5-23 Wake Induced Pressure Time Series Collected at the Periodic Boundary.

The acoustic potential wave in the interaction model is patterned after a sine wave, as lift/circulation about the airfoil varies sinusoidally. The assumed equation for unsteady pressure created by the lift-induced potential disturbances is thus modeled as

$$P_a' = A_a \sin(2\pi ft + \phi) \qquad \textbf{5.3}$$

Assumptions inherent to Equation 5.3 imply wake impact, and subsequent propagation, over the airfoil cause a potential-field response, related to airfoil circulation. This response propagates in the field acoustically, providing a near instantaneous pressure change on the airfoil, contrasting the local pressure disturbance created by the convecting wake.

Interactions between the two pressure disturbances across the airfoil are modeled through the addition of waveforms found in Figure 5-23 and Equation 5.3. The resultant modeled pressure field therefore has two unknowns A_a and ϕ. To find appropriate values for these unknowns, A_a and ϕ were optimized such that the interaction model produced

unsteady pressure first-harmonic time series approximating the computationally obtained results.

Figure 5-24 displays the final optimized lift-induced pressure time series at various chordwise locations along the airfoil upper surface, corresponding to Equation 5.3. Note, the pressure series have been shifted vertically by two units at each successive *x/c* location, to provide better viewing. While the amplitude at each *x/c* location was varied in the optimization, with the leading edge having the highest amplitude and decreasing downstream, the phase at each *x/c* location was held constant. A constant phase relationship models the near instantaneous acoustic potential-wave propagation in the modeled low-speed field (i.e., at $M = 0.03$).

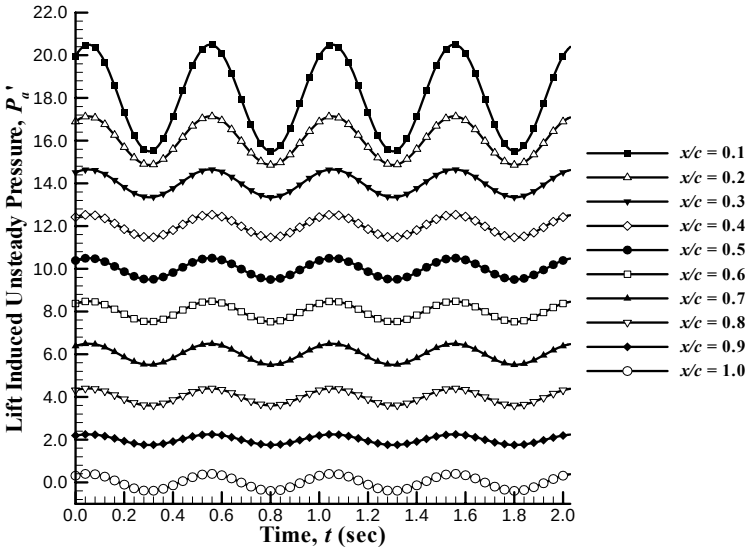

Figure 5-24 Optimized Lift-Induced Pressure Time Series.

Figure 5-25 displays the interaction model first-harmonic time series at various chordwise locations along the airfoil upper surface, created by adding the time series of Figures 5-23 and 5-24. Note, the static pressure series have been shifted vertically by two units for each *x/c* location, in order to provide better viewing. By comparing the

analytically obtained first-harmonic time-series data, shown in Figure 5-25, to the computationally obtained times series data of Figure 5-19, several observations are made. First the overall amplitude of the interaction model time series is found to be slightly higher than the computationally obtained time series. Second, similar trends in terms of amplitude (decreasing downstream) and periodicity are seen in both sets of obtained time-series data. The time series data of Figure 5-25 also exhibit a phase shift similar to that seen in the computational data.

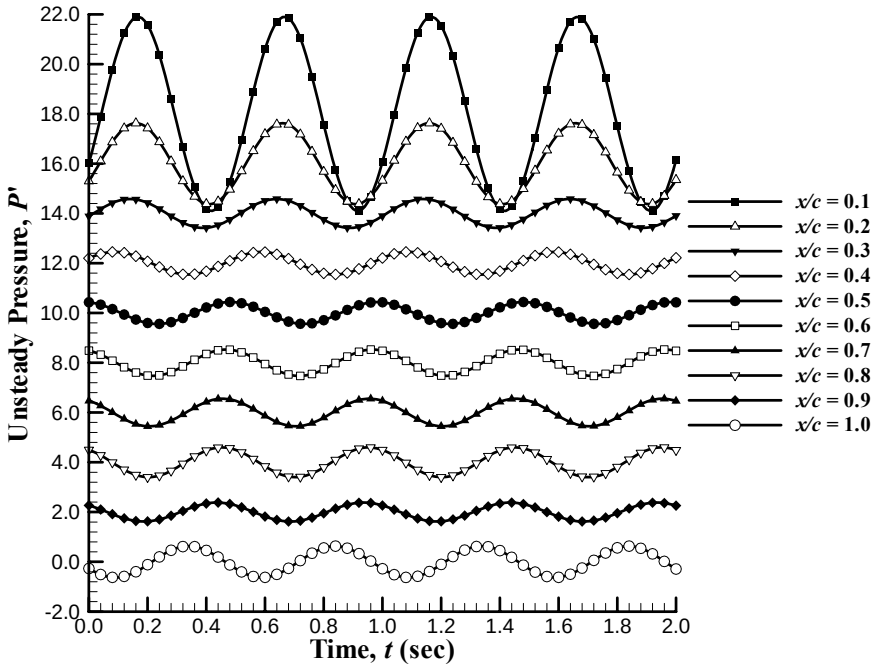

Figure 5-25 Interaction Model 1st Harmonic Time series.

While the time series of Figure 5-25 approximately model the computed first-harmonic series, the data do not account for airfoil thickness effects. Since pressure waves representing the forcing wake were collected at the periodic boundary (i.e. on a line of constant *y*, but varying *x*), the data essentially represent wake propagation along a flat plate. The effects of airfoil thickness would tend to delay wake propagation (or create a phase lag) on airfoil upper surface as compared to flat-plate propagation speeds. This is

illustrated in Figure 5-26. The described time delay relates to the additional time necessary for a disturbance to reach the same *x/c* location on the airfoil surface as it would on a flat plate. This delay is defined by the airfoil thickness Δy_i at a particular *x/c* location, divided by the velocity, *V*, at which the disturbance propagates vertically upward .In terms of phase, Equation 5.4 provides the approximate phase delay caused by airfoil thickness.

$$\Delta\phi = \frac{2\pi f \Delta y_i}{V} \tag{5.4}$$

Thus, accounting for the described phase lag, the extracted wake data in Figure 5-23 are modified to account for airfoil thickness effects.

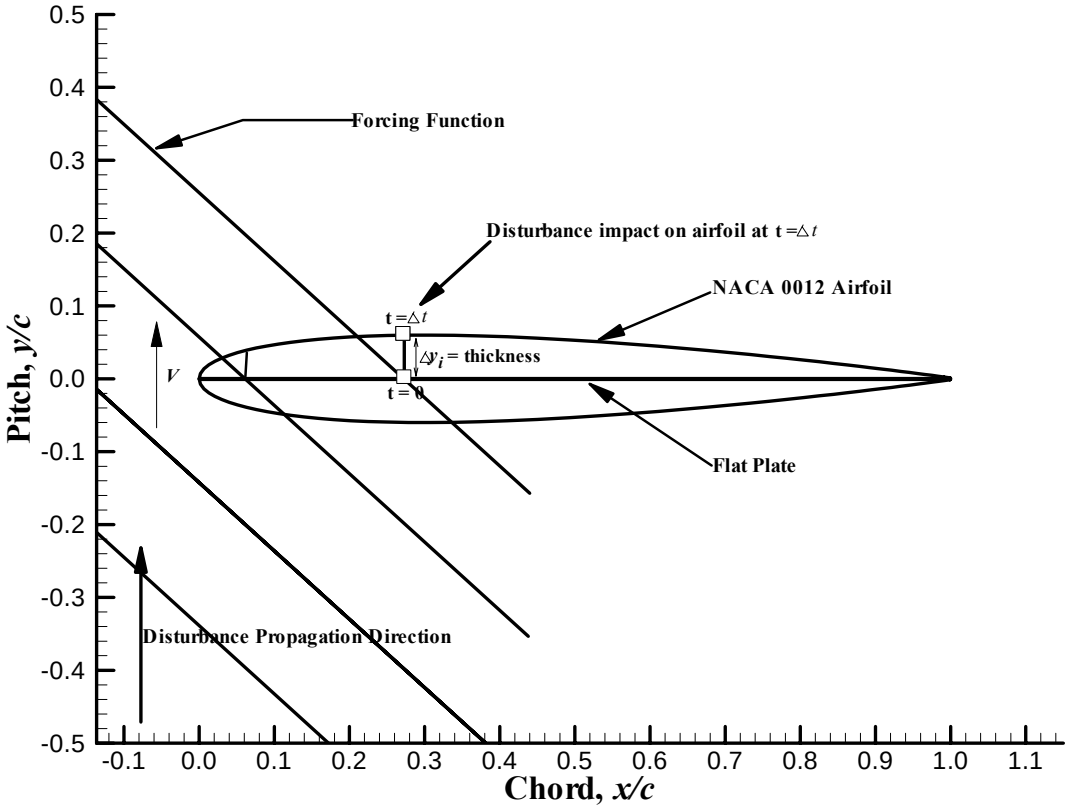

Figure 5-26 Propagating Disturbance Model.

5.9.2 INTERACTION MODEL RESULTS

Figure 5-27 exhibits first-harmonic pressure amplitude dependence on chord for both interaction and computational models. Similar to the computational data, the interaction model data exhibit amplified leading-edge pressures decaying downstream along the chord. While both data sets exhibit similar trends, the interaction model produces slightly higher amplitudes compared to the computational results.

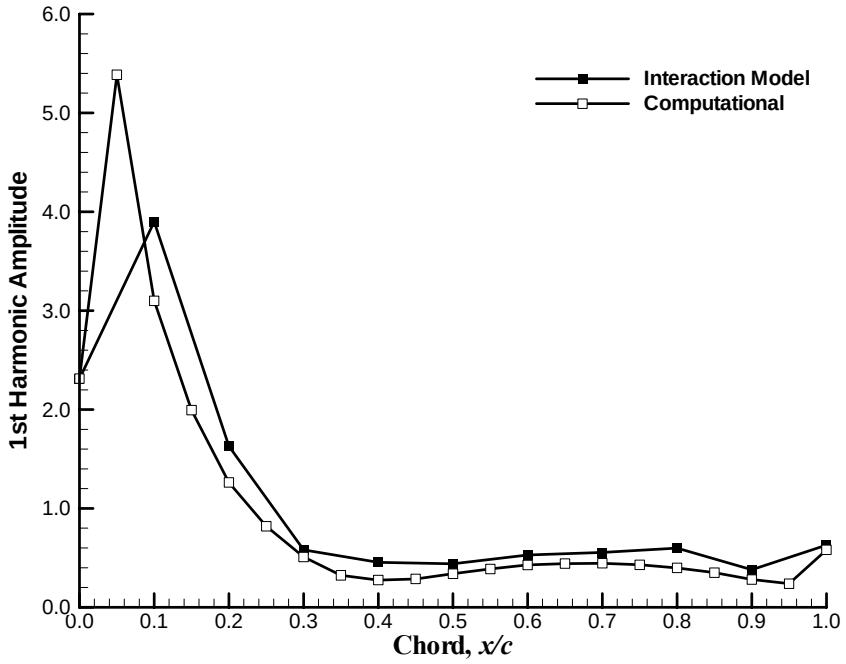

Figure 5-27 1st Harmonic Amplitude Comparison.

Figure 5-28 displays phase data computed using the disturbance interaction model. This figure displays modeled upper-surface pressure phase along the NACA 0012 airfoil, using both flat-plate and thickness-corrected models. As seen in the figure, the analytically obtained phase data show trends similar to the computational data. In particular, phase trends exhibit similar ambiguity in terms of disturbance propagation direction. Given the analytical and computational phase data agreement, the existence of convectively-propagating and acoustically propagating pressure wave interaction is, at

the very least, consistent with the observed characteristics of the lifting-surface data. As such, model agreement provides presumptive evidence that the major interacting pressure components in the lifting-surface aerodynamic forcing field have been identified. Finally note that airfoil thickness effects tend to increase the phase slope near mid chord, as compared to the flat plate. The influence of airfoil thickness on phase will be discussed further in Chapter 6.

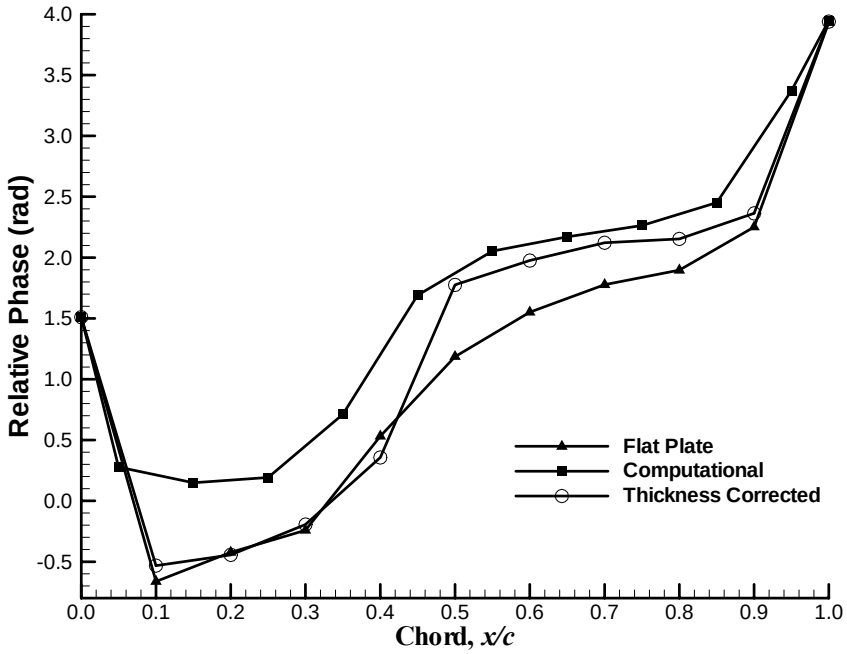

Figure 5-28 Interaction Model 1st Harmonic Phase: Upper-Surface.

Phase data computed using the interaction model along the lower surface of the NACA 0012 airfoil is displayed in Figure 5-29. To obtain the lower surface phase data, re-optimization of the interaction model was performed such that the computationally obtained time-series data along the lower surface was correctly modeled. As seen in Figure 5-29, the analytically obtained phase data show trends similar to the computational data with slightly lower phase magnitudes. Similar to the computational data, the interaction model phase shows rapidly varying phase slopes near the leading and

trailing edge regions. As such, model agreement provides further presumptive evidence that the major interacting pressure components in the lifting-surface aerodynamic forcing field have been identified.

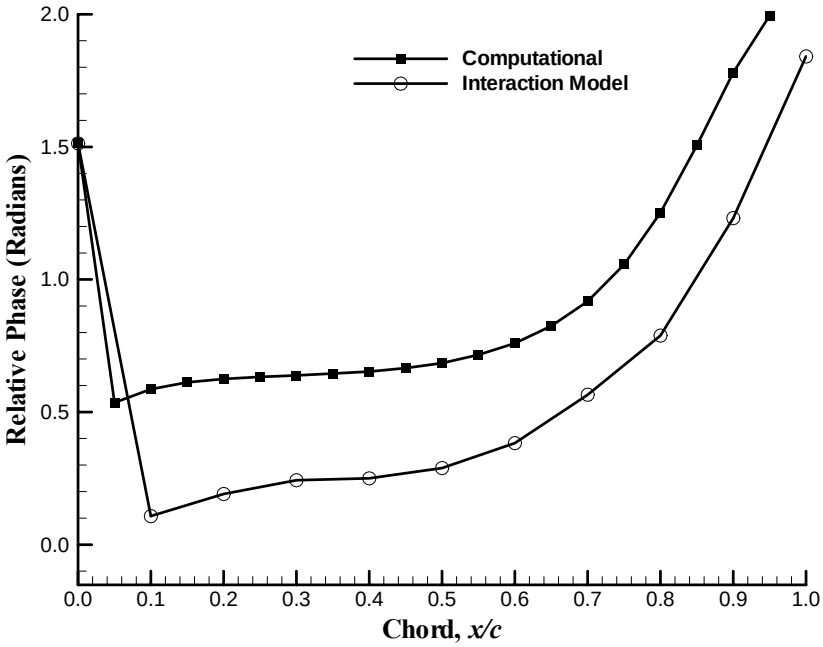

Figure 5-29 Interaction Model 1st Harmonic Phase: Lower-Surface.

5.10 SUMMARY

Unsteady pressure time series data collected along the NACA 0012 airfoil upper and lower surfaces indicate periodic static-pressure variations corresponding to the aerodynamic forcing frequency. The pressure fluctuations, although periodic, are not purely sinusoidal, indicating the existence of harmonic content. Spectral analysis shows surface-pressure harmonic frequencies reaching four times the aerodynamic forcing frequency. Both upper and lower surfaces exhibit increased higher-order pressure harmonics near the airfoil leading edge, generally decaying downstream such that third and fourth harmonic amplitudes almost vanish near the airfoil trailing edge.

First-harmonic phase data exhibit ambiguous disturbance position-vs.-phase maps, from which disturbance propagation direction can not be inferred. Based on the results of Fabian and Jumper, the ambiguous phase results suggest the existence of multiple disturbance interactions across the airfoil, these disturbances having the same primary frequency, but different amplitudes and propagation speeds. A first-order disturbance-interaction model was developed in an attempt to reproduce the ambiguous phase behavior, incorporating a local convectively propagating pressure wave and a global acoustically propagating potential wave. Both disturbances exhibit identical forcing frequencies, but exclusive amplitudes, waveform shapes, and propagation speeds.

The analytically modeled pressure data mimick computationally obtained results quite well. The amplitude of the modeled data was slightly higher at each chordwise location; however, the corresponding phase data exhibit similar ambiguity in terms of disturbance propagation direction. Thus, presumptive evidence was obtained suggesting phase-map ambiguity in the modeled NACA 0012 data results from interaction between local convectively propagating and global acoustically propagating pressure waves.

6 Chapter 6

PARAMETRIC ANALYSIS

This chapter describes results obtained from parametric analyses performed to examine airfoil time-resolved surface pressure phase dependencies. Nominal results are presented for three symmetric NACA airfoil profiles of 10, 15 and 20% thickness (relative to chord), two cambered airfoils of 2 and 6% camber (relative to chord) and two mean-flow attack angles of 5 and 10 degrees. Unsteady results are reported in terms of chordwise unsteady surface-pressure distribution, spectral content, and phase.

6.1 DATA REDUCTION METHODOLOGY

Unsteady pressure results were obtained in the same manner as described in Chapter 5, removing the time-average value from the instantaneous pressure via

$$P' = P - \overline{P} \tag{6.1}$$

Unsteady pressure data were further reduced into elements of amplitude, frequency, and phase for first, second and third harmonics (i.e. one, two and three times the fundamental frequency). Only the first harmonic results are presented in this chapter. Harmonic decomposition was accomplished via Fast-Fourier Transform (FFT) techniques.

6.2 AIRFOIL THICKNESS INFLUENCE

The influence of lifting-surface thickness on surface-pressure phase is examined via simulation of three symmetric NACA profiles of 10, 15, and 20% thickness (based on

chord). Time series data for all thickness profiles are provided in Appendix E. As expected, first-harmonic amplitude time series indicate periodic static-pressure variations corresponding to the aerodynamic-forcing frequency. A phase shift is also observed between chord locations, suggesting disturbance propagation direction along the chord. On both upper and lower surfaces, large unsteady pressure fluctuations exist near the airfoil leading edge, decaying rapidly downstream. The overall time series amplitudes are greater for the lower surface as compared to the upper surface, as observed for all thickness profiles.

Figure 6-1 exhibits first-harmonic unsteady pressure amplitude dependence on chord for the examined lifting-surface thicknesses; both upper and lower surface unsteady pressures are shown. Examining Figure 6-1, several observations can be made. First, unsteady pressure is significantly amplified at the airfoil leading edge, decaying downstream along the chord. This trend is observed for all thickness profiles and is attributed to disturbance interaction and deformation at impact with the airfoil. Second, as thickness increases unsteady pressure amplitude on both upper and lower surfaces also slightly increases, with the lower surface exhibiting higher-amplitude compared to the upper surface for all thicknesses. Third, between $x/c = 0.2$ and $x/c = 0.4$ along the airfoil upper surface, unsteady pressure amplitude is marginally higher for the NACA 0010 airfoil decreasing as the thickness increases. In general, airfoil thickness plays little role in unsteady surface-pressure amplitude.

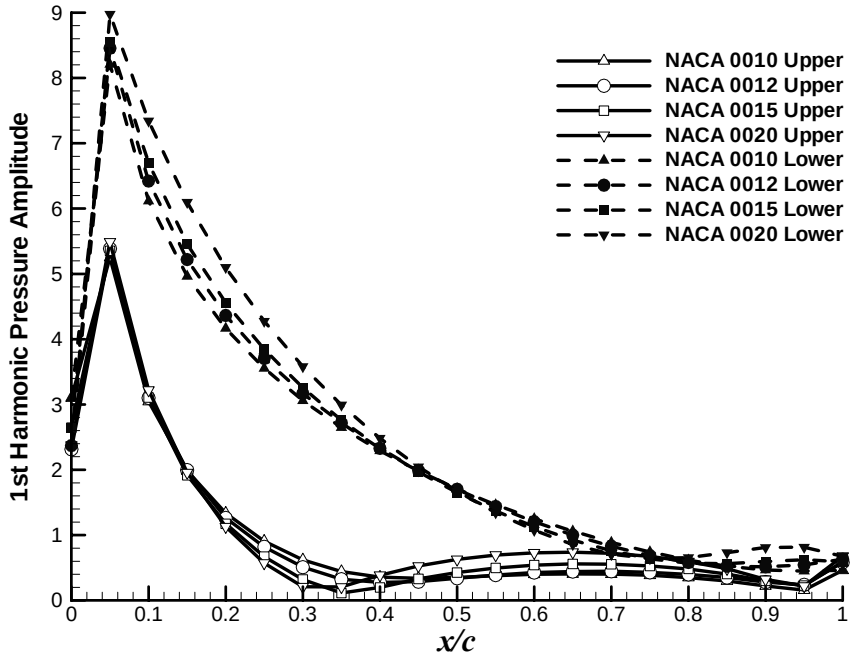

Figure 6-1 1st Harmonic Pressure Amplitude: Various Lifting-Surface Thicknesses.

Figure 6-2 displays first-harmonic chordwise phase along the upper and lower surfaces for the various lifting-surface thicknesses. Similar trends are seen in the phase data for all airfoil thicknesses. Similar to the baseline NACA 0012 data of Chapter 5, the upper surface of each airfoil shows significantly varying phase slope, while the lower surface exhibits almost no slope. As thickness increases, a rapid increase in positive slope between $x/c = 0.3$ and $x/c = 0.4$ occurs on the airfoil upper surface. Conversely, lower-surface phase data in Figure 6-2 indicate little dependence on airfoil thickness.

Based on the results of Chapter 5, upper-surface phase changes near mid-chord due to airfoil thickness are attributed to increased disturbance propagation delay. The disturbance must travel further along the surface at higher thickness values, delaying their progress along the chord, causing the observed phase behavior. This behavior is illustrated in Figure 5-26, with the phase difference between airfoils of different thickness

modeled in Figure 5-28. Clearly Figure 5-28 shows increased thickness causes an increase in phase slope near the airfoil mid-chord.

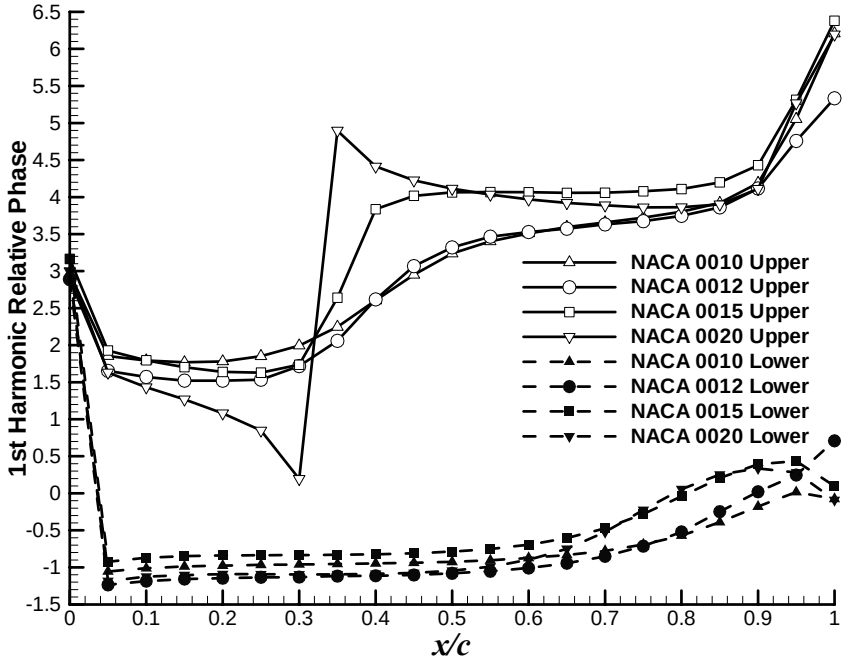

Figure 6-2 1st Harmonic Phase : Various Lifting-Surface Thicknesses.

6.3 AIRFOIL CAMBER INFLUENCE

First-harmonic pressure amplitude time series at various chordwise locations along the upper and lower surfaces of the examined cambered airfoils are presented in Appendix F. Similar to the airfoil thickness investigation, periodic pressure variations corresponding to the aerodynamic forcing frequency, and a phase shift between sequential chordwise locations indicating disturbance propagation, are observed. Large unsteady pressure fluctuations again exist near the cambered airfoil leading edge on both upper and lowers surfaces, decaying downstream. When compared to the symmetric airfoil first-harmonic pressure amplitude series in Figures 5-21 and 5-22, the cambered airfoils tend to have higher overall time series amplitudes.

Figure 6-3 displays upper-surface and lower-surface first-harmonic unsteady pressure dependence on chord for the symmetric, 2% (NACA 2412) and 6% (NACA 6412) camber airfoils. Several observations can be made from Figure 6-3. First, the lower surface exhibits higher-amplitude unsteady pressures for all airfoils. Second, unsteady pressure amplitude along the upper surface slightly increases as camber increases, with the 6%-camber airfoil having the highest amplitude. Along the lower surface however, unsteady pressure decreases as camber increases. Third, pressure amplification occurs on the upper surface of all airfoils between $x/c = 0.4$ and $x/c = 0.95$, which is not mirrored on the lower surface. Finally, unsteady pressure amplitude in all cases is amplified at the leading edge, having maximum value at $x/c = 0.05$, decaying in strength downstream

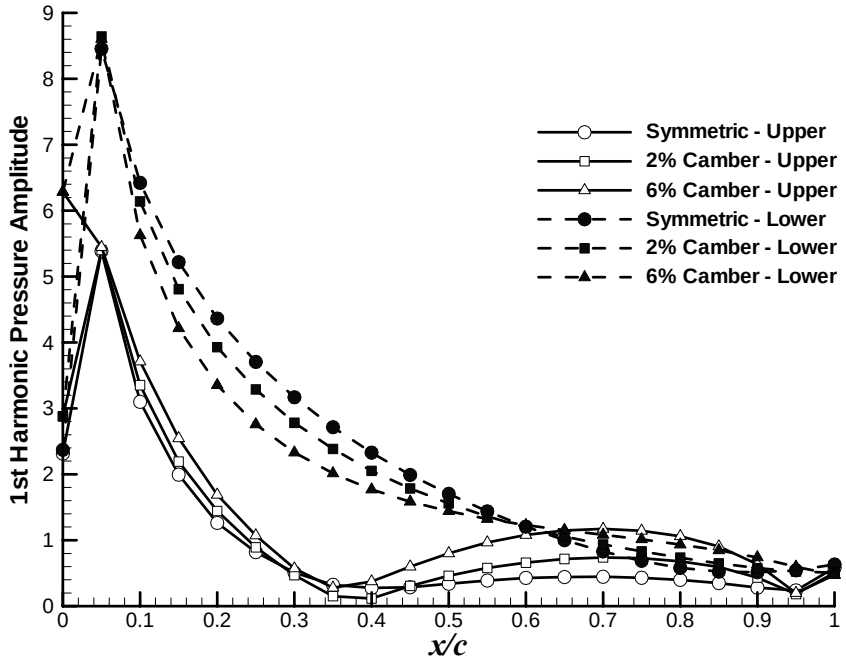

Figure 6-3 1st Harmonic Amplitude: Various Lifting-Surface Cambers.

.

Figure 6-4 shows relative phase for the first-harmonic surface-pressure data. The figure displays phase data along the upper and lower surfaces for the symmetric, 2% and 6% camber lifting-surfaces. Relative phase data for the various cambers follow similar trends to the symmetric airfoil. In particular, phase data on the upper surface show significantly varying slope, while the lower surface phase exhibits almost no slope. In fact, as camber increases the phase change near mid-chord, also observed for the various thickness cases, exacerbates. Based on arguments made in Chapter 5, the mid-chord phase behavior exhibited in Figure 6-4 likely corresponds to convective wake propagation speed changes with camber; i.e., more camber delaying downstream propagation as compared to the symmetric case. Based on this presumption, the physical mechanisms leading to the phase trends with camber are the same as those influencing phase trends with various airfoil thicknesses.

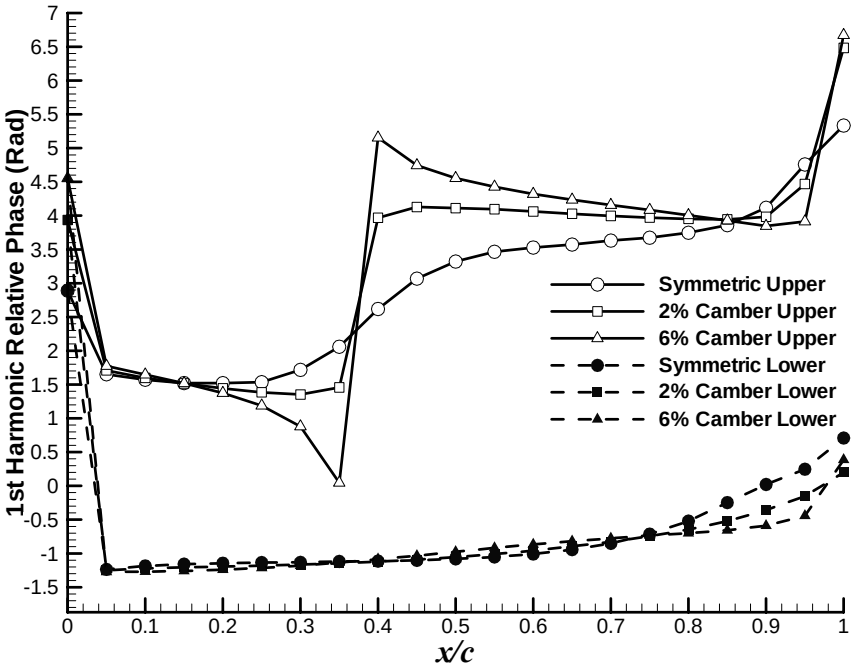

Figure 6-4 1st Harmonic Phase: Various Lifting-Surface Cambers.

6.4 ANGLE OF ATTACK INFLUENCE

As mentioned in Chapter 3, the influence of mean-flow angle of attack (AOA) on surface-pressure phase is examined via simulation of a NACA 0012 airfoil at 0, 5 and 10 degrees AOA. Upper-surface and lower-surface time series corresponding to these simulations are presented in Appendix G. Once again, periodic static-pressure variations corresponding to the aerodynamic-forcing frequency are found, as well as a phase shift between chord locations, indicating disturbance propagation direction. On both upper and lower surfaces, large unsteady pressure fluctuations occur near the airfoil leading edge, decaying rapidly downstream. Higher magnitude unsteady pressure amplitudes occur on the lower, as compared to the upper surface. Overall time-series amplitudes show a small increase as AOA increases.

Figure 6-5 displays upper-surface and lower-surface first-harmonic unsteady pressure dependence on chord for 0, 5 and 10-degrees mean-flow AOA. Several observations can be made from Figure 6-5. First, as AOA increases, pressure amplitude at the leading edge increases. Second, unsteady pressure amplitudes for different AOA follow similar trends (amplified at the leading edge and decaying downstream). The 10-degree AOA case has high amplitudes near the leading edge; however, on the upper surface between x/c = 0.15 to x/c = 0.3, the 0-degree AOA flow has the highest amplitude. Along the aft section of the airfoil (i.e., between x/c = 0.75 to x/c = 1.0), unsteady pressures on both the upper and lower surfaces equalize. In all, AOA has little influence on amplitude downstream of x/c = 0.2.

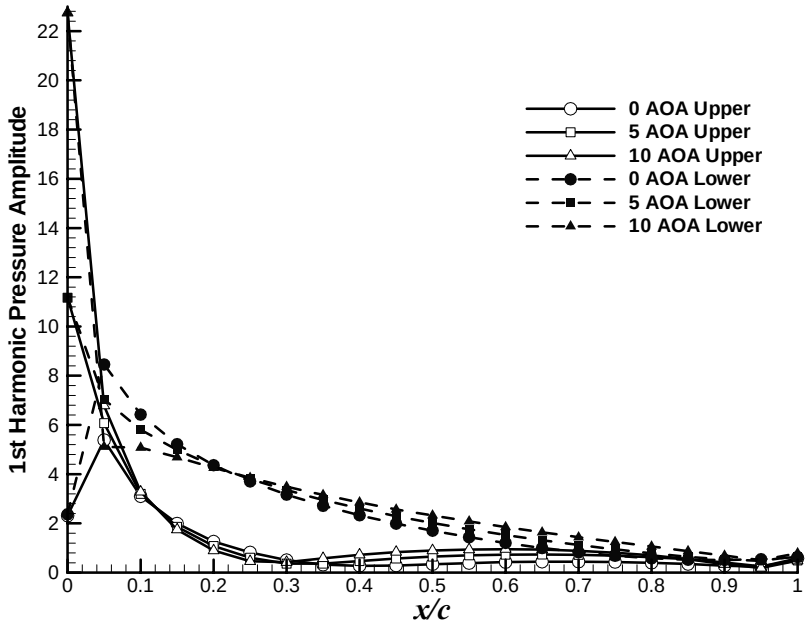

Figure 6-5 1st Harmonic Amplitude: Various Mean-Flow Angles of Attack.

Figure 6-6 shows relative phase data for the first-harmonic surface-pressure data. The figure depicts data along the upper and lower surfaces of a symmetric NACA 0012 profile at 0, 5, and 10-degree AOA. In Figure 6-6, upper-surface and lower-surface phase data exhibit different chordwise trends, but very similar to all phase data reported herein. On the upper surface, large mid-chord phase changes occur as AOA increases. The lower surface however, shows little dependence on AOA; similar to the relative lack of lower-surface phase dependence on airfoil thickness and camber. Unlike the thickness and camber analyses, increasing AOA does not cause a large change in mid-chord phase slope, but rather a shift in mid-chord phase variation toward the leading edge. Again, this can be inferred based on the results of Chapter 5, as AOA does not alter airfoil geometry, (i.e., the amount of phase delay due to airfoil curvature does not change) but rather the location of the time-average leading-edge stagnation point on the airfoil does change. Geometric airfoil changes, like increased thickness or camber, presumably delay

convected wake propagation over the airfoil on the upper surface due to curvature effects. Conversely, AOA changes merely shift the convective wake and potential disturbance interactions along the chord, and the stagnation point (and therefore the propagation distance) changes.

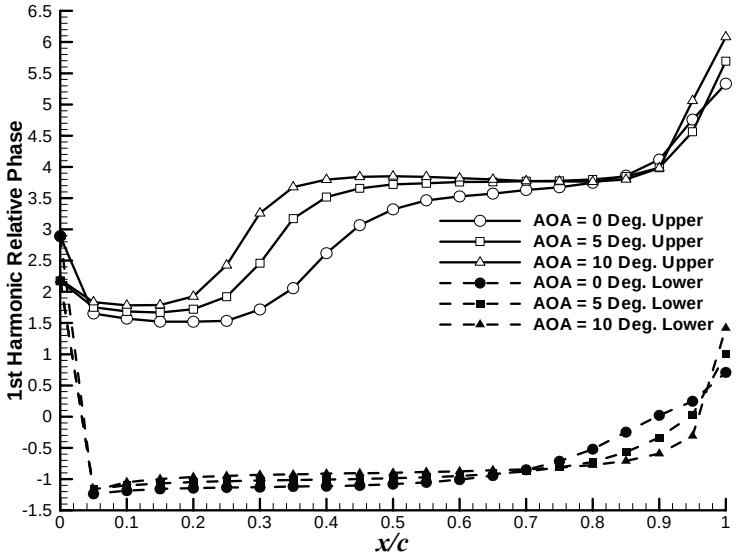

Figure 6-6 1st Harmonic Phase: Various Mean Flow Angles of Attack.

6.5 SUMMARY

Parametric analyses were performed to examine airfoil time-resolved surface pressure phase dependencies on airfoil thickness, camber and mean-flow AOA. Results were presented for three symmetric NACA profiles of 10, 15, and 20 % thickness (relative to chord), two cambered airfoils of 2 and 6% camber (relative to chord) and two mean-flow attack angles of 5 and 10 degrees.

First-harmonic pressure amplitude time-series data for the various thickness, camber and AOA profiles exhibit similar trends in terms of periodic static-pressure variations (corresponding to the aerodynamic-forcing frequency), large unsteady pressure fluctuations near the leading edge (decaying downstream) and a phase shift between

chordwise locations. As thickness and AOA were increased, small changes were seen in the time series amplitudes. However, with the increase in camber, time series amplitudes showed significant amplification specifically in the upper surface aft chord region (i.e., x/c = 0.5 - 0.9). Pressure amplitudes for the various thickness, camber and AOA cases also showed similar trends, being amplified at the leading edge and decaying along the chord. In general, increases in first-harmonic pressure amplitude were seen as thickness, camber and AOA increased, with higher AOA providing significant amplifcation near the leading edge.

First-harmonic phase data along the upper surface of the various thickness, camber and AOA cases exhibited significantly varying slopes, while the lower surface data exhibited little slope change with each case. As thickness and camber increased, rapid increases in positive phase slope occured near the airfoil upper-surface mid-chord. This is attributed to increased convected-disturbance propagation delay at higher thickness and camber values as eluded to in Chapter 5. Unlike thickness and camber results, increasing AOA did not cause an increase in mid-chord phase slope, but rather a shift in mid-chord phase variations toward the leading edge. This is attributed to the static airfoil geometry of the AOA cases, with the phase change moving toward the leading edge as the time-average stagnation point moves downstream of the leading edge.

7 CHAPTER 7

STATOR-VANE CASCADE RESULTS

Computational results from an unsteady cascade simulation are discussed in this chapter. Reduction of the pressure data, for both time-averaged and time-accurate quantities, is initially described, with an FFT technique employed to produce unsteady amplitude and phase results. Decomposed unsteady surface-pressure amplitude and phase data are compared to those obtained in a previous experimental investigation. Presented amplitude and phase results show similar characteristics to those obtained in a running F109 engine by Falk [2000].

7.1 DATA REDUCTION METHODOLOGY

7.1.1 Time-Averaged Results

The methodology followed to compute time-averaged results, is similar to that discussed in Chapter 4. Time-averaged parameter distributions are computed by summing flow parameters (i.e., pressure, velocity, etc.) at each grid location along the vane surface over 50 time steps (one aerodynamic forcing period), respectively. Resulting summations are then divided by the number of time steps, giving a time-averaged value for each solution parameter at each grid point.

7.1.2 Unsteady Results

Unsteady pressure results are obtained by removing time-averaged pressures from instantaneous pressures via

$$P' = P - \overline{P}$$

Unsteady pressure data are further reduced into elements of amplitude, frequency, and phase for first, second and third harmonics (i.e. one, two and three times the fundamental frequency) components. This is accomplished via FFT techniques.

7.2 STATOR-VANE CASCADE CONFIGURATION

The simulated cascade configuration employed aerodynamically loaded vanes mimicking the two-dimensional geometry of the stator-vane row in the fan stage of a F109 turbofan engine. The vanes have a double-circular-arc profile, with a maximum camber and thickness of 12% and 8% relative to vane chord, respectively. A complete description of this configuration is discussed in Chapter 3. Mean flow velocity was set to equivalent to $M = 0.57$ in the presented simulations.

Cascade unsteady forcing was achieved through a UDF written in FLUENT, modeling waveform characteristics of a passing rotor wake. The employed UDF is similar to that developed for the airfoil unsteady forcing simulations discussed earlier. However, the frequency of the generated wakes is increased, such that frequency content matched that of the F109 engine.

7.3 TIME-AVERAGED RESULTS

Time-averaged total-pressure contours for a simulated cascade vane, are presented in Figure 7-1, with attached numerical values indicating respective pressure contour

levels. Figure 7-1 indicates good qualtitative behavior of the simulated flowfield, showing a well-behaved total pressure distribution about the vane profile and wake region. The flow on the vane surface also shows no indication of large-scale separation, exhibiting smooth attached flow. Thus, time-averaged flow about the stator vane is argued to be attached and producing wakes similar to that which would be expected. Note, stator-vane wake chractersitics were not reported by Falk [2000].

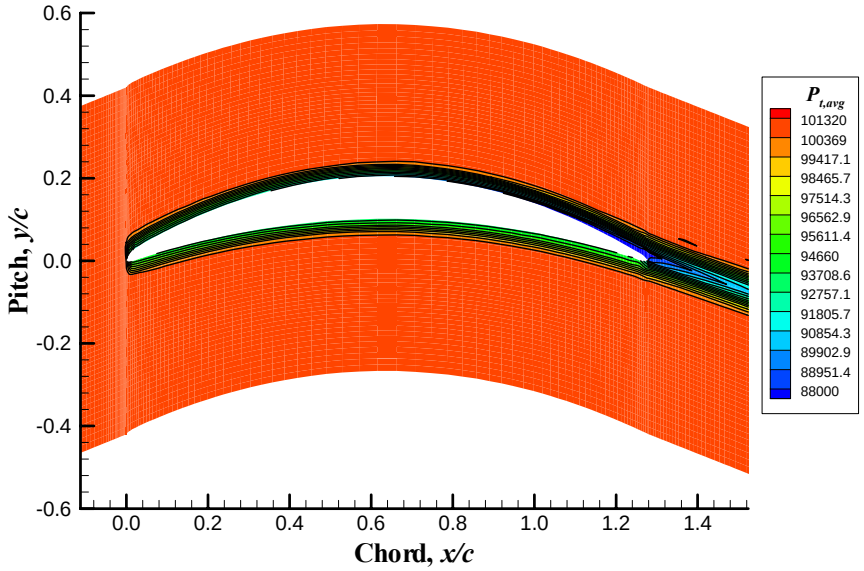

Figure 7-1 Time-Averaged Total -Pressure Contours (Pa).

Figure 7-2 displays time-averaged static pressures computed along the vane chord; pressure distributions along the upper and lower surfaces are individually displayed. As expected, the cambered vane profile exhibits non-matching pressure distributions on the upper and lower surfaces, indicating an aerodynamically loaded vane. Time-averaged differential pressure is zero at the leading edge, increasing with chord and reaching a maximum value around mid-chord. At the trailing edge, the time-averaged differential pressure approaches zero. Comparing the computational results of Figure 7-2

with those measured experimentally by Falk [2000] (Figure 7-3), allows three notable observations. Note the experimental results shown in Figure 7-3 are presented in terms of absolute pressure. First, the overall chordwise characteristics of the computational results are similar to those measured experimentally. Second, time-average pressure amplitudes in the computational data are slightly lower than the experimental results; however, the experimental results were collected at 7,000 ft altitude, while the computations were run at standard-day sea-level conditions. Third, while the suction surface displays exactly similar characteristics, along the lower surface slight differences in the trends are seen.

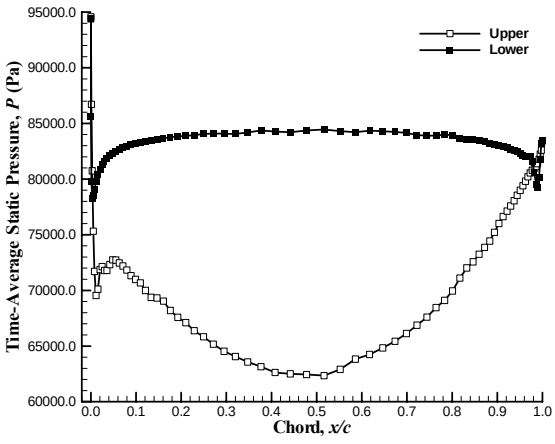

Figure 7-2 Time-Averaged Static Pressure Distribution.

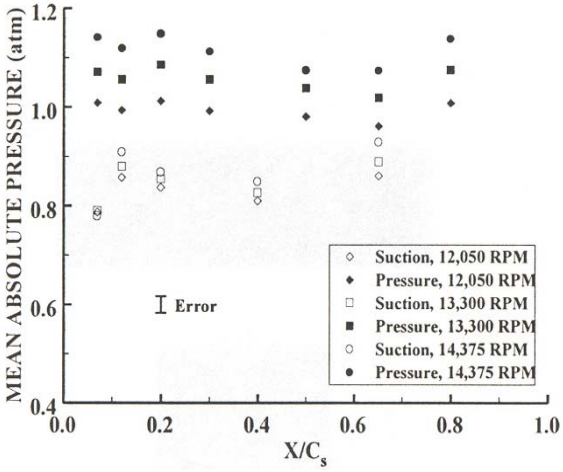

Figure 7-3 Time-Average Pressure Distribution [Falk, 2000].

7.4 UNSTEADY PRESSURE RESULTS

Root-mean-square (RMS) amplitudes for the unsteady pressure data along the stator-vane upper and lower surfaces are shown in Figure 7-4. Comparing the computationally obtained RMS pressures to those of the F109 engine [Falk, 2000], shown in Figure 7-5, several observations can be made; the experimental results in Figure 7-5 are presented in terms of absolute pressures. First, both computational and experimental

results show similar chordwise trends along the suction and pressure surfaces, particularly on the suction surface. Pressure-surface data compare as well, but show deviation in the trailing-edge region. Second, magnitudes for the computationally obtained RMS pressures are again found to be lower than the measured F109 values. This non-agreement of data is attributed to the lower reduced frequency and magnitude of the forcing disturbance employed for the current investigation as compared to the forcing disturbance present in the F109 engine.

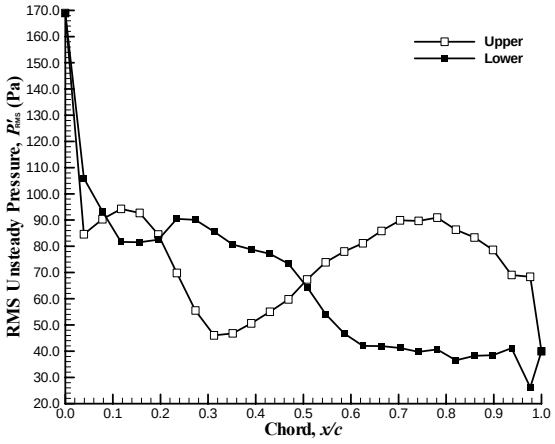

Figure 7-4 RMS Unsteady Pressure Distribution.

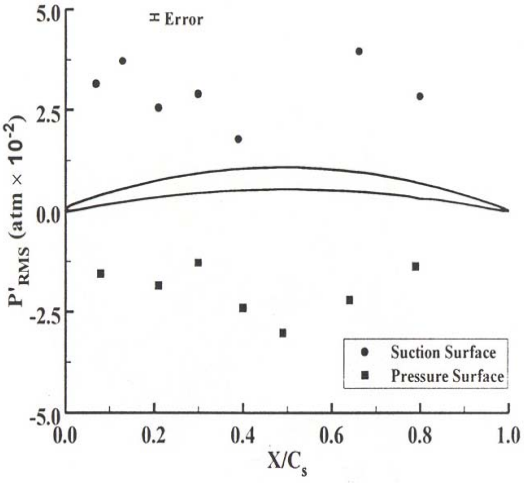

Figure 7-5 P'$_{RMS}$ Distribution [Falk, 2000].

Chordwise first-harmonic amplitudes along the upper and lower surfaces of the stator-vane are exhibited in Figure 7-6. Several observations can be drawn from this figure. First, the data on both upper and lower surfaces display an unsteady leading-edge pressure spike that decays downstream, as in the earlier airfoil configurations. Second, overall amplitude of the lower surface is again higher as compared to the upper surface. Finally, pressure differential between the upper and lower surfaces approaches zero toward the trailing edge. When compared to the unsteady pressure data collected in the F109 engine [Falk, 2000], the computational data compare qualitatively, with slightly

lower amplitudes. Note that the unsteady pressure amplitudes measured experimentally (Figure 7-7) are displayed as normalized values. The slightly lower amplitudes of the computational data are again attributed to the lower reduced frequency and magnitude of the forcing disturbance employed in the current investigation as compared to the forcing disturbance present in the F109 engine.

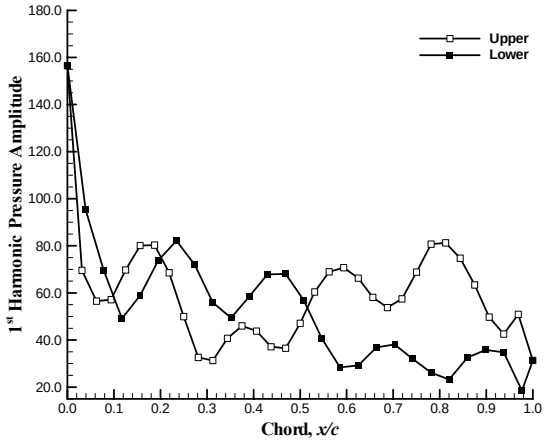

Figure 7-6. 1st Harmonic Amplitude: Stator-Vane.

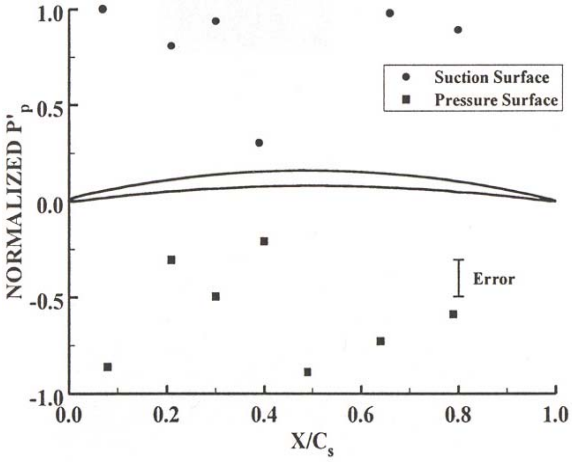

Figure 7-7 Normalized 1st Harmonic Amplitude [Falk, 2000].

Figure 7-8 shows relative phase data for the first-harmonic unsteady surface pressures along the stator-vane. The figure displays airfoil upper and lower-surface phase along the vane chord. The upper-surface and lower-surface phase data exhibit similar chordwise trends. Also, both upper and lower surfaces show a significantly varying phase slope, particularly near the leading and trailing edges. Finally, the lower-surface phase exhibits a rapid change in phase near x/c = 0.3, increasing in slope towards the trailing edge. When compared to the F109 phase data shown in Figure 7-9, the computational data show similar ambiguous disturbance propagation directions to those found in the running F109 engine; following neither the convected or acoustic speeds along the vane. The computational and engine data do not, however, show similar

chordwise trends. This is attributed to the difference in operating conditions employed in the present study as compared to the F109 engine, as specified earlier. In particular the present simulations were performed using standard-day operating conditions while the F109 engine data were obtained at 7,000 ft altitude.

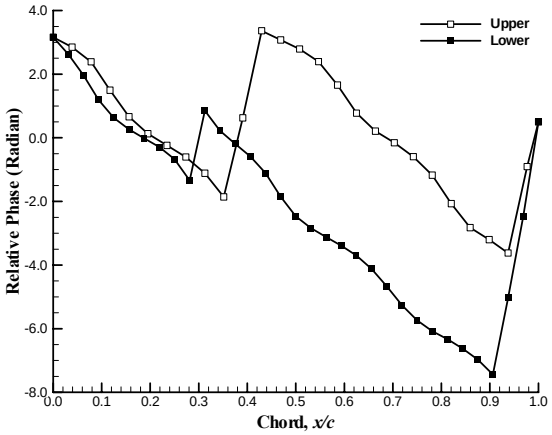

Figure 7-8 1st Harmonic Phase: Stator-Vane.

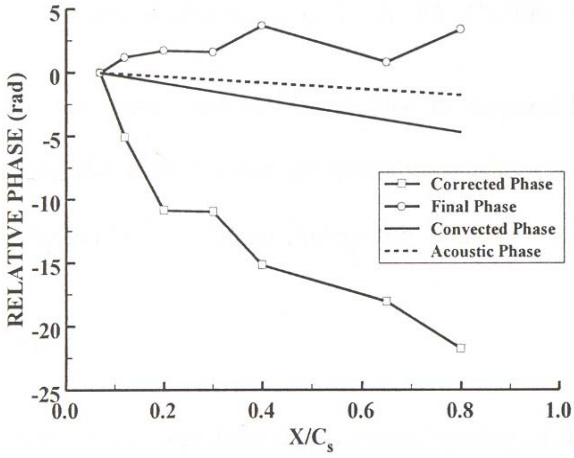

Figure 7-9 Relative Phase Data [Falk, 2000].

Relative phase data for the stator-vane follow similar trends to that seen for the various airfoil cases discussed in Chapter 6. In particular, stator-vane phase data along the upper surface show a mid-chord spike similar to that seen earlier. In addition, relative phase data for the various cambered airfoils exhibit an increasing negative phase slope in the regions forward and aft of mid-chord as camber increased. This is clearly seen in the stator-vane phase data also, with the stator-vane phase data showing a high negative slope due to its large camber profile (12% camber). However, relative phase data along the lower surface of the stator-vane show little similarity with trends observed earlier for the examined cambered profiles. In fact, the lower-surface phase data appear to indicate a constant downstream-propagating disturbance.

7.5 SUMMARY

Unsteady surface-pressure data obtained along the upper and lower surfaces of a simulated cascade vane are presented. These surface-pressure data were reduced into time-averaged and unsteady components, with the unsteady data further decomposed into elements of amplitude, frequency, and phase for first, second and third harmonics. Time-averaged total pressure contours for the simulated vane exhibit attached surface flow with the vane producing a wake similar to that which would be expected. Time-averaged surface-pressure distributions over the vane exhibit non-matching pressure distributions indicating an aerodynamically loaded vane similar to corresponding experimental F109 data.

Unsteady pressures compared favorably, in chordwise distribution, with results from a previous experimental investigation by Falk [2000]. However, magnitudes for the computationally obtained unsteady pressures are found to be slightly lower than experimental values. This is attributed to the lower reduced frequency and magnitude of the forcing disturbance employed in the current research as compared to the forcing disturbance present in the F109 engine.

First harmonic phase data obtained computationally exhibit phase ambiguity similar to that seen earlier in the single - airfoil case, as well as those observed by Falk [2000] in the F109 engine. However, chordwise phase trends do not correlate. Based on the explanation given in Section 5.9 and the results of Fabian et al. and Falk [2000], these ambiguous results additionally support the presumption of the existence of vortical and potential disturbance interactions across the stator-vanes.

8 CHAPTER 8

SUMMARY AND CONCLUSIONS

Unsteady aerodynamic forcing of various lifting surface bodies in cascade is examined through numerical simulation, with specific emphasis given to induced chordwise surface-pressure phase distributions. In particular, the influence of lifting surface thickness, camber and angle of attack is examined. All numerical simulations were conducted using the CFD algorithm FLUENT (v. 6.0). Time-accurate results were analyzed for four symmetric NACA airfoil profiles of 10, 12, 15 and 20% thickness (relative to chord), two cambered airfoils of 2 and 6% camber (relative to chord) and two mean-flow attack angles of 5 and 10 degrees. In addition to the simplified NACA airfoil-cascade configuration, a more complicated cascade configuration was also examined. This configuration employed aerodynamically loaded vanes that mimicked the two-dimensional geometry of the stator-vane row in the fan compression stage of a F109 turbofan engine (at 87.8% span). Aerodynamic forcing of the examined lifting surfaces was achieved by modeling waveform characteristics similar to a passing wake, as might be found in a rotor-stator compression stage.

8.1 RESULTS

8.1.1 Time-Averaged Results

Time-averaged results obtained from FLUENT for the baseline NACA 0012 airfoil show well-behaved characteristics. Total pressure contours around the airfoil

exhibit smooth attached flow with no signs of large-scale separation and a symmetric wake profile. Pitchwise wake profiles developed downstream of the NACA 0012 lifting surface at $x/c = 0.005$ and $x/c = 0.01$ exhibit symmetry as well, further ascertaining this inference. Time-averaged static pressure distributions along the upper and lower surface of the NACA 0012 airfoil are perfectly symmetric, indicating no aerodynamic loading exists on the airfoil, as expected. Comparison of the time-averaged pressures with experimentally obtained values from Abbott and Von Doenhoff exhibit reasonable agreement with very slight discrepancies observed near the leading edge and trailing edge regions. Given this agreement of time-averaged data, the simulations presented correctly predict the time-averaged flowfield about the examined lifting surface.

Time-averaged pressure distributions obtained for various mean flow angles of attack (AOA), various thickness profiles and various camber profiles exhibit characteristics similar to that, which would be expected for the respective profiles. Non-equivalent time-averaged pressure distributions are exhibited at various mean flow angles of attack and by the various camber profiles, indicating aerodynamic loading on these profiles. Differential pressure (aerodynamic loading) is observed to increase as both AOA and percentage of camber relative to chord increased. Conversely, the various thickness profiles exhibit equivalent time-averaged pressure distributions along the upper and lower surfaces indicative of no time-averaged aerodynamic loading. Each thickness profile exhibits distinct time-averaged pressure gradients along the chord, with higher thickness values resulting in more severe chordwise gradients.

Similar to the baseline NACA 0012 case computationally obtained time-averaged results of the parametric analysis were compared with those obtained experimentally by

Abbott and Von Doenhoff [1959]. Here again, as observed for the baseline NACA 0012 case, the computationally obtained time-averaged results compared favorably with the experimental data for all cases.

8.1.2 Unsteady Pressure Data

Unsteady pressure time series data collected along the NACA 0012 airfoil upper and lower surfaces indicate periodic static-pressure variations corresponding to the aerodynamic forcing frequency. The pressure fluctuations, although periodic, are not purely sinusoidal, indicating the existence of harmonic content. Spectral analysis shows surface-pressure harmonic frequencies reaching four times the aerodynamic forcing frequency. Both upper and lower surfaces exhibit increased higher-order pressure harmonics near the airfoil leading edge, generally decaying downstream such that third and fourth harmonic amplitudes almost vanish near the airfoil trailing edge.

First-harmonic phase data exhibit ambiguous disturbance position-vs.-phase maps, from which disturbance propagation direction can not be inferred. Based on the results of Fabian and Jumper, the ambiguous phase results suggest the existence of multiple disturbance interactions across the airfoil, these disturbances having the same primary frequency, but different amplitudes and propagation speeds. A first-order disturbance-interaction model is developed in an attempt to reproduce the ambiguous phase behavior, incorporating a local convectively propagating pressure wave and a global acoustically propagating potential wave. Both disturbances exhibit identical forcing frequencies, but exclusive amplitudes, waveform shapes, and propagation speeds.

The analytically modeled pressure data mimick computationally obtained results quite well. The amplitude of the modeled data was slightly higher at each chordwise

location; however, the corresponding phase data exhibit similar ambiguity in terms of disturbance propagation direction. Thus, presumptive evidence is obtained suggesting phase-map ambiguity in the modeled NACA 0012 data results from interaction between local convectively propagating and global acoustically propagating pressure waves.

First-harmonic pressure amplitude time series data for the various thickness, camber and angle of attack profiles exhibit similar trends in terms of periodic static-pressure variations (corresponding to the aerodynamic-forcing frequency), large unsteady pressure fluctuations near the leading edge (decaying downstream) and a phase shift between chordwise locations. As thickness and AOA were increased, small changes were seen in the time series amplitudes. However, with the increase in camber, time series amplitudes showed significant amplification specifically in the upper surface aft chord region (i.e., x/c = 0.5 - 0.9).

First-harmonic pressure amplitudes of the various thickness, camber and AOA cases also showed similar trends, amplified at the leading edge and decaying along the chord. In general, an increase in first-harmonic pressure amplitudes was seen as thickness, camber and AOA increased, with the first-harmonic amplitudes of the 5 and 10-degree AOA being significantly amplified at the leading edge as compared to the other cases.

First-harmonic phase data along the upper surface of the various thickness, camber and AOA cases exhibited a significantly varying slope, while the lower surfaces exhibited almost no slope. As thickness and camber was increased, a rapid increase in positive phase slope was seen near the airfoil mid-chord. This was attributed to the increased propagation delay experienced by the disturbance at higher thickness and

camber values, similar to that seen in the baseline NACA 0012 case. Unlike the thickness and camber analyses, increasing AOA does not cause an increase in the mid-chord phase change, but rather a shift in the mid-chord phase variations toward the leading edge. This was attributed to the fact that AOA does not alter the airfoil geometry but rather the location of the time-averaged leading edge stagnation point on the airfoil.

Unsteady surface-pressure data obtained along the upper and lower surfaces of a simulated cascade vane are presented. These surface-pressure data were reduced into time-averaged and unsteady components, with the unsteady data further decomposed into elements of amplitude, frequency, and phase for first, second and third harmonics. Time-averaged total pressure contours for the simulated vane exhibit attached surface flow with the vane producing a wake similar to that which would be expected. Time-averaged surface-pressure distributions over the vane exhibit non-matching pressure distributions indicating an aerodynamically loaded vane similar to corresponding experimental F109 data.

Unsteady pressures compared favorably, in chordwise distribution, with results from a previous experimental investigation by Falk [2000]. However, magnitudes for the computationally obtained unsteady pressures are found to be slightly lower than experimental values. This is attributed to the lower reduced frequency and magnitude of the forcing disturbance employed in the current research as compared to the forcing disturbance present in the F109 engine.

First harmonic phase data obtained computationally exhibit phase ambiguity similar to that seen earlier in the single - airfoil case, as well as those observed by Falk [2000] in the F109 engine. However, chordwise phase trends do not correlate. Based on

the explanation given in Section 5.9 and the results of Fabian et al. and Falk [2000], these ambiguous results additionally support the presumption of the existence of vortical and potential disturbance interactions across the stator-vanes.

8.2 CORRELATIONS WITH PREVIOUS INVESTIGATIONS

Results obtained in the current research, correlate well with those reported in previous investigations. For example, experimental investigations by Fleeter et al. [1978, 1980] reported unsteady pressures to be amplified at the leading edge of flat-plate as well as cambered airfoils. Similarly, in the forward forcing cascade investigation of Fabian et al. [1996] unsteady pressure amplification was seen on the stator-vane leading edge. These results correlate well with those presented in the present investigation, where all cases exhibited significant unsteady pressure amplitudes near the leading edge, decaying downstream along the chord.

Surface pressure phase data reported for all cases in the present investigation, exhibited ambiguous characteristics from which no particular disturbance propagation direction could be inferred. This ambiguity was attributed to multiple disturbance interactions occurring on the surface of the lifting bodies, where the multiple disturbances have the same frequency but different propagation speeds. Similar ambiguous phase data were exhibited in the experimental investigations of Fleeter [1978, 1980] and the forward forcing investigation by Fabian [1996]. In fact, all of the above mentioned experimental investigations attributed this ambiguity in phase data to multiple wake interactions on the upper and lower surfaces of the lifting-bodies, where each wake propagated at different speeds.

8.3 CURRENT CONTRIBUTIONS

Several previously conducted investigations have reported surface-pressure phase data on lifting surfaces under a variety of forcing conditions. However, the dependence of lifting-surface response to variations in chordwise surface-pressure phase distribution remains relatively unexamined. Moreover, no known investigation has developed general "rules of thumb" to act as guidelines in predicting phase distributions for the most common forcing configurations. As such, no consistent explanation exists for observed surface-pressure phase variations between different forcing configurations and lifting surfaces.

The current research helps explain the fundamental physics leading to surface-pressure phase ambiguity seen in aerodynamically forward forced lifting surfaces. It is postulated that phase ambiguity is a result of multiple disturbance interactions occurring across the airfoil, these disturbances having the same primary frequency, but different amplitudes and propagation speeds. By means of a first-order disturbance-interaction model it was shown that phase-map ambiguity in the modeled NACA 0012 data results from interaction between local convectively propagating and global acoustically propagating pressure waves.

In addition, the influence of thickness, camber and aerodynamic loading (mean flow angle of attack) on gust phase propagation characteristics were investigated for the first time. Results showed thickness and camber to influence the mid-chord phase slope, with increasing thickness and camber increasing the slope. However, increases in aerodynamic loading produced a shift in the mid-chord phase variations toward the leading edge. The fundamental physics pertaining to these data was also explained.

8.4 RECOMMENDATIONS FOR FUTURE WORK

The current research affords numerous computational and analytical results, where the analytical results approximately reproduced the computationally observed characteristics. While both types of results are significant, this investigation is by no means complete. In fact, a number of further investigations could be undertaken to complete the analysis of the compressor, unsteady aerodynamic environment.

A more detailed three-dimensional computational simulation is recommended where spanwise phase variation is analyzed. Analyzing unsteady surface-pressure distributions at higher Mach number flows is also recommended.

REFERENCES

Abbott, I. H. and Von Doenhoff, A. E., 1959, *Thoery of Wing Sections,* Dover Publications, New York, NY.

Barsom, J. M. and Rolfe, S. T., 1987, *Fracture and Fatigue Control in Structures,* Prentice Hall, Inc., Englewood Cliffs, NJ.

Bernard, P. S. and Wallace, J. M., 2002, *Turbulent Flow; Analysis, Measurement, and Prediction,* John Wiley & Sons, Hoboken, NJ.

Capece, V. R. and Fleeter, S., 1987, "Unsteady Aerodynamic Interactions in a Multistage Compressor," *Journal of Turbomachinery,* Vol. 109, pp. 420-428.

Capece, V. R. and Fleeter, S., 1988, "Wake-Induced Unsteady Aerodynamic Interactions in a Multistage Compressor," *Journal of Propulsion,* Vol. 4, No. 5, pp. 458-465.

Commerford, G. L. and Carta, F. O., 1974, "Unsteady Aerodynamic Response of a Two-Dimensional Airfoil at High Reduced Frequency," *AIAA Journal,* Vol. 12, No. 1, pp. 43-48.

Fabian, M. K. and Jumper, E. J., 1996, "Convected and Potential Unsteady Disturbances Interacting with an Unsteady Cascade," AIAA Paper 96-2672.

Fabian, M. K. and Jumper, E. J., 1999, "Rearward Forcing of an Unsteady Compressible Cascade," AIAA *Journal of Propulsion and Power*, Vol. 15, No. 1, pp. 23-30.

Fabian, M. K., 1995, "Unsteady Pressure Distributions Around compressor Vanes in an Unsteady Transonic Cascade," PhD Dissertation, University of Notre Dame.

Fabian, M. K., Falk, E. A., and Jumper, E. J., 2001, "Upstream-Propagating Potential

Disturbances Interacting with a Compressible Cascade," AIAA *Journal of Propulsion and Power*, Vol. 17, No. 2, pp. 262-269.

Falk, E.A., Jumper, E.J., and Fabian, M.K., 1997, "An Experimental Study of Unsteady Forcing in the F-109 Turbofan Engine," AIAA paper number 97-3286.

Falk, E.A., Jumper, E.J., Fabian, M.K., and Haven, B.A., 1999, "A Characterization of the Unsteady Velocity Field Aft of the F-109 Turbofan Rotor," AIAA paper number 99-0237.

Falk, E. A., 2000, "An Experimental Investigation of Aerodynamic Forcing in the F109 Turbofan Engine Compressor," PhD Dissertation, University of Notre Dame.

Falk, E. A., Bakhtiani, H. P., and Darbe, R. P., 2003, "Influence of Time-Resolved Surface Pressure Phase Distributions on Airfoil Unsteady Response," AIAA Paper 03-4982.

Fecke, T., 1998, "HCF program technical accomplishments overview," Third National Turbine Engine High Cycle Fatigue (HCF) Conference.

Fleeter, S., Bennett, W. A., and Jay, R. L., 1980, "The Time-Variant Aerodynamic Response of a Stator Row Including the Effects of Airfoil Camber," *Journal of Engineering for Power,* Vol. 102, pp. 334-343.

Fleeter, S., Capece, V. R., and Chiang H. D., 1988, "Unsteady Aerodynamic Gust Response Including Steady Flow Separation," *AIAA Journal*, Vol.28, No.6, pp. 1024-1031.

Fleeter, S., Jay, R. L., and Bennett, W. A., 1978, "Rotor Wake Generated Unsteady Aerodynamic Response of Compressor Stator," *Journal of Engineering for Power,* Vol. 100, pp. 664-675.

FLUENT User Services Center, FLUENT Users Manual, February 2004, http://www.fluentusers.com/fluent61/doc/doc_f.htm

FLUENT User Services Center, UDF Manual, November 2001, http://www.fluentusers.com/fluent61/doc/ori/html/udf/node1.htm

Franke, G. F. and Henderson, R. E., 1980, "Unsteady Stator Response to Upstream Rotor Wakes," *Journal of Aircraft,* Vol. 17, No.7, pp. 500-507.

Frey, K.K. and Fleeter, S., 1998, "Rotating Compressor Blade Row Gust Unsteady Aerodynamics," AIAA paper number 98-3435.

Hall, K.C. and Verdon,J.M., 1991, " Gust Response Analysis for Cascades Operating in Nonuniform Mean Flows," AIAA Journal, Vol.25, No.9, pp.1463-1471.

Johnston, R. T. and Fleeter, S., 1996, "Three-dimensional Wake Forcing Functions Generated by a High Speed Rotor," AIAA Paper 96-2566.

Johnston, R. T., and Fleeter, S., 2001, "Inlet Guide Vane Wakes Including Rotor Effects," *Journal of Fluids and Structures,* Vol. 15, pp. 235-253.

Lakshminarayana, B. and Davino, R., 1980, "Mean Velocity and Decay Characteristics of the Guidevane and Stator Blade Wake of an Axial Flow Compressor," *Journal of Engineering for Power,* Vol. 102, pp. 50-60.

Launder, B.E. and Spalding, D. B., 1972, *Lectures in Mathematical Models of Turbulence,* Academic Press, London, England.

Prato, J. and Lakshminarayana, B., 1993, "Investigation of Compressor Rotor Wake Structure at Peak Pressure Rise Coefficient and Effects of Loading," *Journal of Turbomachinery,* Vol. 115, pp. 487-500.

Ravindranath, A. and Lakshminarayana, B., 1980, "Mean Velocity and Decay

Characteristics of the Near and Far-Wake of a Compressor Rotor Blade at Moderate Loading," *Journal of Engineering for Power,* Vol. 102, pp. 535-547.

Reynolds, B., Lakshminarayana, B., and Ravindranath, A., 1979, "Characteristics of the Near Wake of a Compressor of a Fan Rotor Blade," *AIAA Journal,* Vol. 17, No. 9, pp. 959-967.

Sears, W. R., 1941, "Some Aspects of Non-Stationary Airfoil Theory and Its Practical Application," *Journal of the Aeronautical Society,* Vol. 18, pp. 104-108.

Thompson, D., 1998, "The National High Cycle Fatigue (HCF) Program," Third National Turbine Engine High Cycle Fatigue Conference.

Valkov, T. V. and Tan, C. S., 1999, "Effect of Upstream rotor Vortical Disturbances on the Time-Averaged Performance of Axial Compressor Stators: Part 1 – Framework of Technical Approach and Wake – Stator Blade Interactions," *Journal of Turbomachinery,* Vol. 121, pp. 377-386.

Von Karman, T. and Sears, W. R., 1938, "Airfoil Theory for Non-Uniform Motion," *Journal of the Aeronautical Sciences,* Vol. 5, No. 10, pp. 379-390.

White, F.M., 1991, *Viscous Fluid Flow,* McGraw-Hill Inc., New York, NY.

A. APPENDIX A

CASCADE NOMENCLATURE

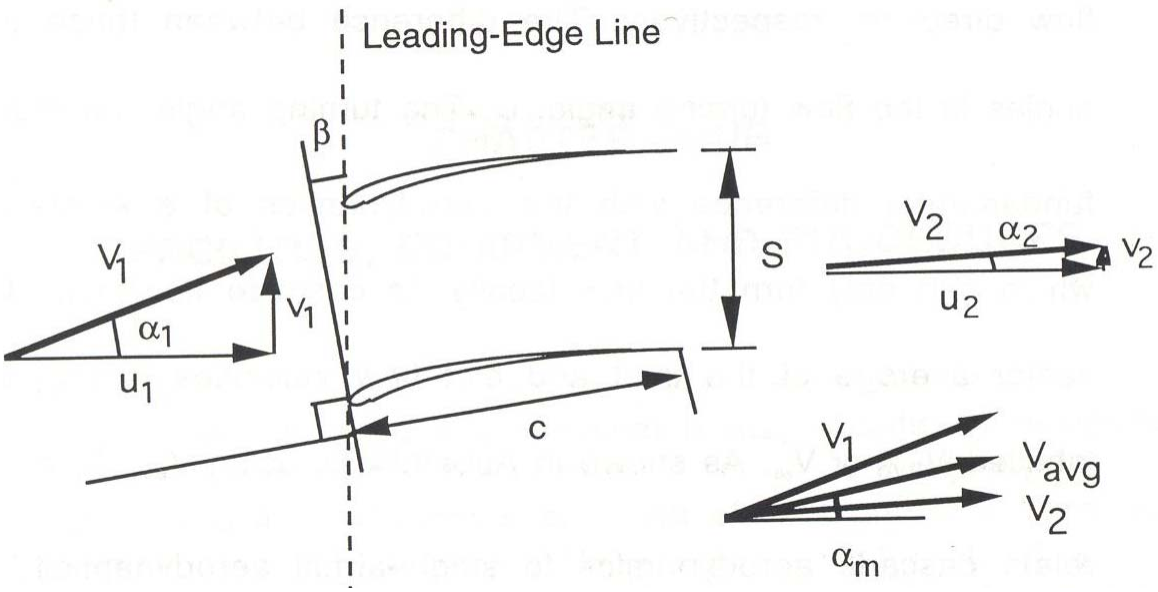

Figure A-1 Cascade Geometry [Fabian, 1995].

In turbomachinery applications, a linear cascade represents an unwrapping of a rotor or stator row into a row of airfoils. The close proximity of airfoils in a cascade row requires the definition of additional terms beyond the single airfoil terminology. The airfoil chord has the usual definition of the distance from the leading edge to the trailing edge of an airfoil. As shown in Figure A-1, spacing, S, is the distance from the leading edge to leading edge (and also trailing edge to trailing edge) of consecutive airfoils on the row. Solidity, σ. Is the ratio of chord to spacing. The leading-edge line is the line tangent to the leading edges of the cascade row. Stagger angle, β, is the angle between the leading-edge line and the perpendicular to the chord line. At high stagger angles or low

solidity, the interaction of the blade pressure fields is reduced. The cascade flow angles, α_1 and α_2, are the angles between the axial direction (perpendicular to the leading edge line) and the cascade-entrance-flow direction and exit-flow direction, respectively. The difference between these two angles is the flow turning angle, φ. The turning angle represents a fundamental difference with the aerodynamics of a single-airfoil, which can only turn the flow locally. In cascade flowfields, the vector average of the inlet and exit flow velocities is frequently labeled V_{avg}. Using V_{avg} helps to relate cascade aerodynamics to single-airfoil aerodynamics. The angle between V_{avg} and the perpendicular to the leading-edge line is termed the mean flow angle, α_m. The angle between the chordline and V_{avg} is the cascade angle of attack, α. A final angle to be mentioned is the deviation angle, δ, which is the difference between an extension of the trailing-edge camber line and the exit flow vector. It represents the ability of the cascade to turn the flow through the desired angle, approximately parallel to the trailing-edge line.

B. APPENDIX B

STATOR-VANE COORDINATES

Table B.1 Stator-Vane Coordinates In Terms of Half-Chord.

x/(c/2)	y pressure/(c/2)	y suction/(c/2)
-1.00E+00	0.00E+00	0.00E+00
-9.98E-01	-3.50E-03	1.25E-02
-9.95E-01	-4.50E-03	1.80E-02
-9.93E-01	-5.00E-03	2.30E-02
-9.90E-01	-5.00E-03	2.65E-02
-9.85E-01	-4.00E-03	3.25E-02
-9.80E-01	-2.50E-03	3.80E-02
-9.75E-01	-1.00E-03	4.19E-02
-9.70E-01	6.55E-04	4.50E-02
-9.40E-01	1.03E-02	6.45E-02
-9.10E-01	1.96E-02	8.09E-02
-8.80E-01	2.87E-02	9.67E-02
-8.50E-01	3.74E-02	1.12E-01
-8.20E-01	4.58E-02	1.27E-01
-7.90E-01	5.40E-02	1.41E-01
-7.60E-01	6.18E-02	1.55E-01
-7.30E-01	6.93E-02	1.68E-01
-7.00E-01	7.65E-02	1.80E-01
-6.50E-01	8.79E-02	2.00E-01
-6.00E-01	9.84E-02	2.18E-01
-5.50E-01	1.08E-01	2.35E-01
-5.00E-01	1.17E-01	2.50E-01
-4.50E-01	1.25E-01	2.64E-01
-4.00E-01	1.32E-01	2.76E-01
-3.50E-01	1.38E-01	2.87E-01
-3.00E-01	1.44E-01	2.96E-01
-2.50E-01	1.49E-01	3.04E-01
-1.50E-01	1.55E-01	3.15E-01
-5.00E-02	1.59E-01	3.20E-01
5.00E-02	1.59E-01	3.19E-01
1.50E-01	1.55E-01	3.11E-01
2.50E-01	1.49E-01	2.98E-01
3.00E-01	1.44E-01	2.89E-01
3.50E-01	1.39E-01	2.79E-01
4.00E-01	1.32E-01	2.67E-01

4.50E-01	1.25E-01	2.54E-01
5.00E-01	1.17E-01	2.39E-01
5.50E-01	1.09E-01	2.23E-01
6.00E-01	9.90E-02	2.05E-01
6.50E-01	8.85E-02	1.85E-01
6.80E-01	8.18E-02	1.73E-01
7.10E-01	7.48E-02	1.60E-01
7.40E-01	6.75E-02	1.47E-01
7.70E-01	5.99E-02	1.33E-01
8.00E-01	5.20E-02	1.18E-01
8.30E-01	4.38E-02	1.03E-01
8.60E-01	3.53E-02	8.77E-02
8.90E-01	2.65E-02	7.16E-02
9.20E-01	1.74E-02	5.49E-02
9.50E-01	7.99E-03	3.77E-02
9.80E-01	-1.72E-03	2.00E-02
9.90E-01	-8.61E-04	9.98E-03
1.00E+00	0.00E+00	0.00E+00

C. APPENDIX C

USER DEFINED FUNCTION (UDF) DESCRIPTION

A user-defined function, or UDF, is a function that you program that can be dynamically loaded with the FLUENT solver to enhance the standard features of the code. UDFs are written in the C programming language. They are defined using DEFINE macros that are supplied by Fluent Inc. They access data from the FLUENT solver using predefined macros and functions also supplied by Fluent Inc. Every UDF contains the *udf.h* file inclusion directive (*#include "udf.h")* at the beginning of the source code file, which allows definitions for DEFINE macros and other Fluent-provided macros and functions to be included during the compilation process. UDFs are executed as either interpreted or compiled functions in FLUENT. Values that are passed to the solver by a UDF or returned by the solver to a UDF must be specified in SI units.

In summary, UDFs:

- are written in the C programming language.
- must have an include statement for the *udf.h* file.
- must be defined using DEFINE macros supplied by Fluent Inc.
- access FLUENT solver data using predefined macros and functions supplied by Fluent Inc.
- are executed as interpreted or compiled functions.
- must have all values returned to the FLUENT solver specified in SI units.

User-defined functions can perform a variety of tasks in FLUENT. They can return a value unless they are defined as void in the *udf.h* file. If they do not return a value, they can modify an argument, modify a variable not passed as an argument, or perform I/O tasks with case and data files. In summary, UDFs can:

- return a value.
- modify an argument.
- return a value *and* modify an argument.
- modify a FLUENT variable (not passed as an argument).
- write information to (or read information from) a case or data file.

UDFs are written in C using any text editor and the source file is saved with a .c file extension. Source files typically contain a single UDF, but they can contain multiple, concatenated functions. Source files can be either interpreted or compiled in FLUENT. For interpreted UDFs, source files are interpreted and loaded directly at *runtime*, in a single-step process. For compiled UDFs, the process involves two separate steps. A shared object code library is first built and then it is loaded into FLUENT. Once interpreted or compiled, UDFs will become visible and selectable in FLUENT graphics panels, and can be hooked to a solver by choosing the function name in the appropriate panel.

C.1 UDF EMPLOYED FOR THE CURRENT RESEARCH

The C-source code of the UDF employed in the present research is presented below. The functionality of the UDF is designated by the leading DEFINE macro. Here, the DEFINE_PROFILE macro is used to indicate to the solver that the following code will provide profile information at boundaries.

```
/************************************************************/
/*UDF for specifying a wake total-pressure profile boundary condition        */
/************************************************************/
#include "udf.h"
DEFINE_PROFILE(inlet_t_pressure, thread, position)
{
        real x[ND_ND];      /*this will hold the position vector*/
        real y,t;
        int cycles,buffer,n;   /*this holds the number of cycles needed and buffer*/
        real mag[ND_ND][ND_ND];
        real sum;
        int k,j;
        face_t f;
        cycles = 800;   /*specifies the number of cycles*/
        buffer = 80;
        j = 0;    /*intialization*/
        begin_f_loop(f,thread)  /*begin face loop*/
                {
                        F_CENTROID(x,f,thread);  /*get face centroid value*/
                        y = x[1];                        /*set y equal to the centroid value*/
                        t = RP_Get_Real("flow-time"); /*get real flow time*/
                        sum = 0;
                        for (n = (-cycles-buffer); n <= buffer ; n++)
                                {
                                sum = sum + 55*exp(-60.0*((y-8*t+n*4.)*(y-8*t+n*4.)));
                                }
                        F_PROFILE(f,thread,position) = -sum + 101325 ;
                }
        end_f_loop(f,thread)
}
```

The first argument of the DEFINE_PROFILE macro, **inlet_t_pressure**, is used to identify the function in the Pressure Inlet panel. The name is arbitrary and is specified by you. The equation in the function will be applied to all cell faces (identified by f in the face loop) on a given boundary zone (identified by thread). The thread is defined automatically when you select the UDF for a particular boundary in the FLUENT graphical user-interface. The index is defined automatically through the **begin_f_loop** utility. In this UDF, the **begin_f_loop** macro is used to loop through all cell faces in the boundary zone. For each face, the coordinates of the face centroid are accessed by the

F_CENTROID macro. The coordinate *y* is used in the wake profile equation and the returned total pressure value is assigned to the face through the **F_PROFILE** macro. **begin_f_loop** and **F_PROFILE** are Fluent-supplied macros. For further information regarding the FLUENT-supplied macros, the reader is referred to the FLUENT UDF manual.

D. APPENDIX D

NACA 0012 BASELINE CONFIGURATION RESULTS

This appendix provides additional results obtained for the NACA 0012 lifting surface not given in Chapter 5. In particular, chordwise differential-pressure data and higher harmonic amplitude and phase data are presented.

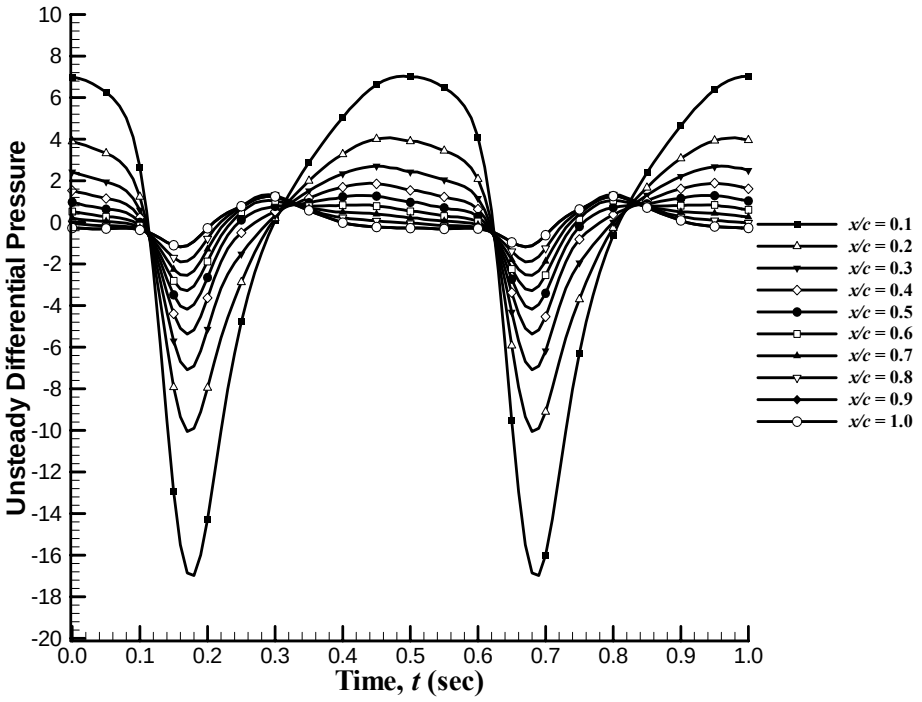

Figure D-2 Unsteady Differential Static Pressure Time-Series.

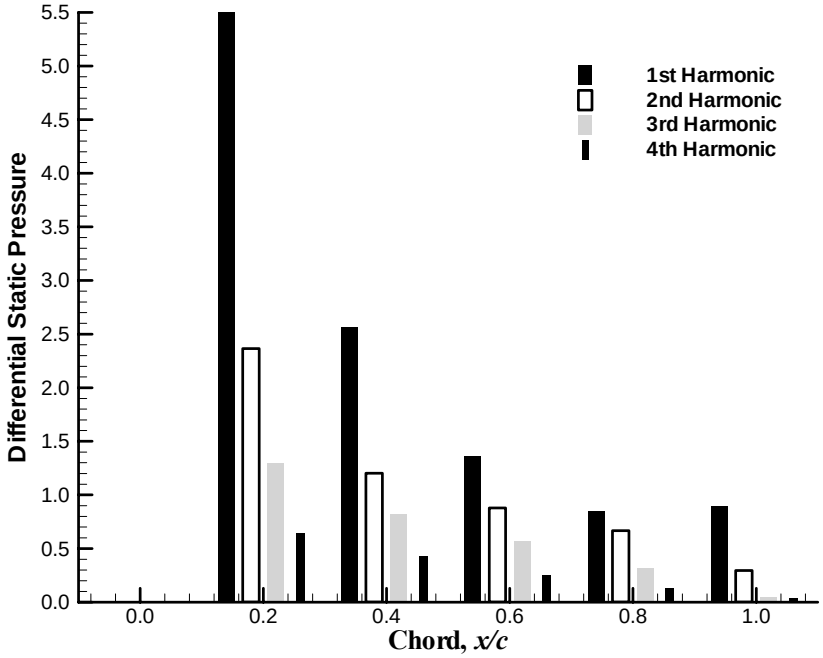

Figure D-3 Unsteady Differential-Pressure Spectral Content.

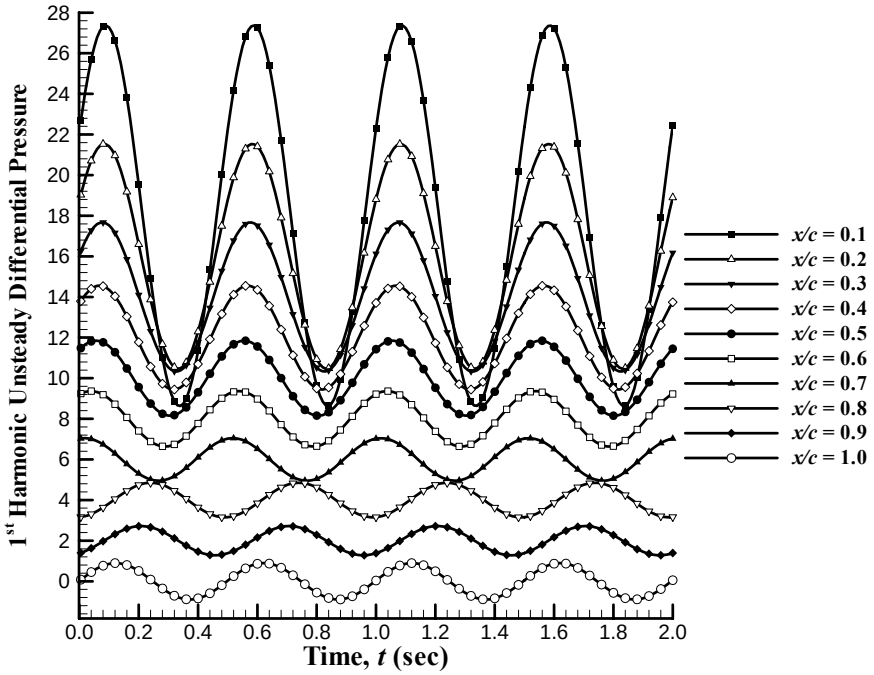

Figure D-4 1st Harmonic Differential-Pressure Time-Series.

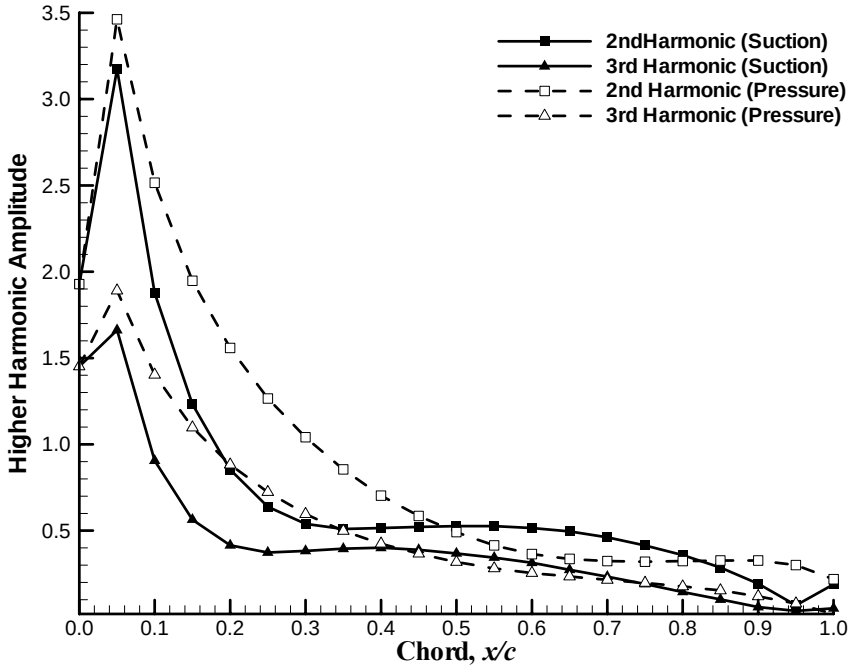

Figure D-5 Higher Harmonic Amplitudes: NACA 0012.

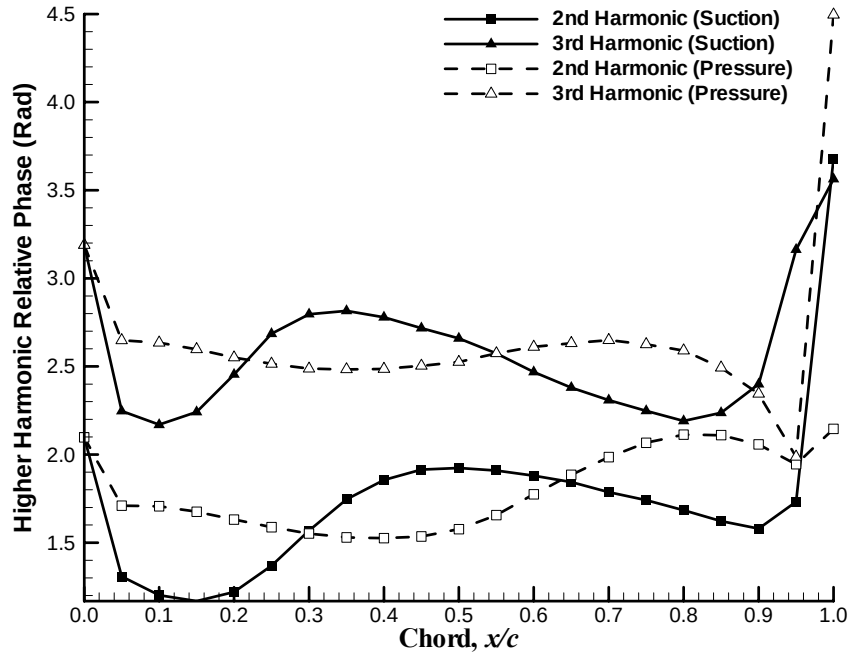

Figure D-6 Higher Harmonic Phase: NACA 0012.

E. APPENDIX E

INFLUENCE OF THICKNESS RESULTS

This appendix presents additional thickness analysis results not presented in Chapter 6. In particular time-series data as well as upper-surface spectral content of the various thickness cases are presented.

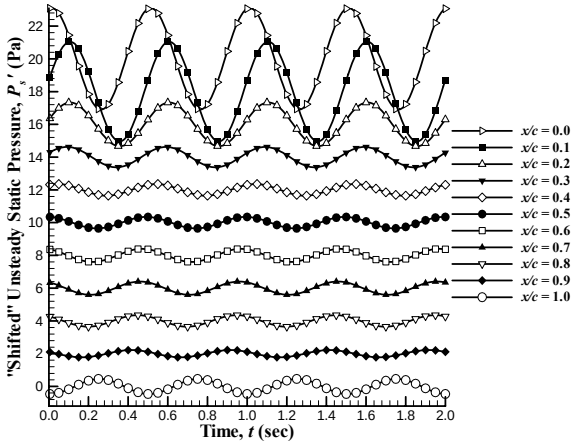

Figure E-7 1st Harmonic Time-Series: NACA 0010 Upper Surface.

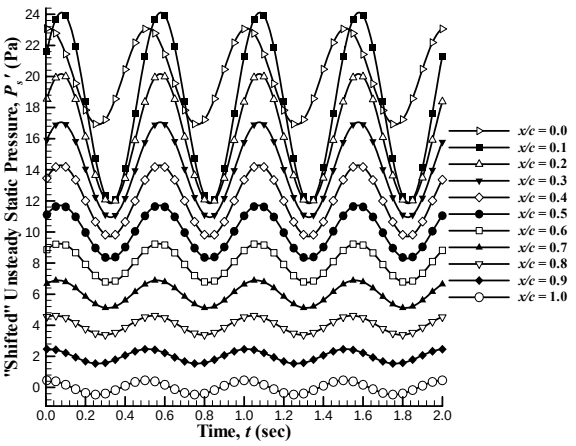

Figure E-8 1st Harmonic Time-Series: NACA 0010 Lower Surface.

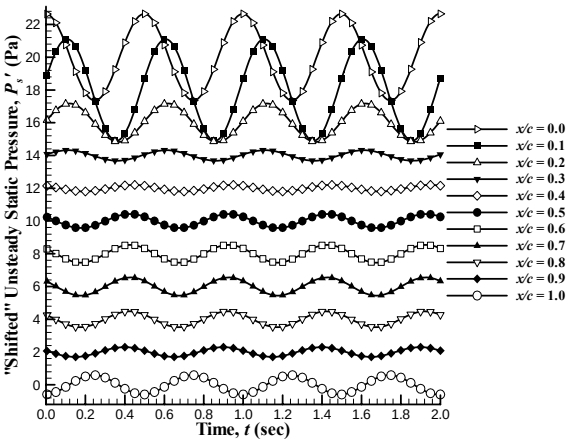

Figure E-9 1st Harmonic Time-Series: NACA 0015 Upper Surface.

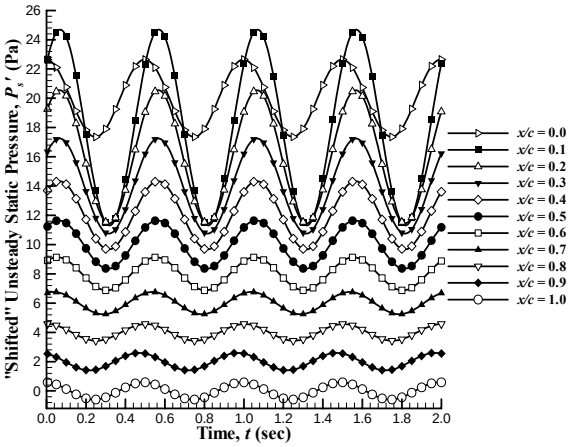

Figure E-10 1st Harmonic Time-Series: NACA 0015 Lower Surface.

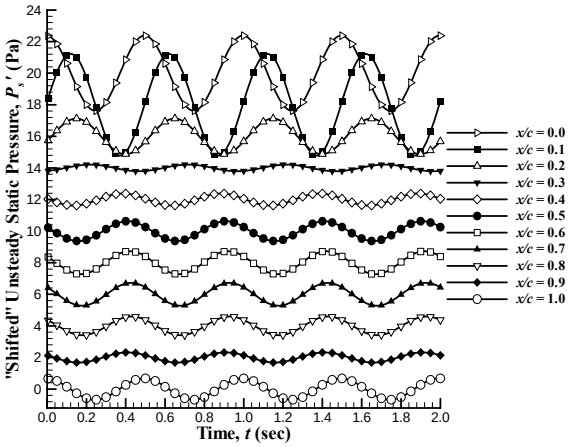

Figure E-11 1st Harmonic Time-Series: NACA 0020 Upper Surface.

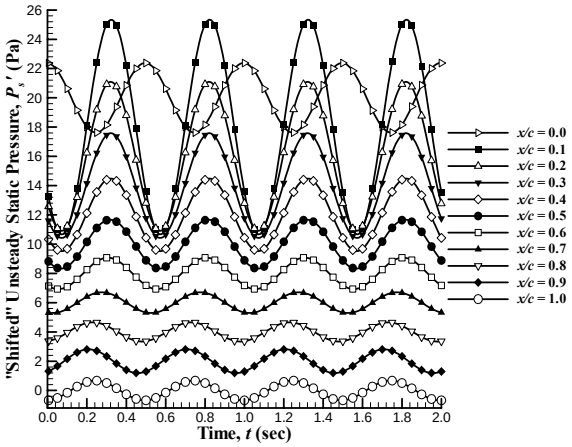

Figure E-12 1st Harmonic Time-Series: NACA 0020 Lower Surface.

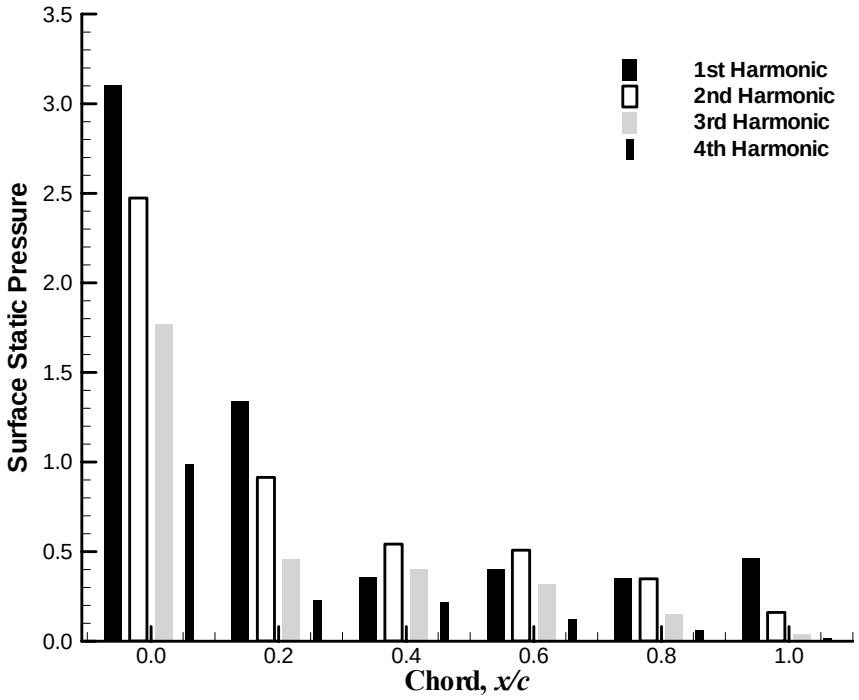

Figure E-13 Surface-Pressure Spectral Content: NACA 0010 Upper Surface.

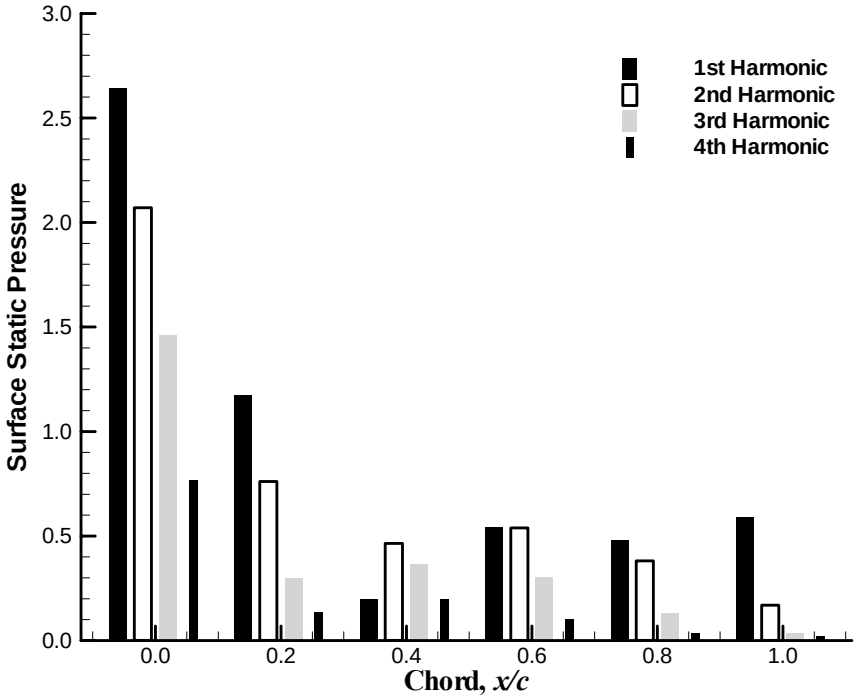

Figure E-14 Surface-Pressure Spectral Content: NACA 0015 Upper Surface.

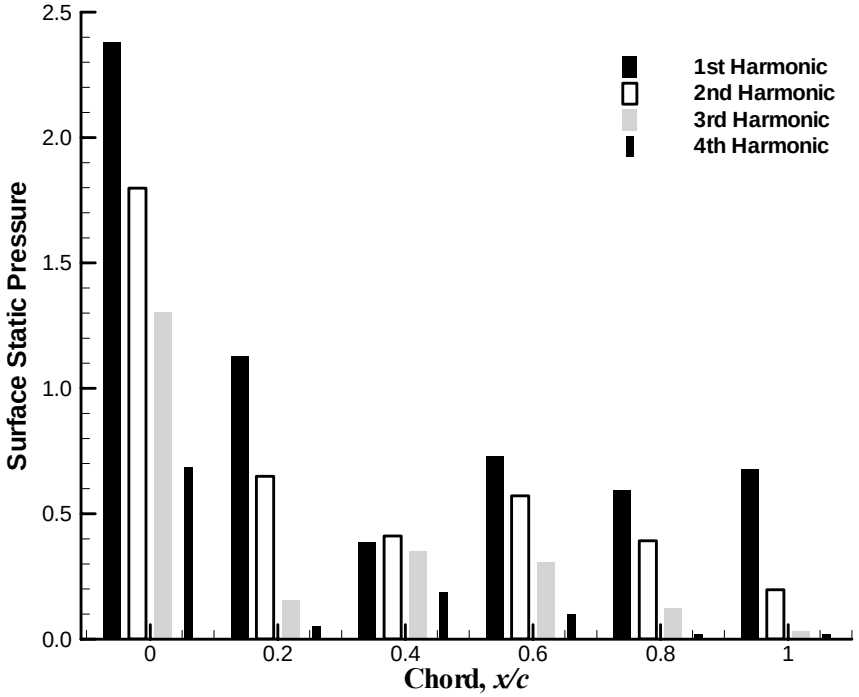

Figure E-15 Surface-Pressure Spectral Content: NACA 0020 Upper Surface.

F. APPENDIX F

INFLUENCE OF CAMBER RESULTS

This appendix presents first-harmonic time-series data along the upper and lower surfaces of the 2% and 6% cambered airfoils.

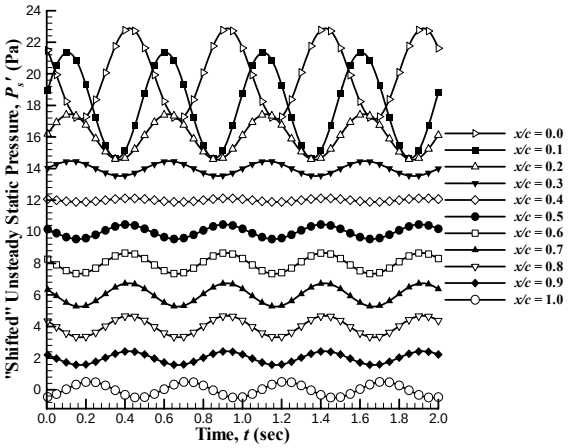

Figure F-16 1st Harmonic Time-Series: 2% Camber Airfoil Upper Surface.

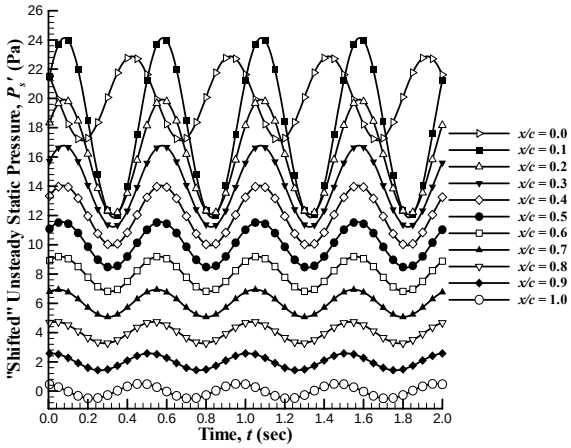

Figure F-17 1st Harmonic Time-Series: 2% Camber Airfoil Lower Surface.

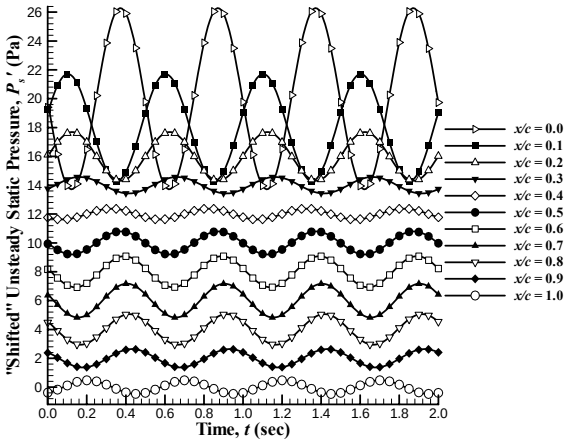

Figure F-18 1st Harmonic Time-Series: 6% Camber Airfoil Upper Surface.

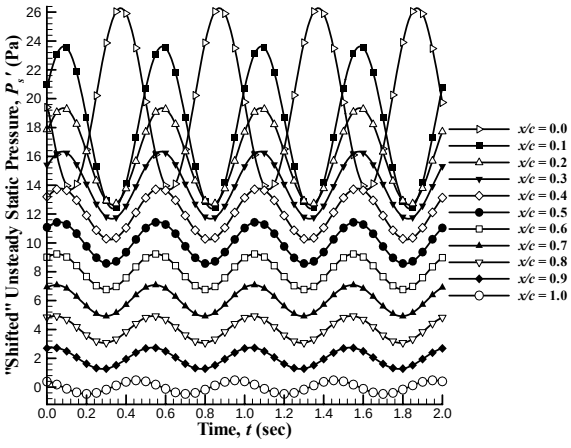

Figure F-19 1st Harmonic Time-Series: 6% Camber Airfoil Lower Surface.

G. APPENDIX G

INFLUENCE OF MEAN-FLOW ANGLE-OF-ATTACK RESULTS

This appendix presents upper-surface and lower-surface first-harmonic time-series data 5 and 10-degrees mean-flow AOA.

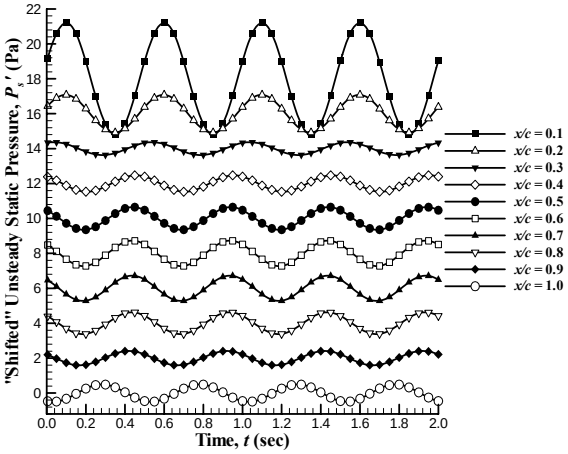

Figure G-20 1st Harmonic Time-Series: 5-Degree AOA Upper Surface.

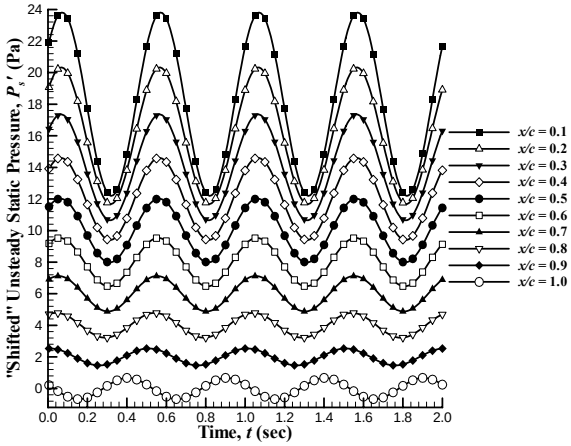

Figure G-21 1st Harmonic Time-Series: 5-Degree AOA Lower Surface.

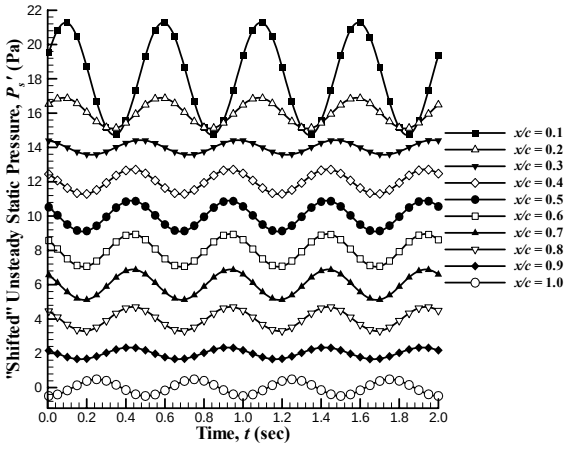

Figure G-22 1st Harmonic Time-Series: 10-Degree AOA Upper Surface.

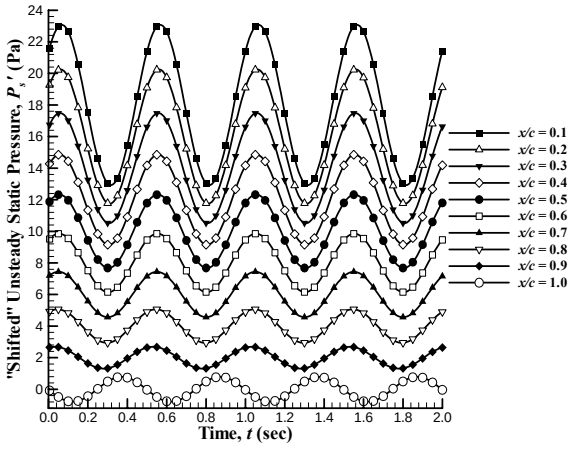

Figure G-23 1st Harmonic Time-Series: 10-Degree AOA Lower Surface.

VITA

HARIKISHIN PRAKASH BAKHTIANI

Candidate for the Degree of

Master of Science

Thesis: A PARAMETRIC ANALYSIS OF GUST-INDUCED AIRFOIL SURFACE-PRESSURE PHASE BEHAVIOR

Major Field: Mechanical Engineering

Biographical:

Personal Data: Born in Pune, India on September 17, 1979, the son of Prakash Govindram Bakhtiani and Jaya Prakash. Bakhtiani.

Education: Graduated from the Our Own English High School in Dubai, U.A.E. in March 1997; Received Bachelor of Science in Aerospace Engineering from Oklahoma State University, Stillwater, Oklahoma in May 2002;Completed requirements for the Master of Science degree with a major in Mechanical Engineering at Oklahoma State University in July 2004.

Experience: Employed by Oklahoma State University as a Graduate Research Assistant and Teaching Assistant in the Department of Mechanical and Aerospace Engineering from 2002 to 2004.

Professional Membership: American Institute of Aeronautics and Astronautics, Pi Tau Sigma.